# Collective Effects of Laser-Driven Cold Atoms in an Optical Cavity

PhD thesis

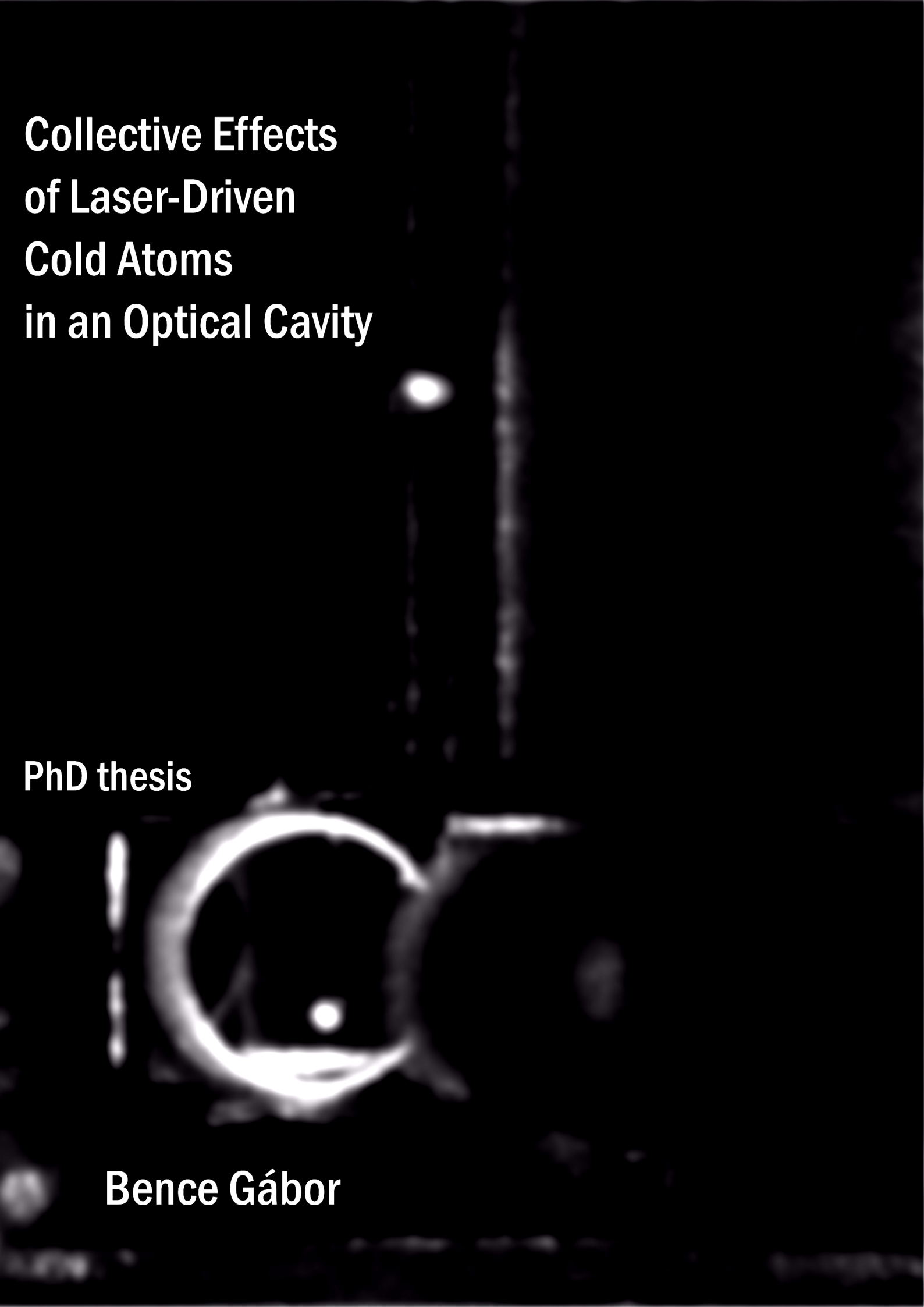

Bence Gábor

# *Collective Effects of Laser-Driven Cold Atoms in an Optical Cavity*

PhD Thesis


Bence GÁBOR

Supervisor: Peter Domokos, PhD, research professor

Doctoral School of Physics

Department of Theoretical Physics

Faculty of Science and Informatics

University of Szeged

Quantum Optics “Momentum” Group

Department of Quantum Optics and Quantum Information

Institute for Solid State Physics and Optics

HUN–REN Wigner Research Centre for Physics


Szeged, 2025

*Dominus illuminatio mea et salus mea,*
*quem timebo?*
Psalmus XXVI

# Contents

# Abbreviations

**AOM** acousto-optic modulator 21, 37, 38, 49, 63, 66

**APD** avalanche photodiode 31, 32

**BCS** bipolar current source 30

**CQED** cavity quantum electrodynamics 4–6, 19, 27, 48, 51, 55, 94

**cw** continuous wave 4, 17

**DFB** distributed-feedback 24

**DQPT** dissipative quantum phase transition 7, 46, 47, 69–71, 75

**ECDL** external-cavity diode laser 18, 24, 28

**EIT** electromagnetically induced transparency 50

**EOM** electro-optic modulator 18, 21, 23, 28

**FALC** Fast Analog Linewidth Control 21, 26

**FM** frequency modulation 21–23, 25

**FORT** far off-resonance trap 29

**FPGA** field-programmable gate array 26

**FSR** free spectral range 71

**GUI** graphical user interface 26

**HWHM** half-width at half-maximum 17, 21, 25–27, 50

**IR** infrared 4

**MOT** magneto-optical trap 5, 18, 24, 30, 33–37, 39, 81, 83, 87

**PBB** photon-blockade-breakdown 48, 54, 70

**PBS** polarizing beamsplitter 25, 82, 83

**PDH** Pound–Drever–Hall 25, 26, 28

**PID** proportional–integral–derivative 23, 27

**PLL** phase-locked loop 24, 81

**QED** quantum electrodynamics 4, 5, 45, 68, 70, 80

**RF** radio frequency 21, 23, 28

**RWA** rotating wave approximation 13

**SNSPD** superconducting nanowire single photon detector 31, 32, 81, 84, 125

**SPC** single photon counter 31, 32, 81, 88

**TA** tapered amplifier 24, 25, 34

**TBB** transmission-blockade-breakdown 47–49

**UHV** ultra-high vacuum 30

**UV** ultraviolet 4

# Introduction

If physicists were asked to name the birthdate of quantum theory, many would probably say 14 December 1900. This was the day when Planck published his explanation of the spectrum of thermal blackbody radiation [1], in which he heuristically assumed the quantum nature of light. This groundbreaking idea inspired a series of conceptual developments [2–6], each contributing to the establishment of quantum mechanics as a distinct branch of physics. A comprehensive quantum theory was proposed by Heisenberg [7] and Schrödinger [8], unified and formalized later by Dirac [9] and von Neumann [10]. This early history of quantum mechanics, briefly outlined above, usually referred to as the *first quantum revolution* [11–13] had set the stage for an optics and solid-state physics based on quantum mechanics, which revealed the deeper nature of light and matter. It could be then exploited in various applications, such as transistors, LEDs, lasers etc.

By today, in the era of the *second quantum revolution*, manipulating, and what is more, designing and constructing individual quantum systems, such as atoms and photons have become possible. Since the foundation of quantum mechanics, advances in spectroscopy and high-level manipulation of atoms had been achieved, taking full advantage of the invention of lasers as well-controlled sources of light. Optical pumping [14–16], magnetic trapping [17], laser cooling and trapping [18–21] of atoms are techniques that have been developed since the second half of the 20th century, and are now routinely employed in experiments studying their interaction with electromagnetic radiation. The primary objective extends beyond a deeper understanding of light-matter interactions to the development of new technologies

based on the quantum nature of these systems. Key research directions include quantum sensing [22], quantum metrology [23], quantum cryptography [24], quantum communication [25] and quantum computing [26].

Various platforms are suitable for such investigations: beyond different neutral atoms (mostly but not exclusively alkaline and alkaline earth metals) [27], ions [28], nanoparticles [29] and artificial atoms [30] can be exposed to electromagnetic radiation, which may take the form of microwave, infrared (IR), visible light or ultraviolet (UV). For the latter three, continuous wave (cw) lasers play a key role, as narrow-linewidth, coherent sources of radiation. Since their invention, laser technology has seen remarkable advancements in both linewidth and stability [31], which had an influence on the improvement of our ability of manipulating atomic matter. Lasers with linewidth well below that of the addressed atomic transitions are available today, allowing for precise spectroscopic measurements and well-controlled experiments.

The effect of electromagnetic radiation can be further enhanced and modified by means of optical resonators. The research field of cavity quantum electrodynamics (CQED), arising from the application of optical cavities, reveals a genuinely distinct regime of light-matter interactions. In many cases of interest, matter is considered as means of manipulating light: it can modify the properties of propagation (e.g. via scattering or dispersion), the frequency (through Raman scattering, harmonic generation etc.), the polarization (through birefringence or dichroism) or the intensity (by amplification or absorption). By contrast, as mentioned above, light can also be used as a tool to manipulate matter. Cavity QED combines the two domains of phenomena in a coupled dynamics of light and matter, in which they can mutually influence each other. This interaction becomes particularly interesting when the characteristic frequency of the coupling strength exceeds the dissipative rates. Aiming for this so-called *strong coupling regime*, CQED, as a research field, is devoted to explore the ultimate limits of non-linear atom-light interaction at the single atom, single photon level.

Strong atom-cavity coupling can be achieved by either cavity design, as the cou-

pling constant is determined by the geometry, or by making use of the collective behaviour of multiple identical atoms interacting with the same cavity mode. When an ensemble of atoms interacts with a mode of a resonator, each atom couples to the mode, and its electronic state and spatial position influences the mode. This field, in turn, acts back on the state and position of all the atoms. As a consequence, the atoms communicate with each other via the cavity field, regardless of their spatial separation. This approach also allows for tuning the collective coupling by adjusting the number of atoms in the mode volume.

Cavity QED schemes typically involve few degrees of freedom that are relevant to the atom-light interaction. The field is composed of a single or only a few modes, and the interacting atoms can be represented by a small set of electronic states. In these systems, cold atoms can be held in a magneto-optical trap (MOT), or loaded into a cavity-sustained optical dipole trap, or be tightly confined in atom-chip based magnetic traps [32]. Such physical realizations of CQED systems have a multitude of applications in quantum information processing and quantum sensing: the cavity can enable sensitive measurement of the atomic dynamics or state at spectroscopic sensitivity below the standard quantum limit for coherent spin states [33, 34], real-time monitoring of the spatial distribution [35] or the atom number in evaporative cooling of atoms [36]. Superradiance decoherence caused by long-range Rydberg atom pair interactions, too, has been demonstrated by using cavity-assisted measurements [37]. Another prospect of strongly coupled atom-cavity systems is given by optical lattice clocks, which are based on lasing on a narrow atomic transition within a resonator [38–41]. The cavity mode can have a dynamical role such that the hybrid atom-photon excitations introduce new features to non-linear optics. For example, in the case of multiple laser drives, the suppression of polariton excitation by quantum interference [42] and the proof-of-principle of a multiplexed quantum memory based on spin-waves [43] have been demonstrated.

Within this general perspective of strongly-coupled, interacting atom-light system, CQED is an outstanding platform to study phase transitions in driven-dissipative open quantum systems [44–46]. In its natural setting, a CQED system (see a generic

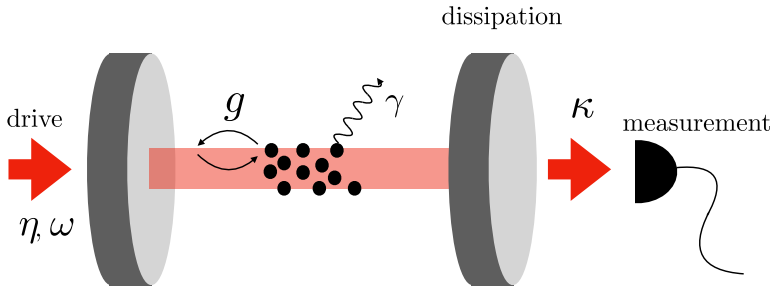


**Figure 1:** *A scheme of a generic CQED system. Atoms with natural linewidth $\gamma$ are positioned between the mirrors of an optical resonator, coupled to its mode with coupling strength $g$. The cavity is driven coherently with angular frequency $\omega$ and drive amplitude $\eta$. The cavity mode decays through one of the mirrors with rate $\kappa$ towards a detector. The evolution of the atom-cavity system takes place under the effect of the measurement back action.*

scheme in Fig. 1) is driven by external coherent sources, e.g. by laser or microwave radiation, meanwhile the energy is dissipated through a number of channels leading to a steady state resulting from a dynamical equilibrium between driving and loss [47]. One of the dissipation channels is the coupling of the cavity field to external, freely propagating, spatially well-defined modes, which can be efficiently collected for detection. The outcoupled field then affords an indirect observable of the intracavity steady state [48], in the sense of continuous weak quantum measurement. Although the intracavity system size is small, the continuously measured outcoupled field is a macroscopic observable, and it can be considered an *order parameter* of the system and the steady states can be referred to as *phases*. Transitions between phases can be affected by changing drive parameters (*control parameters*) and monitored as a macroscopic change in the recorded signal. Such driven-dissipative phase transitions have been discussed and experimentally studied recently in CQED [49–56].

In 2016, the Quantum Optics Group of the HUN-REN Wigner Research Centre for Physics started to build a CQED laboratory [57]. The aim was to realize quantum technological applications based on atoms and photons. Today, the laboratory, called *Atom-photon interface*, hosts experiments which are based on complex procedures of routinely trapping and cooling rubidium atoms, coupling them to a single mode

of a high-finesse optical resonator and observing feeble light signals by avalanche photodiodes as well as by single photon counters. By the time I joined in 2021, the group had already published experimental results [58, 59]. In the spirit of *learning by doing*, I started to use, maintain and develop the system with my colleagues. Now, I have the honour of being the first in the group to write a PhD thesis out of measurements performed in the Atom-photon interface. As a pioneering work in this sense, the present thesis (beyond its natural aim of summarizing my scientific results) also provides a detailed description of the setup, the experimental methods and the underlying principles, serving as a useful reference for both current and future members of the group.

The thesis is structured in two parts. In Part I, both the theoretical and experimental background of my work are reviewed. In Ch. 1, a semiclassical, mean-field model is invoked to describe the interaction of multiple atoms and a single mode of a high-finesse optical cavity. In Ch. 2, I describe the laboratory setup in detail: all the employed lasers and cavities are enumerated with the connections between them, elaborating on the stabilization techniques applied on them. After a brief description of the vacuum chamber and the detection system, the whole cold atom sample preparation cycle is explained. Part II is devoted to the results of the three major research projects I participated in during the three-year period spent in the Quantum Optics Group. The first study (Ch. 3) reports on the observation of a finite-size realization of a dissipative quantum phase transition (DQPT) between hyperfine ground states of cold rubidium atoms interacting with a single mode of a high-finesse optical cavity and an external laser field. The phase diagram of the phase transition is determined by means of a semi-classical mean-field model. The remarkable feature of the phase diagram is that it predicts the coexistence of two solutions, each describing a phase with atoms very close to their hyperfine ground states. Although the predicted bistability region is rather limited in range for the control parameters, the bistability effect has been confirmed by recording hysteresis curves. Enhancement of intensity fluctuations well above the shot-noise level, accompanying the phase transition, is also revealed and investigated. The second project (Ch. 4) is a theoretical study to

extend the concept of phase transitions between ground states: whether it is possible to enlarge the bistability domain and achieve phases which include pure quantum states in the thermodynamic limit? The initial idea was to consider the case when instead of the external laser field, another driven cavity mode excites the atoms. This configuration is not available in the existing experimental setup, because the free spectral range of our cavity is larger than the hyperfine splitting. However, we could study this system on the basis of the mean-field model, constructed for the first study, extending it with the dynamical variable of the new cavity mode, and another excited state of the atoms coupled to it. A non-trivial phase diagram is obtained, and the finite-size scaling of the phase transition towards the thermodynamic limit shows that pure quantum states represent the coexisting phases and, ultimately, the bistability sets in the full range of the ratio of the control parameters. The third and last work in this thesis (Ch. 5) demonstrates strong collective coupling between a subradiant atom array and undriven modes of a high-finesse optical cavity. The vacuum Rabi splitting spectrum, an evidence of the strong collective coupling, predicted by the simple linear polarizability model of the atoms, is measured in a specific geometry. The atoms, placed in an optical lattice incommensurate with the resonant wavelength, and hence forming a subradiant array, are driven by a closely resonant external laser field in a direction perpendicular to the cavity axis. The linearity and the subradiance of the scattering is confirmed by scaling with the driving power and the number of atoms, respectively. Polarization rotation, exceeding the range of the linear polarizability model, is also observed and accounted for. The results presented in this thesis were published in [T1, T2, T3], which form the basis of the corresponding chapters, and the theses formulated from page 94.

# Part I

# Prerequisites

# Chapter 1

# Theoretical background

## 1.1 Interaction of atoms with a single optical mode

In this section, a semiclassical, mean-field model is constructed for the case of many atoms interacting with a single mode of a high-finesse optical cavity. The equations of motion are derived for the atomic polarization and population, as well as for the electromagnetic field amplitude. These Maxwell–Bloch equations (and their extensions with additional modes, fields and atomic levels) are used for modelling the experiments in Ch. 3 and Ch. 5, and for deriving the main results of Ch. 4.

Let us consider $N$ identical atoms, placed at the positions $x^{(i)}$, ($i = 1, \ldots, N$) along the axis of a high-finesse linear optical resonator with resonance at angular frequency $\omega_{\mathrm{C}}$ (see Fig. 1.1). The cavity is driven by a laser field with amplitude $\tilde{\eta}$, and angular frequency $\omega$, close enough to the resonance frequency $\omega_{\mathrm{A}} = (E_e - E_g)/\hbar$ of an atomic transition, $g \leftrightarrow e$, so that we can neglect all other levels. Since the atoms are much smaller than the optical wavelengths ($248\,\mathrm{pm}$ and $780\,\mathrm{nm}$ for the radius of the Rb atom and the wavelength of its $D_2$ line, respectively), their interaction with the electromagnetic field can be described in dipole approximation, meaning that the atoms are considered to be pointlike objects with a dipole moment

$$\mathbf{d}^{(i)} = \mathbf{d}_{eg}\left(\sigma^{(i)} + \sigma^{(i)\dagger}\right), \tag{1.1}$$

where $\sigma^{(i)} \equiv \left|g^{(i)}\right\rangle \left\langle e^{(i)}\right|$ is the lowering operator, and the matrix element of the dipole moment $\mathbf{d}_{eg}$ is chosen to be real. The interaction between a dipole moment and a radiation field is represented by the Hamiltonian

$$H_{\text{dip}}^{(i)} = -\mathbf{d}^{(i)} \frac{\mathbf{D}}{\varepsilon_0}, \tag{1.2}$$

where $\mathbf{D}$ is the quantized electric displacement vector. Quantizing $\mathbf{D}$, rather than $\mathbf{E}$, is chosen to eliminate the $\mathbf{A}$-square term from the Hamiltonian, which would couple the electromagnetic modes and challenge the validity of the single mode approximation. In this picture, this is performed consistently and without additional approximations [60, 61]. The quantized electric displacement field in a single mode of the optical resonator is given by

$$\mathbf{D}\left(x,t\right) = i\epsilon\sqrt{\tfrac{\varepsilon_0\omega_{\text{C}}}{2\hbar\mathcal{V}}}\cos\left(kx\right)\left(a\left(t\right) - a^{\dagger}\left(t\right)\right), \tag{1.3}$$

where $\epsilon$ is the polarization of the field, $\mathcal{V}$ is the volume of the cavity mode, and the time dependence is carried by the creation and annihilation operators $(a^{\dagger}, a)$ in Heisenberg picture.

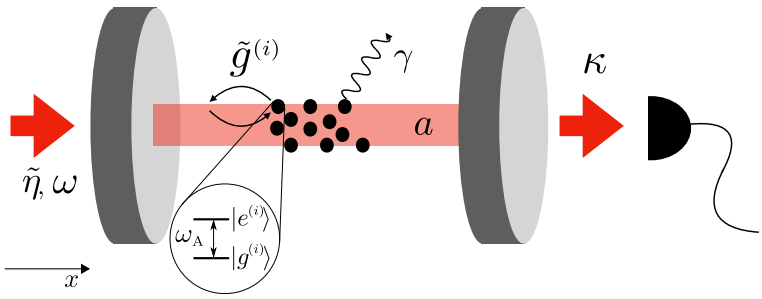


**Figure 1.1:** *Scheme of two-level atoms interacting with a cavity mode.*

The Hamiltonian of the total system consists of terms describing the free cavity mode and the free atoms, the interaction between them (1.2), and the driving of the cavity. Substituting the dipole moment (1.1) and the electric displacement field (1.3) in the expression (1.2), in the frame rotating with $\omega$, the total Hamiltonian takes the form:

$$H/\hbar = -\Delta_{\mathrm{C}} a^\dagger a - \Delta_{\mathrm{A}} \sum_{i=1}^{N} \sigma^{(i)\dagger}\sigma^{(i)} + i\sum_{i=1}^{N} \tilde{g}^{(i)} \left(a^\dagger \sigma^{(i)} - a\sigma^{(i)\dagger}\right) + i\tilde{\eta}\left(a^\dagger - a\right), \quad (1.4)$$

in the order given above, where $\Delta_{\mathrm{C}} \equiv \omega - \omega_{\mathrm{C}}$, $\Delta_{\mathrm{A}} \equiv \omega - \omega_{\mathrm{A}}$ are detunings of the laser from the cavity and from the atoms, respectively, $\tilde{g}^{(i)} = \sqrt{\frac{\omega_{\mathrm{C}}}{2\epsilon_0 \hbar \mathcal{V}}} d_{eg} \cos\left(kx^{(i)}\right)$ is the coupling coefficient between the $i$-th atom and the cavity mode (with $d_{eg}$ being the projection of the matrix element of the dipole moment to the field polarization, and $k = \omega_{\mathrm{C}}/c$ the wavenumber of the cavity mode). The terms $a\sigma^{(i)}$ and $a^\dagger\sigma^{(i)\dagger}$ have been omitted according to the rotating wave approximation (RWA), as they rotate at $\omega_{\mathrm{C}} + \omega_{\mathrm{A}} \approx 2\omega$, and average out during the time scale of the atom-cavity interaction, determined by the coupling coefficient, having the order of magnitude of several $\mathrm{MHz}$.

The conservative dynamics of an operator $\mathcal{O}$ can be straightforwardly obtained in terms of Heisenberg equations of motion:

$$\dot{\mathcal{O}} = -\frac{i}{\hbar}\left[\mathcal{O}, H\right]. \quad (1.5)$$

The dissipation of the cavity mode amplitude with a rate $\kappa$, the decay of the excited state with the spontaneous emission rate $\gamma$ can be taken into account in the Heisenberg–Langevin equations of motions [62] with the associated noise described by noise operators $\xi$, $\zeta^{(i)}$, $\vartheta_e^{(i)}$, $\vartheta_g^{(i)}$, specifically:

$$\begin{aligned}
\dot{a} &= \left(i\Delta_{\mathrm{C}} - \kappa\right) a + \sum_{i=1}^{N} \tilde{g}^{(i)}\sigma^{(i)} + \tilde{\eta} + \tilde{\xi} \\
\dot{\sigma}^{(i)} &= \left(i\Delta_{\mathrm{A}} - \gamma\right)\sigma^{(i)} + 2\tilde{g}^{(i)} a\sigma_z^{(i)} + \zeta^{(i)}, \\
\dot{n}_e^{(i)} &= -2\gamma n_e^{(i)} - \tilde{g}^{(i)}\left(\sigma^{(i)\dagger} a + a^\dagger \sigma^{(i)}\right) + \vartheta_e^{(i)}, \\
\dot{n}_g^{(i)} &= 2\gamma n_e^{(i)} + \tilde{g}^{(i)}\left(\sigma^{(i)\dagger} a + a^\dagger \sigma^{(i)}\right) + \vartheta_g^{(i)},
\end{aligned} \quad (1.6)$$

where we introduced the population operators $n_e^{(i)} = \sigma^{(i)\dagger}\sigma^{(i)}, n_g^{(i)} = \sigma^{(i)}\sigma^{(i)\dagger}$. Note

that these are not independent, as for a closed two-level atom $n_e^{(i)} + n_g^{(i)} = 1$ holds. The mean value of the noise operators is zero, and they are defined by diffusion coefficients:

$$\begin{aligned}
\left\langle \tilde{\xi}(t_1)\, \tilde{\xi}^{\dagger}(t_2) \right\rangle &= 2\kappa\, \delta(t_1 - t_2), \\
\left\langle \zeta^{(i)}(t_1)\, \zeta^{(j)\dagger}(t_2) \right\rangle &= 2\gamma\, \delta_{ij}\, \delta(t_1 - t_2), \\
\left\langle \vartheta_e^{(i)}(t_1)\, \zeta^{(j)\dagger}(t_2) \right\rangle &= 2\gamma \left\langle \sigma^{(i)\dagger} \right\rangle \delta_{ij} \delta\left(t_1 - t_2\right), \\
\left\langle \vartheta_g^{(i)}(t_1)\, \zeta^{(j)\dagger}(t_2) \right\rangle &= -2\gamma \left\langle \sigma^{(i)\dagger} \right\rangle \delta_{ij} \delta\left(t_1 - t_2\right), \\
\left\langle \vartheta_e^{(i)}(t_1)\, \vartheta_e^{(j)}(t_2) \right\rangle &= 2\gamma \left\langle n_e^{(i)} \right\rangle \delta_{ij} \delta\left(t_1 - t_2\right), \\
\left\langle \vartheta_g^{(i)}(t_1)\, \vartheta_e^{(j)}(t_2) \right\rangle &= -2\gamma \left\langle n_e^{(i)} \right\rangle \delta_{ij} \delta\left(t_1 - t_2\right), \\
\left\langle \vartheta_g^{(i)}(t_1)\, \vartheta_g^{(j)}(t_2) \right\rangle &= 2\gamma \left\langle n_e^{(i)} \right\rangle \delta_{ij} \delta\left(t_1 - t_2\right).
\end{aligned} \tag{1.7}$$

All the other first-order correlations vanish. This set of correlation functions can be derived either from a microscopic model of the dissipative processes, or simply by using the generalized fluctuation-dissipation theorem [62].

Now, if we assume that the atoms are equally coupled to the mode, that is $\tilde{g}^{(i)} \equiv \tilde{g}$ for all $i$, the coupling coefficient can be factored out, and a closed set of equations can be obtained for the collective atomic operators $\Sigma = \sum_{i=1}^{N} \sigma^{(i)}$ and $N_e = \sum_{i=1}^{N} n_e^{(i)}$, $N_g = \sum_{i=1}^{N} n_g^{(i)}$, given as:

$$\begin{aligned}
\dot{a} &= \left(i\Delta_{\mathrm{C}} - \kappa\right) a + \tilde{g}\, \Sigma + \tilde{\eta} + \tilde{\xi}, \\
\dot{\Sigma} &= \left(i\Delta_{\mathrm{A}} - \gamma\right) \Sigma + \tilde{g}\, \left(N_e - N_g\right)\, a + N\, \Xi, \\
\dot{N}_e &= -2\gamma N_e - \tilde{g}\left(\Sigma^{\dagger} a + a^{\dagger} \Sigma\right) + N\, \Theta_e, \\
\dot{N}_g &= 2\gamma N_e + \tilde{g}\left(\Sigma^{\dagger} a + a^{\dagger} \Sigma\right) + N\, \Theta_g,
\end{aligned} \tag{1.8}$$

where the noise terms are simply the sum of the individual atomic noise terms, e.g., $N\,\Xi = \sum_{i=1}^{N} \zeta^{(i)}$, keeping the atom number as a prefactor for later convenience. The use of collective atomic operators is a crucial assumption to close the set of equations,

which is exact e.g. for atoms in the antinodes of the mode, in an optical dipole lattice. This approximation is the starting point for a mean-field description of a randomly distributed ensemble of atoms when their collective behaviour is considered, such as in the experiment discussed in Ch. 3. By contrast, spatially dependent coupling coefficients must be maintained when the different positions of the individual atoms play a significant role in the dynamics, like in the case studied in Ch. 5.

The operator products in the above equations (e.g. the product $\Sigma^\dagger a$ in the evolution equation for the population $N_e$) make this problem analytically intractable. We resort therefore to the standard mean field approach, linearizing the above operator equations around the mean values. For later convenience, let us introduce scaled variables in the form of a sum of the scaled mean-field and scaled fluctuation variables, i.e., $a = \sqrt{N}(\alpha + \delta a)$, $\Sigma = N(m + \delta\Sigma)$, $N_e = N\,(n_e + \delta N_e)$ and $N_g = = N\,(n_g + \delta N_g)$. With a suitable scaling of the parameters $g = \sqrt{N}\tilde{g}$ and $\eta = \tilde{\eta}/\sqrt{N}$, the mean field variables obey the Maxwell–Bloch equations

$$\begin{aligned}
\dot{\alpha} &= (i\Delta_{\mathrm{C}} - \kappa)\,\alpha + g\,m + \eta, \\
\dot{m} &= (i\Delta_{\mathrm{A}} - \gamma)\,m + g\,\left(n_e - n_g\right)\,\alpha, \\
\dot{n}_e &= -2\gamma n_e - g\,(m^*\alpha + \alpha^* m)\,, \\
\dot{n}_g &= 2\gamma n_e + g\,(m^*\alpha + \alpha^* m)\,.
\end{aligned} \tag{1.9}$$

The linearized dynamical equations for the fluctuations read

$$\begin{aligned}
\dot{\delta a} &= (i\Delta_{\mathrm{C}} - \kappa)\,\delta a + g\,\delta\Sigma + \xi, \\
\dot{\delta\Sigma} &= (i\Delta_{\mathrm{A}} - \gamma)\,\delta\Sigma + g\,\left(\,[\delta N_e - \delta N_g]\;\alpha + [n_e - n_g]\,\delta a\right) + \Xi, \\
\delta\dot{N}_e &= -2\gamma\delta N_e - 2g\,\mathrm{Re}\left(m^*\delta a + \alpha\delta\Sigma^\dagger\right) + \Theta_e, \\
\delta\dot{N}_g &= 2\gamma\delta N_e + 2g\,\mathrm{Re}\left(m^*\delta a + \alpha\delta\Sigma^\dagger\right) + \Theta_g,
\end{aligned} \tag{1.10}$$

where $\xi = \tilde{\xi}/\sqrt{N}$. These are linear equations with the noise terms as driving. The

non-vanishing noise terms are obtained straightforwardly from their definition,

$$\begin{aligned}
\left\langle \xi(t_1)\,\xi^{\dagger}(t_2)\right\rangle &= \frac{2\kappa}{N}\,\delta(t_1-t_2),\\
\left\langle \Xi(t_1)\,\Xi^{\dagger}(t_2)\right\rangle &= \frac{2\gamma}{N^2}\,\delta(t_1-t_2),\\
\left\langle \Theta_e\left(t_1\right)\Xi^{\dagger}\left(t_2\right)\right\rangle &= \frac{2\gamma}{N^2}\left\langle \Sigma^{\dagger}\right\rangle \delta\left(t_1-t_2\right),\\
\left\langle \Theta_g\left(t_1\right)\Xi^{\dagger}\left(t_2\right)\right\rangle &= -\frac{2\gamma}{N^2}\left\langle \Sigma^{\dagger}\right\rangle \delta\left(t_1-t_2\right),\\
\left\langle \Theta_e\left(t_1\right)\Theta_e\left(t_2\right)\right\rangle &= \frac{2\gamma}{N^2}\left\langle N_e\right\rangle \delta\left(t_1-t_2\right)\\
\left\langle \Theta_g\left(t_1\right)\Theta_e\left(t_2\right)\right\rangle &= -\frac{2\gamma}{N^2}\left\langle N_e\right\rangle \delta\left(t_1-t_2\right),\\
\left\langle \Theta_g\left(t_1\right)\Theta_g\left(t_2\right)\right\rangle &= \frac{2\gamma}{N^2}\left\langle N_e\right\rangle \delta\left(t_1-t_2\right),
\end{aligned} \tag{1.11}$$

All the above diffusion coefficients vanish in the limit of large $N$.

The model above can be straightforwardly extended with other atomic levels, drives and cavity modes. Such extensions are used throughout the thesis. In Ch. 3, Eq. (3.6), another ground state $|f\rangle$ and an effective drive, $\lambda$ from $|g\rangle$ to $|f\rangle$ are introduced. In Ch. 4, Eq. (4.1), there are two excited and two ground states with two driven cavity modes. Finally, in Ch. 5, instead of the cavity, the atoms are driven, and two orthogonally polarized cavity modes are considered, however, in this problem, the mean-field equations will not be used.

# Chapter 2

# Atom-photon interface

In this chapter, I provide a detailed description of the laboratory setup used for the measurements that form the basis of my experimental results presented in this work. In the next section, I present the lasers and optical resonators employed in the setup, with emphasis on their frequency stabilization and synchronization. In Sec. 2.2, I briefly describe the vacuum chamber, in which the interaction between the cold $^{87}$Rb atoms and the photons takes place. Sec. 2.3 discusses the properties of the utilized detectors. In the final section of this chapter, I outline the typical experimental protocol.

## 2.1 Frequency stabilized lasers and cavities

Quantum optics experiments rely on frequency stabilized, continuous wave (cw) laser sources. Given that the $D_2$ line of the $^{87}$Rb has the linewidth (HWHM) of $\gamma = 2\pi \cdot 3\,\mathrm{MHz}$ [63], for precise measurements, the linewidth of the laser sources needs to be well below that. It is also important that the frequencies of these laser sources are fixed in the long term against drifts induced by a variety of environmental effects (temperature, pressure, humidity, etc.), and that they are synchronized to each other, and ultimately, to an atomic resonance as reference. In this section, we will discuss the lock chain depicted in Fig. 2.1 in detail, and see, how different lock-

ing and linewidth-narrowing techniques were utilized to reach our goal: frequency stabilized and synchronized lasers and optical resonators. The frequencies of the lasers are shown on the rubidium level scheme for comparison in Fig. 2.2. Before the detailed description of the lasers and cavities, here is a short summary of their purpose:

1. Reference laser: A laser locked to a rubidium reference, used as frequency standard for other lasers, furthermore, for optical pumping and absorption imaging.

2. Repumper laser: Whenever other lasers can pump the atoms from the $F = 2$ ground state to $F = 1$, this laser is used to compensate by pumping the atoms back.

3. MOT laser: A laser with a tapered amplifier, driving the $F = 2 \rightarrow F' = 3$ cooling transition, necessary for the magneto-optical trap.

4. 'Science' laser: A laser with tunable frequency, used to manipulate the atoms in the cavity. One part of its light drives the cavity, the other one drives the atoms directly, from up and down, in a direction perpendicular to the cavity axis (transverse drive).

5. 'Transfer' cavity: A high-finesse optical resonator, used to transfer the frequency stability of the reference laser to the 'science' cavity.

6. 'Science' cavity: A high-finesse optical resonator in the vacuum chamber where the atom-light interaction takes place.

7. '805' laser: A laser with a wavelength of $805\,\mathrm{nm}$ used to stabilize the 'science' cavity and to realize an intra-cavity optical dipole lattice.

### 2.1.1 Reference laser

Our reference laser (blue beamline in Fig. 2.1) is a Toptica external-cavity diode laser (ECDL). One portion of the beam is sent through an electro-optic modulator

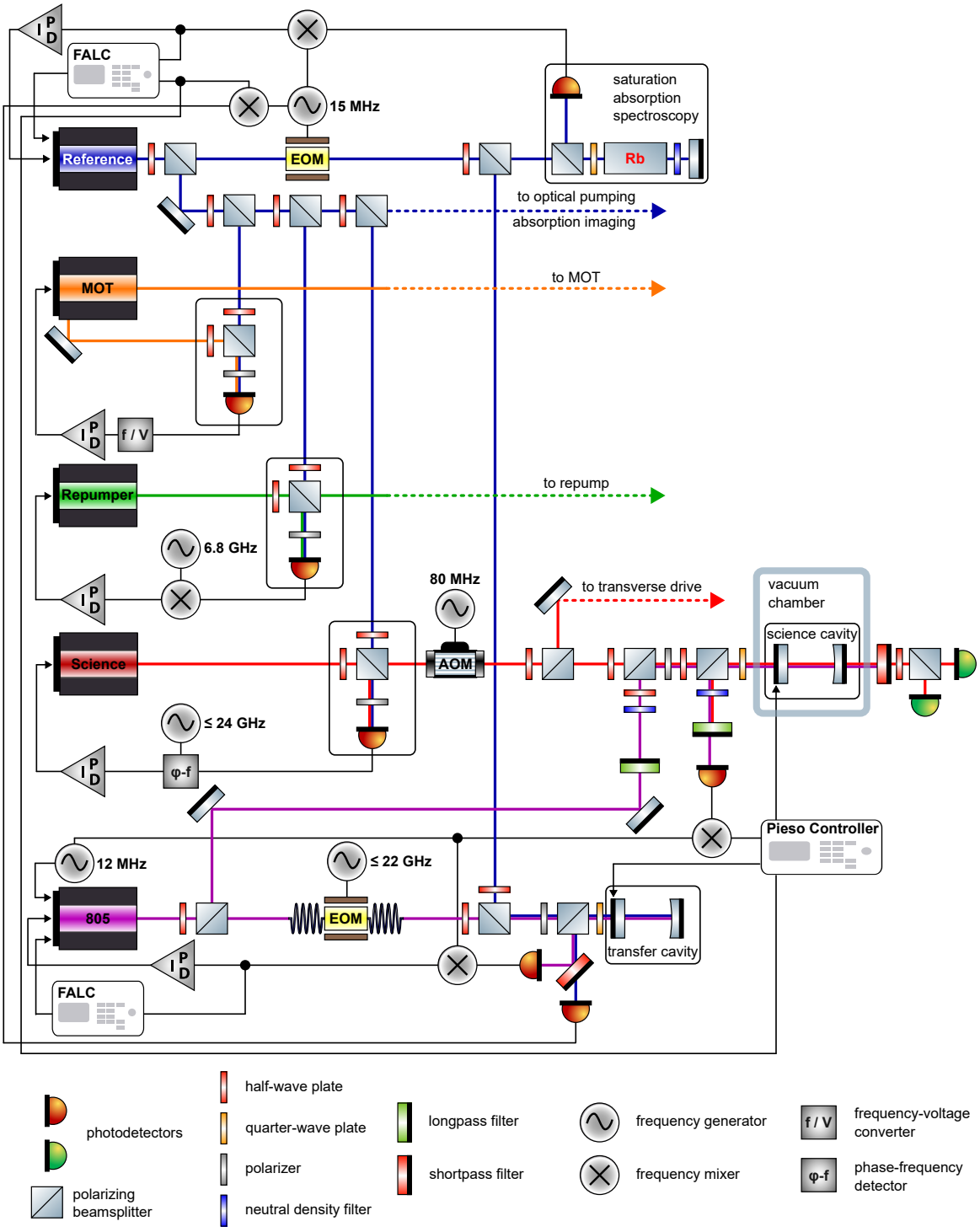


**Figure 2.1:** *Scheme of the frequency stabilized and synchronized laser sources of our CQED laboratory [64]. Laser beampaths marked with dashed lines are detailed in Fig. 2.7.*

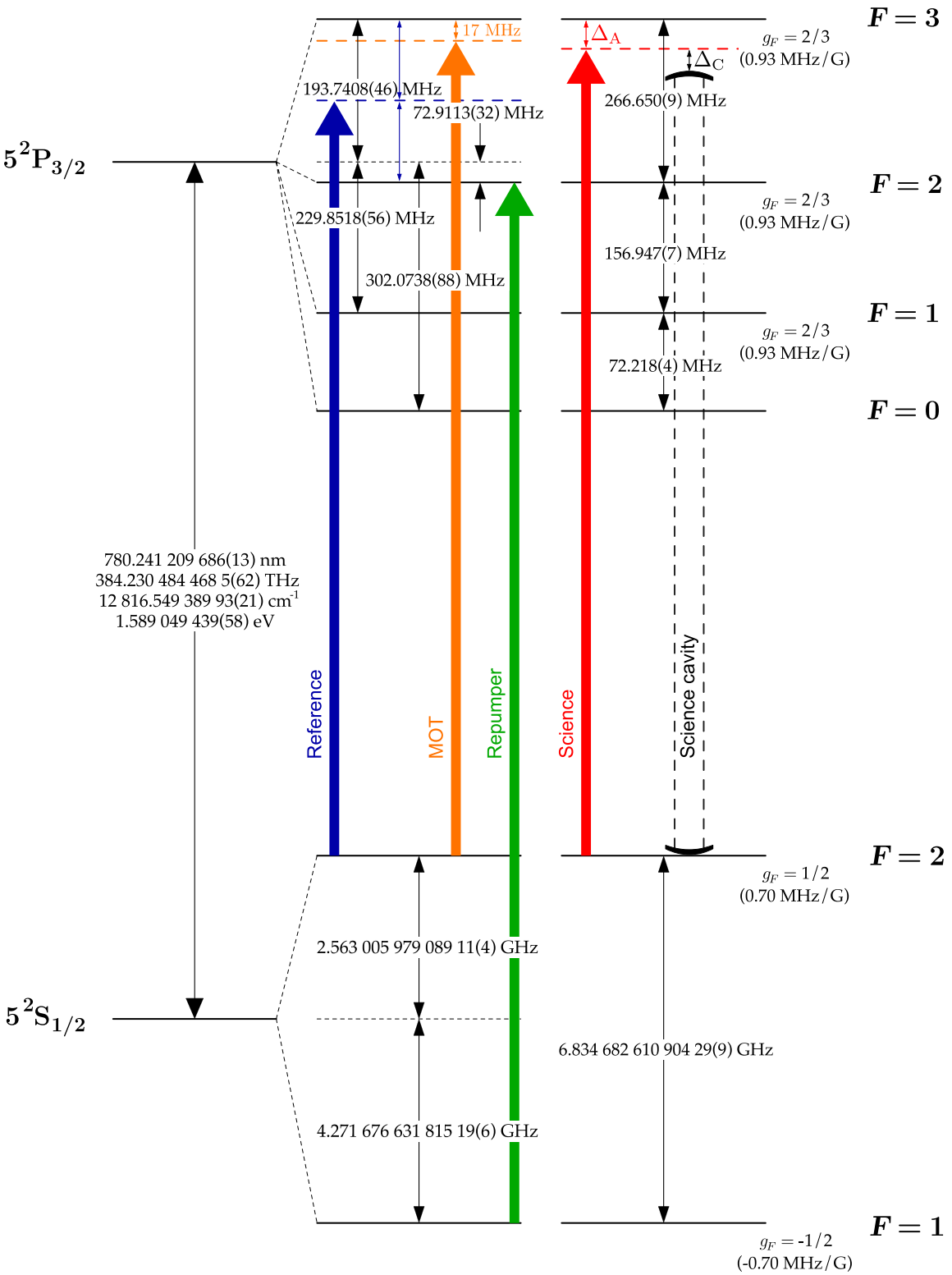


**Figure 2.2:** *Hyperfine structure of the $D_2$ line of $^{87}$Rb [63] with the frequencies of the lasers and the science cavity. Landé $g$-factors, $g_F$ and Zeeman splittings in* MHz/G *are also given.*

(EOM): a device made of a crystal whose refraction index is affected by the strength of the local electric field. The EOM is driven by a radio frequency (RF) signal of $15\,\mathrm{MHz}$, which is translated into the phase modulation of the transmitted light. The modulated light is utilized to perform frequency modulation (FM) saturated absorption spectroscopy of a room temperature rubidium cell, in order to lock the laser to the crossover resonance of the $F = 2 \rightarrow F' = 3$ and $F = 2 \rightarrow F' = 2$ transitions of the $D_2$ line of $^{87}$Rb (see Fig. 2.2). The error signal from the FM spectroscopy is fed back into the piezo voltage, as well as onto the diode current, via a Toptica Fast Analog Linewidth Control (FALC) Pro module, a high-speed linear control amplifier. With these techniques, the linewidth of the reference laser can be reduced down to $\sim 100\,\mathrm{kHz}$ (HWHM).

The reference light is utilized in different ways: the unmodulated part is divided further to give reference to other lasers for frequency stabilization, and to use it for absorption imaging and optical pumping. In order to achieve resonance with the $F = 2 \rightarrow F' = 2$ transition for imaging or the $F = 2 \rightarrow F' = 3$ transition for optical pumping, the laser frequency is shifted by $-133\,\mathrm{MHz}$ or $133\,\mathrm{MHz}$, respectively, by means of an acousto-optic modulator (AOM) in each corresponding beampath. In this device, an acoustic wave is propagated through a crystal, modulating its refraction index. The transmitted light is diffracted from the periodic structure of the refraction index profile of the crystal with a frequency shifted by multiples of the acoustic frequency, according to the diffraction order [65]. It is also utilized for fast ($\sim$ ns) switching, as the optical power gets transferred between spatially separated diffraction orders when the acoustic modulation is switched on and off.

**Saturated absorption spectroscopy**

Saturated absorption spectroscopy is a method allowing for resolving atomic resonances below the Doppler limit [66]. To this end, a pump-probe scheme is utilized (see top right in Fig. 2.1), where the probe is just the reflection of the pump, reduced in intensity by a neutral density filter. As the frequency of the laser is being swept, the pump beam addresses atoms of different velocity classes (red/blue detuned pump

excites atoms moving towards/away from the laser source). These classes of atoms are, in general, distinct for the pump and the probe. When the frequency is at the atomic resonance, those atoms are excited whose velocity is perpendicular to the beam propagation, which are the same atoms for both beams. In this case, the pump saturates these atoms, so that they become transparent for the probe. Since these atoms have a well-defined velocity ($0$ in the direction of illumination), no Doppler broadening takes place. If there are two resonances within the Doppler broadened spectrum (e.g. $\omega_1 < \omega_2$) with a shared ground state, a third absorption peak will appear in the saturated absorption spectrum, right in the middle, at $(\omega_0 = \omega_1 + \omega_2)/2$ (crossover frequency). This can be understood as follows: at the crossover frequency, the pump will saturate transition $1$ ($2$) of the atoms moving away from (towards) the source with velocity $v = c|\omega_1 - \omega_0|/\omega_0$, while the probe will address the other transition of the same atoms. Atoms in these two velocity classes will be less likely to be found in their ground state, so they will become transparent for the probe. In our case, we use the transitions $F = 2 \rightarrow F' = 3$ and $F = 2 \rightarrow F' = 2$, and the laser is locked to their crossover resonance.

**Frequency modulation spectroscopy**

A resonance peak is not ideal for a feedback error signal due to various reasons. At the top of the peak, a frequency mismatch from resonance in either direction results in the same change of the signal, and hence, the direction of the deviation cannot be determined and compensated. One side of the peak could be used, given that it is monotonous with respect to the frequency difference. The difficulty, aside from the fact that the side of the peak is not at the exact resonance, is that laser intensity noise and background light add fluctuations to the signal and can also lead to a drift of the working point.

Frequency modulation (FM) spectroscopy provides a solution to this problem [67]. According to the Kramers–Kronig relation, the dispersion of a medium changes sign at the extremal value of its absorption. This implies that a nearly resonant light (i.e. one with frequency within the linewidth of the absorption line), when propagat-

ing through the medium, gains a phase shift which is proportional to the detuning of the light from the resonance. As this is the case, if we could measure the *phase* of the light instead of its *intensity*, we would obtain a zero-crossing at the exact resonance, undisturbed by any intensity fluctuations, providing the desired error signal.

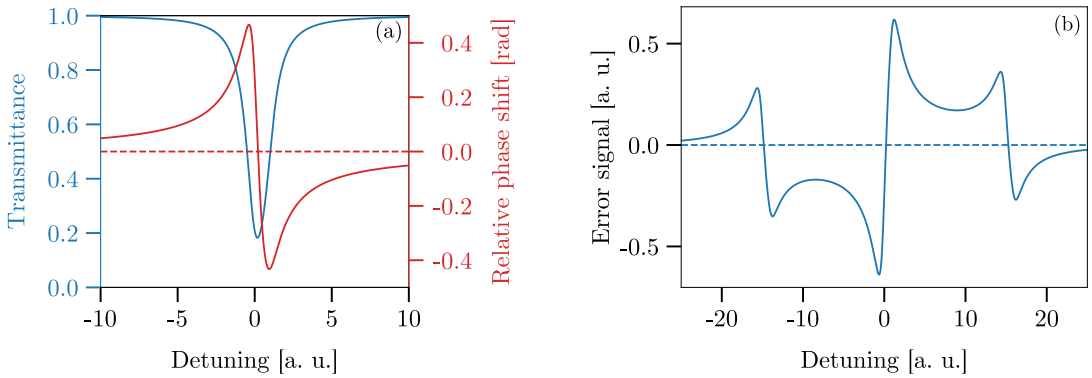


**Figure 2.3:** *Intensity and phase shift (a) of a light transmitted through a resonant medium, and the error signal (b) provided by FM spectroscopy (simulated data). The error signal provides a steep line at resonance.*

In FM spectroscopy, the light is phase-modulated with an RF signal, whose frequency is larger than the linewidth of the absorption peak. The phase modulation can be performed by an EOM or by driving the diode current with the RF signal. It generates sidebands symmetrically to the carrier, at a distance in frequency equal to that of the modulation. The interfering signal of the transmitted carrier and the two sidebands, which contains harmonics of the modulation frequency, is detected by a fast photodiode. It can be shown (see e.g. [67]) that the amplitude of one of the quadratures oscillating with the modulation frequency is proportional to the phase shift of the carrier, thus to the frequency mismatch between the laser and the resonance line. This amplitude can be extracted from the photodiode output by demodulation, that is mixing it with the RF signal used for the phase modulation, with an appropriate phase. The resulting DC signal is proportional to the frequency deviation, so that it can be used as an error signal, e.g. in a PID control loop, to lock the laser.

### 2.1.2 MOT laser

The laser used for magneto-optical trap (MOT) and polarization gradient cooling (referred to simply as MOT laser, orange beamline in Fig. 2.1) is a Toptica tapered amplifier (TA) Pro. Its seed beam is split inside the box: the main part is injected into a tapered amplifier (TA), and the amplified beam is used for experimental purposes (see in Sec. 2.4); the other, smaller portion serves to lock the frequency to that of the reference. The two beams are interfered in a fibre and the beat signal is detected by a fast photodiode. The error signal is produced from the photodiode signal by a *frequency-to-voltage converter*, an electronic device, generating a voltage output, proportional to the frequency of the sinusoidal input signal. Finally, the laser is locked $17\,\mathrm{MHz}$ below the $F = 2 \rightarrow F' = 3$ transition.

### 2.1.3 Repumper

The repumper (green beamline in Fig. 2.1) is a home-made laser, which is based on a distributed-feedback (DFB) laser diode. Its beat signal with the reference is detected with a fast photodiode, whose signal is compared to a $6.8\,\mathrm{GHz}$ local oscillator in a *phase-frequency detector*. This device outputs a voltage with a sign corresponding to the detuning if there is a mismatch between the beat and the local oscillator, and it is sensitive to the phase difference if the frequencies match. Utilizing this tool, a phase-locked loop (PLL) can be realized between two lasers by feeding back the error signal on the current of the laser diode. As a result, the repumper is locked to the reference with sub-$\mathrm{Hz}$ precision, having a frequency resonant with the transition $F = 1 \rightarrow F' = 2$.

### 2.1.4 'Science' laser

The laser that we used to manipulate the atoms in the cavity, called 'science' laser (red beamline in Fig. 2.1), was initially a Toptica ECDL, beatlocked to the reference with a frequency-to-voltage converter, the same way as we did with the MOT laser.

Later (after the experiments discussed in Ch. 3), in order to reach larger intensities, it was replaced by a Toptica TA Pro, which we phase-locked to the reference in a similar way as it is done in the case of the repumper.

The beam is split on a polarizing beamsplitter, so that one part can drive the science cavity mode along the cavity axis through one of the cavity mirrors on careful optimization of spatial mode matching, the other can drive the atoms from a direction perpendicular to the cavity axis (transverse drive).

### 2.1.5 'Transfer' cavity

A temperature stabilized high-finesse cavity (see Table 2.1 for parameters) in an invar tube is utilized to transfer the frequency stability of the reference laser to the science cavity at a wavelength far from the ones involved in the light-atom interaction effects to be studied. The length of the cavity is adjustable by means of a piezo crystal, fixed on one of the mirrors. Voltage control and feedback on the piezo is governed by a specific device, developed together with our group.

| | | |
|---|---|---|
| linewidth (HWHM) | $\kappa/2\pi$ | $0.36\,\mathrm{MHz}$ |
| finesse | $\mathcal{F}/\pi$ | $666$ |
| length | $d$ | $5\,\mathrm{cm}$ |
| free spectral range | $\nu_{\mathrm{FSR}}$ | $3\,\mathrm{GHz}$ |
| mode waist | $w_0$ | $146\,\mu\mathrm{m}$ |

**Table 2.1:** *Transfer cavity parameters. We use LaserOptik HR mirrors of* $10\,\mathrm{mm}$ *diameter. The reflectivity of both mirrors is* $R = 0.9985$*, and is closely constant over a range of* $\sim 50\,\mathrm{nm}$ *around* $790\,\mathrm{nm}$*, so the cavity parameters are the same for the two modes at* $780\,\mathrm{nm}$ *and* $805\,\mathrm{nm}$ *that we use.*

The reference light is coupled into the cavity after passing a polarizing beamsplitter (PBS), using its transmitting path, and a $\lambda/4$ plate, with the slow axis oriented at $45^\circ$ with respect to the polarization plane. This way the polarization of the light reflected from the input mirror is rotated by $90^\circ$, and gets reflected on the PBS. This reflected light is used to lock the cavity to the reference with the Pound–Drever–Hall (PDH) technique, a locking method based on FM spectroscopy, discussed above. There is a feedback loop in the opposite direction as well: the error signal of the

transfer cavity is fed back to the diode current of the reference laser using the same FALC device as for the rubidium spectroscopy. This way, the transfer cavity mode serves as a narrow-line etalon to reduce the linewidth of the reference laser, down below $100\,\mathrm{kHz}$ (HWHM).

**Piezo controller device**

A low-noise piezo controller, called 'Quantum piezo controller' was developed together with our group by R&D Ultrafast Lasers Ltd. One device is capable of handling two control loops, each corresponding to one piezo actuator attached to a cavity. Each loop has an input channel for the error signal, a high-voltage output channel for setting the workpoint ($-20\,\mathrm{V}$ to $+100\,\mathrm{V}$ with a resolution of $\sim 3.33\,\mathrm{mV}$), and a low-voltage output channel for the control signal around the workpoint ($-5\,\mathrm{V}$ to $+5\,\mathrm{V}$ with a resolution of $\sim 0.17\,\mathrm{mV}$). Additionally, there are two monitor channels for tracing both the input and the output signals.

The control is implemented by means of field-programmable gate arrays (FPGAs), handled by a front-end GUI on a computer, connected to the controller via ethernet. The workpoint (i.e. the cavity resonance) can be found by scanning the length of the cavity (in terms of the voltage on the piezo actuator), and looking for the PDH signal in the input. When the workpoint is selected, the voltage range is reduced in an automated operation by means of scans of smaller and smaller amplitudes. After this zooming process, when the scanning range is constricted to the actual error signal (the slope corresponding to the resonance), the lock can be switched on.

Each input signal is split into two paths: one goes to a fast feedback loop, realized by a PID controller, and the other to a slow one, realized by an integrator. Both parts are filtered by digital filters, in order to properly separate the fast and slow part (by means of high-pass and low-pass filters), and to rule out the mechanical resonance of the cavity holder (by means of a notch filter). The transfer function of these filters, having the form

$$H(z) = \frac{b_2 z^{-2} + b_1 z^{-1} + b_0}{a_2 z^{-2} + a_1 z^{-1} + 1}, \tag{2.1}$$

can be designed and implemented by defining the constants $a_i$ and $b_i$ between $+10$ and $-10$, with a precision of 7 decimal digits. The maximum sampling frequency of the filters is $1\,\mathrm{MHz}$. The outputs of the fast and the slow feedback are summed, this will be the control signal on the low-voltage output. If the voltage on this output reaches the edge of its working range, the workpoint is shifted, and the control signal is rewound to the opposite edge of the interval. This is done in a harmonized way, so that the two changes in the voltage with opposite signs cancel each other.

During my work, my task was to test this device, to optimize the settings (e.g. PID and digital filter parameters) with respect to lock noise and stability. I was in contact with the developer regarding occasional bugs in the software and implementing new features (e.g. the above-mentioned smooth compensation of the low-voltage output with the high-voltage one).

### 2.1.6 'Science' cavity

Another high-finesse resonator (see Table 2.2 for parameters), used for the CQED experiments, is placed inside the vacuum chamber. This is what we call 'science' cavity. It can be driven by the 'science' light, and locked by using the same electronic control device as that for the transfer cavity. The locking principle is presented in the next subsection.

| | | |
|---|---|---|
| linewidth (HWHM) | $\kappa/2\pi$ | $3\,\mathrm{MHz}$ |
| finesse | $\mathcal{F}/\pi$ | $1430$ |
| length | $d$ | $1.5\,\mathrm{cm}$ |
| free spectral range | $\nu_{\mathrm{FSR}}$ | $10\,\mathrm{GHz}$ |
| mode waist | $w_0$ | $127\,\mu\mathrm{m}$ |
| atom-mode coupling | $g/2\pi$ | $0.33\,\mathrm{MHz}$ |

**Table 2.2:** *Science cavity parameters. The arrangement of the mirrors is planoconcave, so that the mode waist is situated on the planar mirror that we use for incoupling. We use LaserOptik HR mirrors of* $5\,\mathrm{mm}$ *diameter. The reflectivity of both mirrors is* $R = 0.9993$*, and is closely constant over a range of* $\sim 50\,\mathrm{nm}$ *around* $790\,\mathrm{nm}$*, so the cavity parameters are the same for the two modes at* $780\,\mathrm{nm}$ *and* $805\,\mathrm{nm}$ *that we use. The single-atom coupling constant* $g$ *was calculated using the cavity mode volume:* $V = = \pi\, w_0^2\, d/4 \approx 0.2\,\mathrm{mm}^3$.

### 2.1.7 '805' laser

A Toptica ECDL similar to the reference is used for locking the science cavity (purple beamline in Fig. 2.1). Its wavelength must be very far from any atomic resonances so that the lock laser does not influence the atom-cavity system under study, therefore, it is tuned to $805\,\mathrm{nm}$. In order to rule out the broadband amplified spontaneous emission coming from the laser diode, which contains light at $780\,\mathrm{nm}$ resonant with the atoms, a long-pass filter is placed in the beampath just before it is combined with the science light. In the following, this laser is referred to simply as '805 laser'.

Locking a resonator near to a specific frequency with a laser detuned from that by $25\,\mathrm{nm}$ is a highly non-trivial task. The principle is illustrated in Fig. 2.4. One of the modes of the transfer cavity (upper comb in the figure) is locked to the reference, representing the atomic resonance, from which a certain detuning, $\delta = \omega_\mathrm{C} - \omega_\mathrm{ref}$ (typically in the $\mathrm{MHz}$ to $\mathrm{GHz}$ range) is to be set for one of the science cavity modes (lower comb). Sidebands are generated on a portion of the 805 light by means of a fibre-EOM driven by an RF signal with adjustable frequency. One of the sidebands of the 805 laser is locked to a mode of the transfer cavity. If $\omega_\mathrm{C}$ is set to the desired value, the carrier of the 805 light, which is to be used for locking the science cavity, misses the closest cavity mode by the amount of $\Delta$. This mismatch, which can be at maximum half of the free spectral range of the transfer cavity (i.e. $1.5\,\mathrm{GHz}$, see Table 2.1), can be bridged by the tunable RF signal that generates the sidebands on the 805 laser. If a red (blue) sideband was locked to the transfer cavity, when changing the modulation frequency, the frequency of the carrier is also changing in the same (opposite) direction.

The fixed sidebands for the PDH lock to the transfer cavity are generated by a $12\,\mathrm{MHz}$ AC modulation on the diode current. The fibre-EOM is driven by a Rohde & Schwarz Vector Signal Generator, allowing for creating the additional sidebands for the 'mode matching' at arbitrary distance from the carrier up to $20\,\mathrm{GHz}$.

It is important to note, that the lock scheme could be the other way around: one could lock the carrier of the 805 light to the transfer cavity, and lock the science

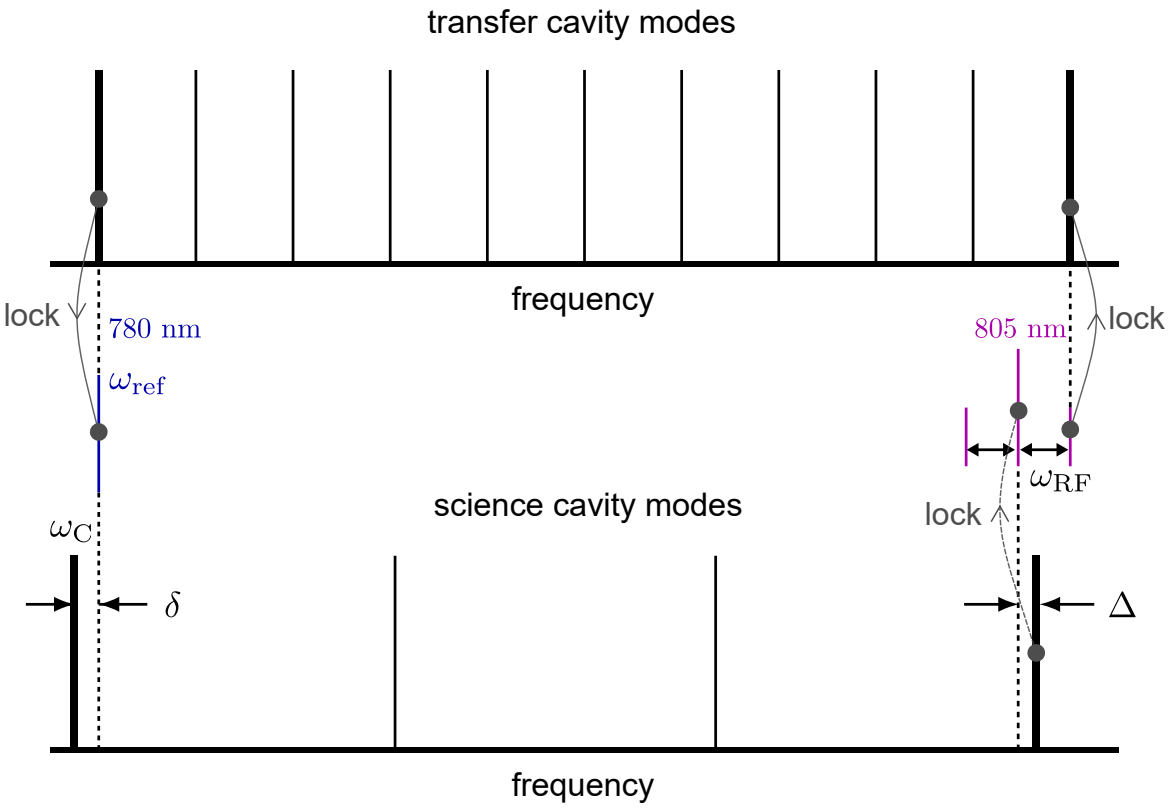


**Figure 2.4:** *Principle of locking the science cavity.*

cavity to one of the sidebands. Initially, the lock system used this latter, however, it was later realized that the higher intensity of the 805 light in the carrier injected to the science cavity can be used to create an intracavity far off-resonance trap (FORT) for the atoms in the cavity mode at the wavelength around $805\,\mathrm{nm}$ [F1].

## 2.2 Rubidium-87 atoms in the vacuum chamber

Rubidium-87 atoms are collected, trapped and cooled in a vacuum chamber. A pressure of $\sim 7 \cdot 10^{-11}\,\mathrm{mbar}$ is attained in it by applying various techniques consecutively: baking out the chamber to evaporate contaminants, using a scroll pump to eliminate them and create pre-vacuum for the turbomulecular pump, which can remove small particles, utilizing an ion pump to capture residual molecules through ionization, and finally, a titanium sublimation pump to adsorb any remnant particles by coating

the interior of the chamber with titanium. Once the ultra-high vacuum (UHV) is achieved, it is maintained by the latter two methods.

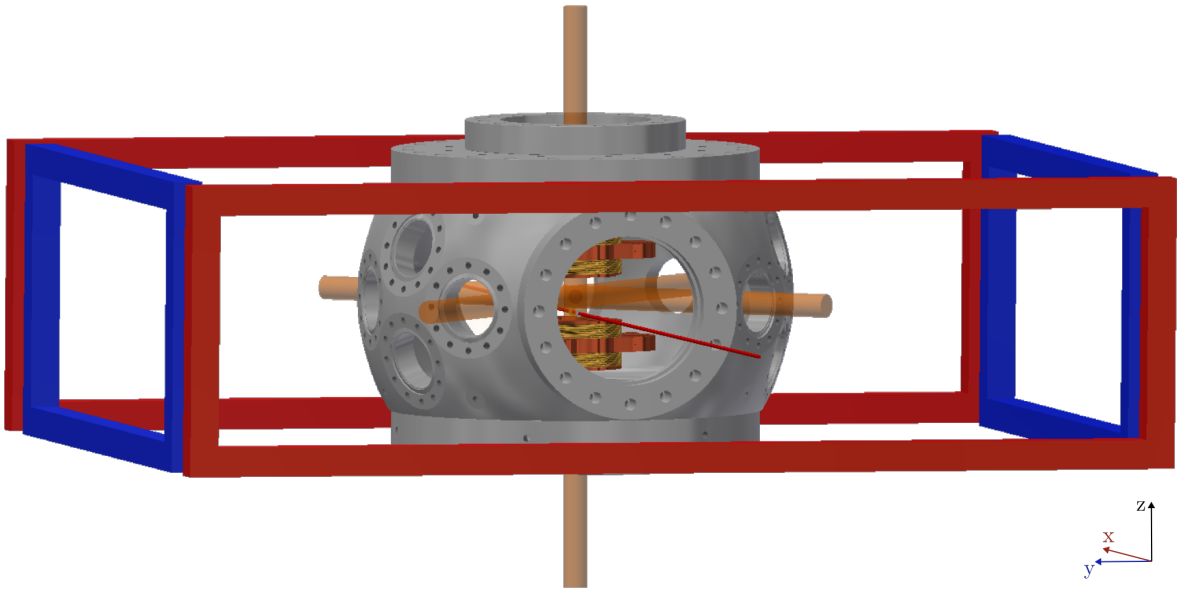


**Figure 2.5:** *Vacuum chamber surrounded by compensating coils (red and blue). Only the cavity drive (red, entering at the front flange) and the MOT beams (orange) are shown here. More detailed internal geometry of the chamber is shown in Fig. 2.6.*

Two pairs of identical cylindrical copper coils are placed in the chamber, with their axis aligned. We refer to the coils with the names `upper MOT+`, `upper MOT`, `lower MOT`, `lower MOT+`, in top-down order. There is a separation of $34\,\mathrm{mm}$ between the `upper MOT` coil and the `lower MOT` coil. The centre of symmetry defines the centre of the MOT. The chamber is surrounded by two pairs of rectangular coils (red and blue in Fig. 2.5), compensating the background magnetic field (e.g. that of the Earth) together with the intra-vacuo coils, used for MOT and magnetic trapping. All the coils are driven by HighFinesse bipolar current source (BCS) devices.

A rubidium dispenser is placed in the chamber with its opening oriented towards the centre of the MOT. When current ($\sim 3.8\,\mathrm{A}$) flows through the dispenser, Rb vapour is released due to the heat, and the atoms are captured by the MOT.

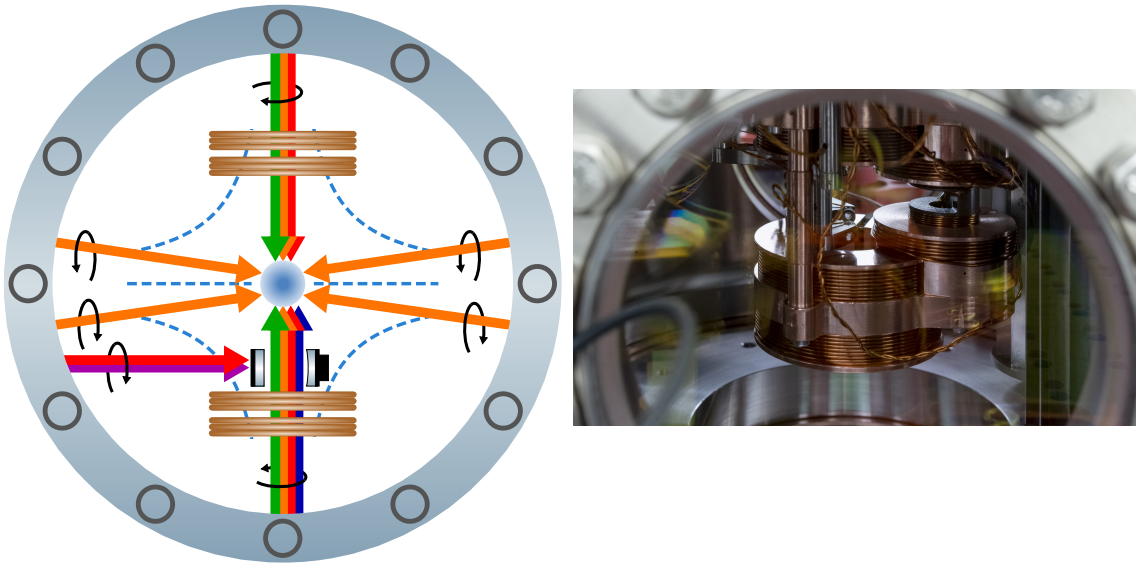

**Figure 2.6:** *Schematic drawing and photo of the insight to the vacuum chamber. The viewpoint in the drawing corresponds to the right side of Fig. 2.5, while the photo shows the front view. Laser beam colours match those used in Fig. 2.1. Further details of the beamline alignment are shown in Fig. 2.7. In the photo,* `upper MOT`*,* `lower MOT` *and* `lower MOT+` *coils are visible, with the science cavity between them. The coils on the right side of the photo are not used in the experiments discussed in present thesis.*

## 2.3 Detection

Before detection, the $805\,\mathrm{nm}$ part of the cavity output is filtered, utilizing shortpass and resonant optical filters, and split by a polarizing beamsplitter. The cavity output can be detected with an avalanche photodiode (APD) (Thorlabs APD410A/M), avalanche single photon counter (SPC) (Laser Components COUNT-500N-FC) modules or a superconducting nanowire single photon detector (SNSPD) (ID Quantique ID218). The detectors are compared in Table 2.3. The overall detection efficiency in our setup was significantly lower than the quantum efficiency of the detectors themselves. Additional fibre couplings and filtering decreased the signal intensity by a factor of 10 for the SNSPD. Later, when the SPC modules were implemented, I managed to optimize the setup and improve the cavity-to-fibre coupling, reducing the overall loss to $20\,\%$. With the upgraded configuration, the capabilities of the SPC modules were proved to be sufficient for our experiments, while having the advantage of compactness and working without cryogenic cooling.

| | SNSPD | SPC | APD |
|---|---|---|---|
| quantum efficiency at $780\,\mathrm{nm}$ | $\sim$80–95 % | $\sim$60 % | - |
| saturation | $30\,\mathrm{Mcps}$ | $20\,\mathrm{Mcps}$ | $1.5\,\mu\mathrm{W}$ |
| time resolution | $\sim$30 ps | $\sim$1 ns | 50 ns |
| dead time | 30 ns | 45 ns | - |
| dark count | $<$1 cps | $\sim$70 cps | - |
| operating temperature | $<1\,\mathrm{K}$ | $\lesssim 300\,\mathrm{K}$ | $\sim 300\,\mathrm{K}$ |

**Table 2.3:** *Comparison of the detectors employed in our laboratory. The saturation value for the single photon detectors are given in 'megacounts per second', which is in the order of magnitude of picowatt at wavelength* $780\,\mathrm{nm}$*. The operating temperature of the diode inside the SPC module is somewhat lower than room temperature, achieved by thermoelectric cooling.*

The single photon detectors are connected to an ID900 Time Controller, a time tagger capable of $\mathrm{ps}$ resolution, allowing for precise time course and photon correlation measurements. During my work, my task was to set up the optical connection to the single photon detectors, and to implement the time tagger into the software control of the experiment. Given that the single photon counters are very sensitive devices, the background light, scattering into the fibres via the incouplers or infiltrating through their cladding, could produce a noise comparable to the measured signal. By careful shielding of the coupling setups and the fibres themselves, we could reduce this noise down to the intrinsic dark count rate of the detectors. We made test measurements, and improved further the signal-to-noise ratio by spectral filtering of the cavity output and increasing the efficiency of its coupling into the optical fibres (up to 80%).

## 2.4 Experimental protocol

Each experiment begins with a cold atom sample preparation cycle, which varies only in its specific parameters (e.g. time duration of steps). In this section, I will follow the protocol step by step, describing the corresponding configuration (see Fig. 2.6 for the interior of the chamber and Fig. 2.7 for the geometry of the optical alignment) and outlining the actions to be taken. The protocol is illustrated by means of 'timelines':

these plots show the values to which the devices are set, as functions of time.

The whole experimental sequence is controlled by an ADwin-Pro II real-time process controller, that allows for timing digital and analogue output signals with a precision of $500\,\mathrm{ns}$, and acquire analogue input signals with a resolution down to $250\,\mathrm{ns}$. For defining experimental sequences (and generating the timelines), we use a Python front-end developed in our group.

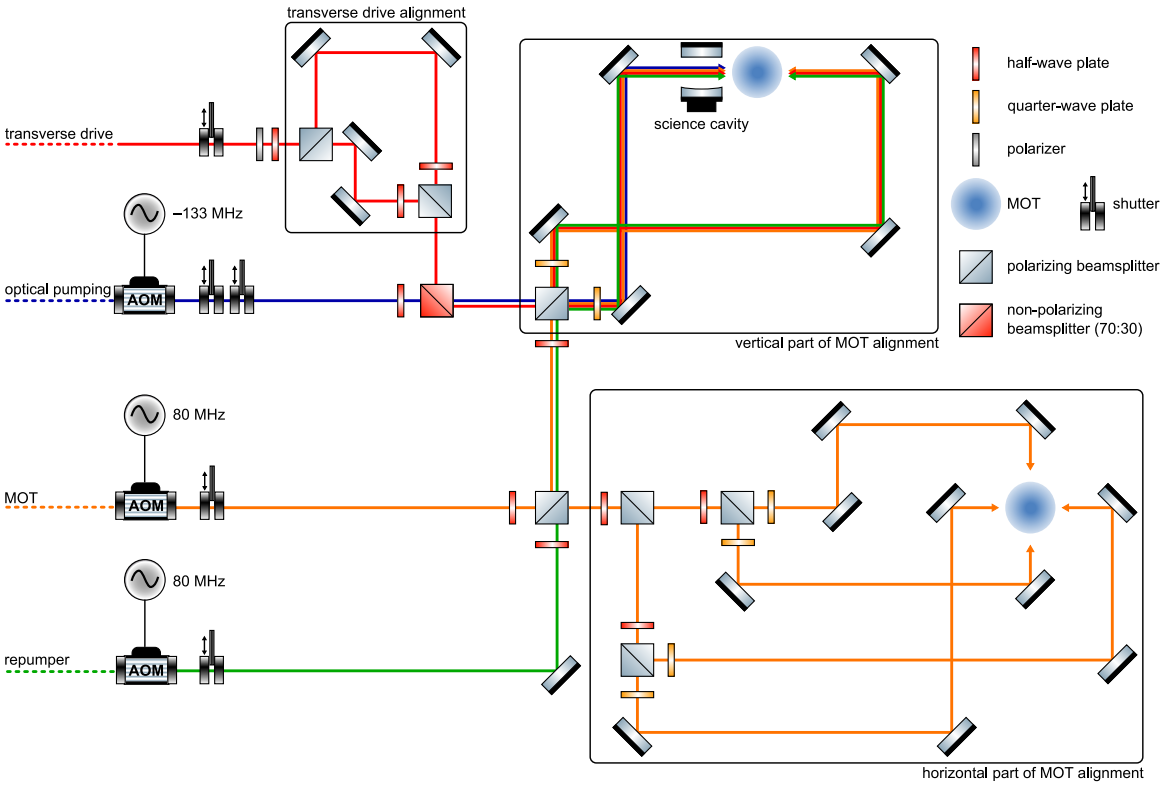


**Figure 2.7:** *Beamline alignment and control scheme. Dashed lines are the continuation of those in Fig. 2.1. Transverse drive is divided and reunited before joining the optical pumping beam to allow for adjustment of the two directions independently of the MOT beams.*

### 2.4.1 Magneto-optical trapping

Magneto-optical trapping is the standard method to produce cold atomic sample with high density and large atom numbers [68]. In the usual configuration the atoms are illuminated by three counter-propagating $\sigma^+ - \sigma^-$ pairs of red detuned laser

beams, while a quadrupole magnetic field is present, centred at the intersection of the optical beams. The principle of operation lies in the spatially varying Zeeman shift on the atoms, caused by the inhomogeneous magnetic field. This leads to a spatially dependent radiation pressure force, induced by the laser fields, restoring the atoms towards the trap centre. At the same time, velocity dependence arises from the Doppler effect, and leads to motional damping (Doppler cooling). As a result, this trap simultaneously confines spatially and cools the atoms.

The quadrupole magnetic field, needed for the trap, is generated by the `upper` and `lower MOT` coils, driven in anti-Helmholtz configuration, by $-0.98\,\mathrm{A}$ and $-1\,\mathrm{A}$, respectively. Six independently adjustable laser beams, derived from the TA laser constitutes the optical part of the MOT, the counter-propagating $\sigma^+ - \sigma^-$ pairs in each dimension. Each direction is separated from a common beam by means of polarizing beamsplitters, and the proper polarizations are achieved by quarter-wave plates. The beam waist was $12\,\mathrm{mm}$ during the experiment in Ch. 3 and $9\,\mathrm{mm}$ during the one in Ch. 5. The detuning from the cooling transition of the atoms ($F = 2 \rightarrow F' = 3$ in our scheme) is $-17\,\mathrm{MHz}$ determined experimentally to balance a high velocity capture range with low temperature. Lower temperature can be achieved with larger detuning at the cost of smaller capture range. That being the case, at the end of the MOT phase, when the cloud is already in a steady state, the laser is detuned further (see Fig. 2.8).

Driving the $F = 2 \rightarrow F' = 3$ by the MOT beams, though off-resonantly, excites the $F = 2 \rightarrow F' = 2$ transition as well, opening an escape channel for the atoms from the cooling cycle towards the $F = 1$ ground state. In order to restore the atoms to the $F = 2$ ground state, another tone, a repumper is illuminating the atoms constantly during the MOT phase, driving the $F = 1 \rightarrow F' = 2$ transition resonantly. This beam is joined to the vertical beams of the MOT at the point where the vertical and the horizontal directions are split (see Fig. 2.7). It illuminates the atoms from up and down in equal measure (power: $4\,\mathrm{mW}$ per direction, waist: $12\,\mathrm{mm}$).

Approximately $10^6$ atoms are collected over a time duration of $\sim$1–$30\,\mathrm{s}$. Their temperature at this stage is $\sim 150\,\mu\mathrm{K}$. The fluorescence image of the cloud is con-

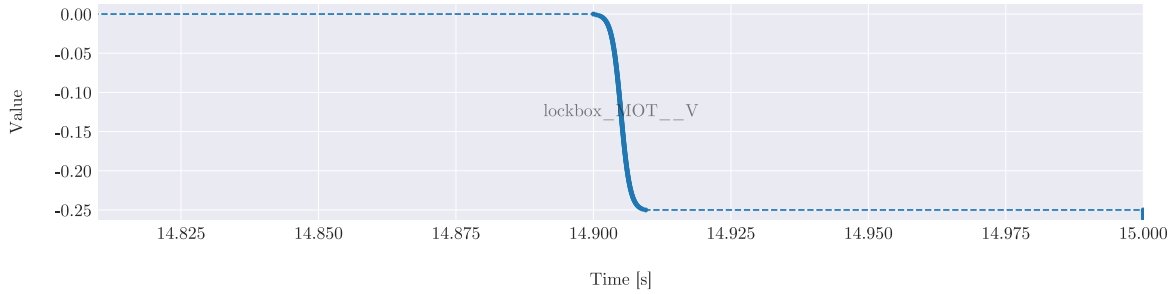


**Figure 2.8:** *Tuning the MOT laser at the end of a* $15\,\mathrm{s}$ *long MOT phase. For the last* $90\,\mathrm{ms}$ *of the collection phase, the MOT laser is detuned further by* $-5\,\mathrm{MHz}$ *in* $10\,\mathrm{ms}$ *as a means of achieving lower temperature. Shifting the frequency is carried out by ramping the offset voltage on the frequency-voltage converter ('lockbox'). The names written on the timeline graphs correspond to the quantity or device in question, used also in the software control, containing the unit of the quantity for analogue signals (e.g.* `__V` *means volt).*

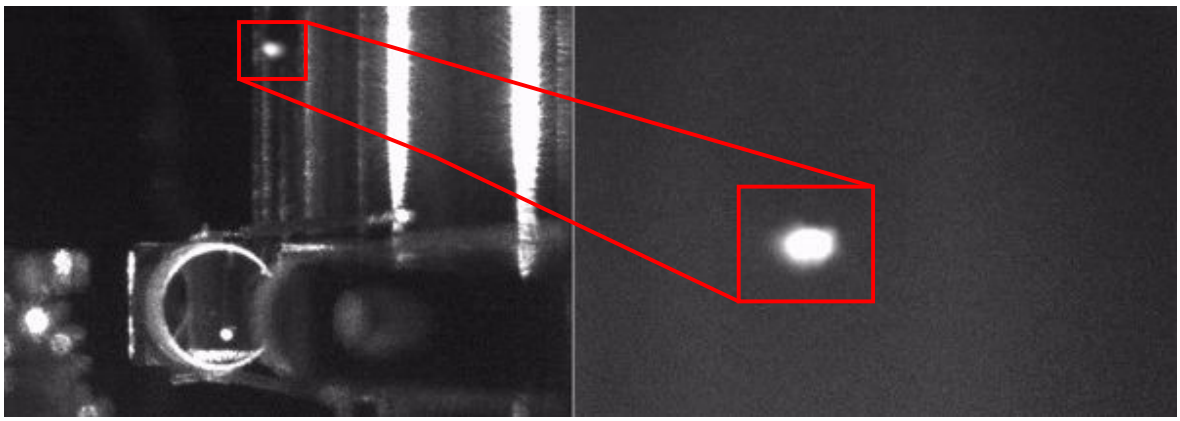

**Figure 2.9:** *Fluorescence images of the atomic cloud in the magneto-optical trap. The left image also shows the science cavity below the cloud, with the resonant mode spot visible on the incoupling mirror. The right image captures the same cloud from a perpendicular viewpoint, with a closer zoom.*

stantly monitored for diagnostic purposes with a CCD camera placed at one of the viewports of the vacuum chamber (see Fig. 2.9).

### 2.4.2 Polarization gradient cooling

Cooling below the Doppler limit ($146\,\mu\mathrm{K}$ for the $D_2$ line of $^{87}$Rb [63]) can be achieved by methods based on laser polarization gradients [20]. There are two radically different approaches to realize such a scheme with counter-propagating laser beams:

either the waves have orthogonal linear polarizations or orthogonal circular polarizations. The two methods operate on different principles, have different friction coefficients and velocity capture ranges. In our system, the $\sigma^+ - \sigma^-$ configuration is implemented, so the brief explanation here is restricted to that case.

The net polarization in this case is linear, and rotates around the propagation axis with a periodicity of the wavelength. When an atom is moving in such a field, in the frame moving with the atom and rotating in accordance with the local polarization, an extra inertial interaction will take place, coupling together the external and internal degrees of freedom (the velocity and the angular momentum) of the atom. This coupling leads to a motion induced population difference among the Zeeman sublevels of the ground state, resulting in an imbalance between the radiation pressures of the two counter-propagating waves, realizing a net friction force on the atom.

The same MOT beams at detuning $-107\,\mathrm{MHz}$ are utilized to perform polarization gradient cooling. The repumper remains on during the cooling to prevent the escaping mechanism discussed at the MOT phase. Unlike magneto-optical trapping, polarization gradient cooling is performed without any magnetic field. In fact, for an efficient polarization gradient cooling, it is crucial to completely eliminate the background magnetic field and achieve degeneracy of the different magnetic sublevels [69]. The appropriate currents, driving the external coils ($I_x = 0.25\,\mathrm{A}$, $I_y = 1.5\,\mathrm{A}$ for the red and the blue coil in Fig. 2.5, respectively) and the `MOT` coils ($I_z = -0.1\,\mathrm{A}$), compensating the background magnetic field, were found in an iterative process, where we optimized for the lowest temperature of the cloud. The external coils are driven continuously throughout the protocol at the compensation values, while the compensating current on the `MOT` coils is added to the operating currents as an offset.

The magnetic fields are switched off in $1\,\mathrm{ms}$, and the lasers are on for $4.5\,\mathrm{ms}$. Temperatures of $\sim$10–$20\,\mu\mathrm{K}$ of the atom cloud have been achieved.

### 2.4.3 Optical pumping

The process of gathering atoms in a specific quantum state is called optical pumping. A homogeneous magnetic field is necessary to define a quantization axis, and to lift the degeneracy of the Zeeman sublevels. The atoms are excited by a resonant, circularly polarized light pulse with a duration of a few tens of microseconds, propagating along the direction of the magnetic field. Each time an atom absorbs a circularly polarized photon, its $m_F$ quantum number changes by 1 (with a sign according to the handedness of the polarization and the direction of the magnetic field). When the atom relaxes, $m_F$ changes randomly by plus or minus 1, or does not change at all (for $\sigma^+$, $\sigma^-$ and $\pi$ transitions, respectively). As a result, after several cycles (in tens of microseconds), the atoms end up in an extremal $m_F$ state (stretched state). Optical pumping has to be kept short because this illumination by resonant light induces heating of the cloud.

The optical pumping beam is derived from the reference laser by tapping it with a polarizing beamsplitter, then frequency-shifted by $-133\,\mathrm{MHz}$ using an AOM, so that it drives the $F = 2 \rightarrow F' = 2$ transition resonantly. It is combined with the vertical beam path of the MOT and the repumper at the beamsplitter where the up-down and down-up directions are separated. The optical pumping beam goes only in one direction (from down to up), since there must be only one circular polarization present. Using $\sigma^+$ polarization, the atoms are pumped in to the $F = 2, m_F = 2$ ground state. The repumper laser is still switched on in this stage as well.

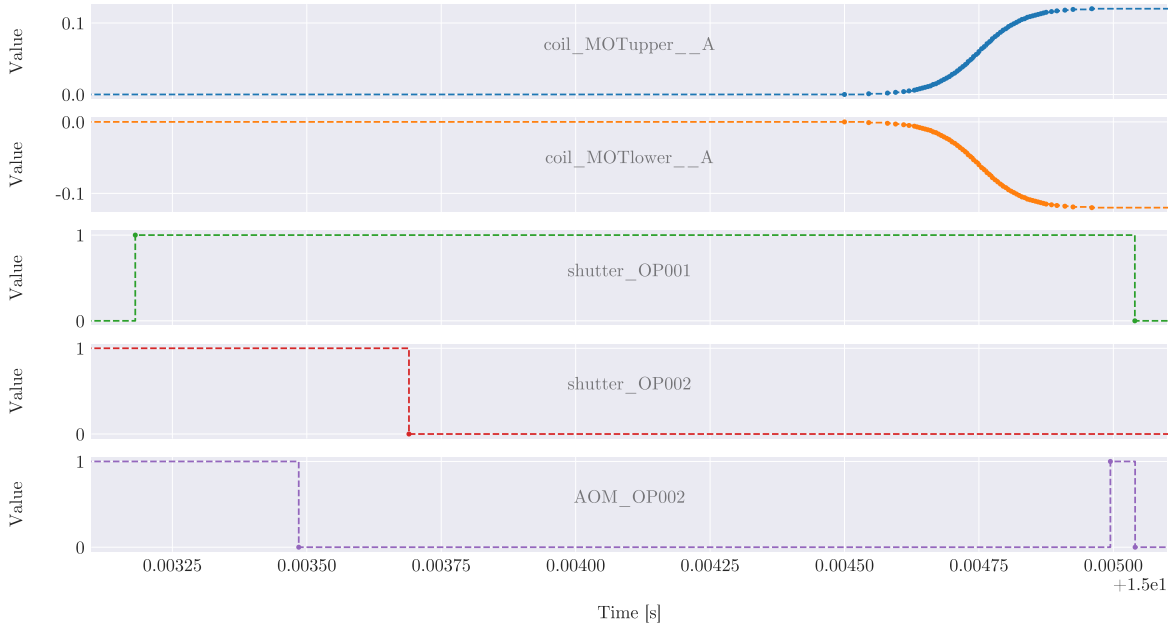


**Figure 2.10:** *Timeline of optical pumping. The* `MOT` *coils are driven with a small* ($120\,\mathrm{mA}$) *current in Helmholtz configuration to generate a weak* ($\sim 1\,\mathrm{G}$)*, homogeneous, vertical magnetic field defining the quantization axis. With the aim of fast switching, two shutters are placed in a row and operated consecutively. The AOM opens in the short time window* ($\sim 0.5\,\mathrm{ms}$) *when the two shutters are simultaneously open. Opening and closing only one shutter would result in a longer time window) due to its lag* ($1.5\,\mathrm{ms}$)*. The trigger for the operation of the two shutters precedes that of the AOM because of the lags of the shutters. Both shutters are reset afterwards to their initial position (closed for no. 1, open for no. 2, the latter not shown here), allowing for an additional optical pumping on demand. The AOM is kept on from the beginning of the experimental cycle, in order to maintain a steady working temperature, and avoid switching transients.*

### 2.4.4 Magnetic trapping

Particles with magnetic moment, $\boldsymbol{\mu}$ in a magnetic field, $\mathbf{B}$ experience a potential, given by $U = -\boldsymbol{\mu} \cdot \mathbf{B}$. A pair of coils driven in anti-Helmholtz configuration, produces a quadrupole field, which creates a linear potential for these particles. The magnetic moment of an atom is proportional to its $m_F$ quantum number and its $g_F$ Landé factor, and directed parallel (for $m_F > 0$) or antiparallel (for $m_F < 0$) to the local magnetic field. Atoms with positive (negative) $m_F$ states are trapped (repelled) by the potential, and those with $m_F = 0$ remain untouched. In the previous optical pumping step, the atoms were prepared in the $F = 2, m_F = 2$ ground state with the aim of achieving the most efficient trapping possible, as this state yields the largest

magnetic moment.

After the optical pumping, when ramping the magnetic field from homogeneous into quadrupole, a point with zero magnetic field sweeps along the vertical axis, settling finally in the centre of the quadrupole magnetic trap. For atoms being at a magnetic field zero point, the direction of the magnetic moment is undefined. This can lead to the so-called Majorana spin flip, when the magnetic moment changes sign, and the atom escapes from the trap. In order to decrease this effect, the ramp starts with a quick 'initial catch', and then the field is strengthened (see the timeline in Fig. 2.11).

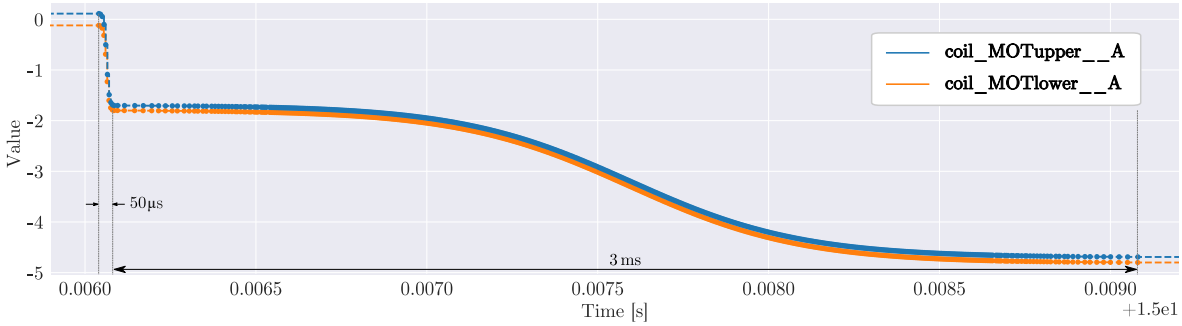


**Figure 2.11:** *Timeline of the magnetic trapping. The homogeneous field is quickly ramped into a quadrupole over a period of* $50\,\mu$s *('initial catch'), then strengthened in* $3\,$ms *to strength* $66\,\mathrm{Gcm}^{-1}$.

Approximately $5 \cdot 10^5$ atoms are collected in the magnetic trap. Their temperature is close to that achieved by the polarization gradient cooling, but due to imperfect matching of the centre of the magnetic trap and that of the cloud, additional heating can take place.

### 2.4.5 Magnetic transport to the cavity

The magnetic transport from the MOT centre to the cavity is performed by lowering the centre of the quadrupole magnetic trap adiabatically. The ramps follow a smooth function (tangent hyperbolic), in order to avoid sudden jerks (see the timeline in Fig. 2.12 and the nonlinear displacement of the cloud in time in the absorption-image sequence in Fig. 2.13). Since the vertical distance between the MOT centre and the

cavity is $\sim$11 mm, and the separation of the MOT coils is 34 mm, the transport brings the cloud close to the lower MOT coil. The shape of the magnetic quadrupole would therefore be strongly distorted if we used only a single coil pair. This is the reason for using the MOT+ coils.

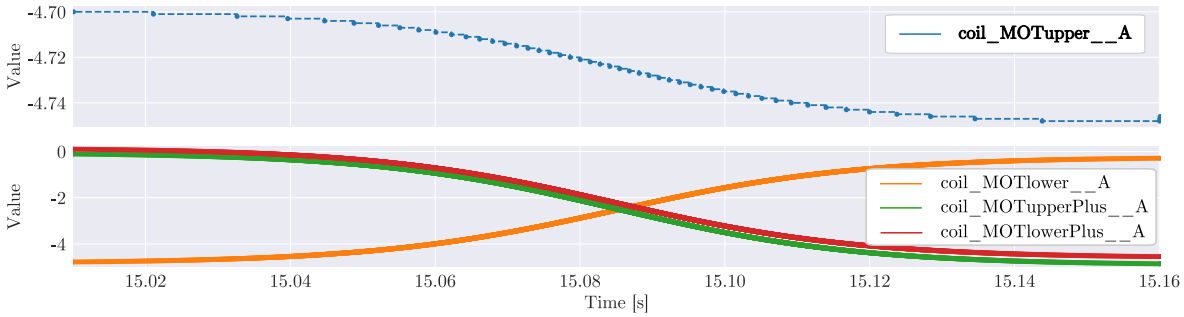


**Figure 2.12:** *Timeline of the magnetic transport. The currents in the coils are ramped asymmetrically to lower the zero-field centre of the trap towards the cavity axis. Up to small corrections from optimization, the current in the* lower MOT *coil is 'transferred' to the* lower MOT+ *coil, the current in the* upper MOT+ *coil is ramped up to the same value as in the* upper MOT *coil, while the latter is kept constant.*

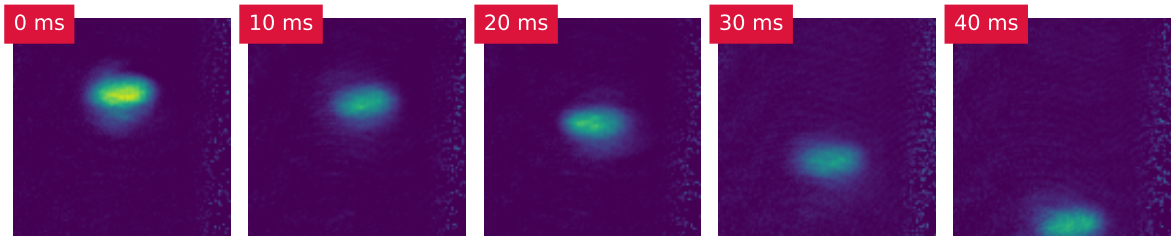


**Figure 2.13:** *Absorption images of an atomic cloud during magnetic transport.*

After the magnetic transport, the experiment protocol can vary significantly (e.g. maintaining the magnetic trap or releasing the atoms; different laser drives can be applied etc.). The subsequent steps are detailed therefore in the chapters corresponding to the individual experiments. Here, only one more possible step is described in general, loading the atoms into an intra-cavity dipole lattice.

### 2.4.6 Intra-cavity dipole lattice

Atoms in a standing wave, red detuned from resonance, experience a periodic potential, with minima in the antinodes, proportional to the intensity of the field. This

potential is called optical dipole lattice [70]. As the 805 light is coupled into the science cavity mode, the wavelength being far red detuned from any resonance in question, there is an optical dipole lattice in the cavity.

Due to the large volume mismatch of the traps, loading the atoms into this lattice from the magnetic trap is a non-trivial task, worked out and optimized by our group [F1]. The crucial parameter for the optimization is the transport position, which could be varied in horizontal direction by superimposing homogeneous magnetic fields on the quadrupole by the external coils, and in vertical direction by changing the transport parameters, i.e. the currents on the `MOT` and `MOT+` coils. At the optimized position, the magnetic trap is switched off in $7\,\mathrm{ms}$, and the atoms remain in the dipole lattice for up to $200\,\mathrm{ms}$. An ongoing project is to switch off the magnetic trap and ramp up the optical intensity simultaneously. This approach avoids the issue when atoms, falling into an already existing, conservative potential, escape from the optical lattice with their initial energy. By gradually strengthening the laser intensity as the magnetic trap is turned off, the atoms are expected to be captured more effectively, providing a controlled and efficient transfer.

# Part II

# Scientific results

# Chapter 3

# Ground state bistability of cold atoms in a cavity

## 3.1 Introduction

Driven-dissipative open quantum systems, such as atoms in a laser-driven cavity, can realize phase transitions, where the *phases* are steady (quantum) states of the system, arising from the dynamical equilibrium of drive and loss. By tuning one or more of the system parameters, called *control parameters*, the phase of the system can continuously change, or it can happen that there is a phase transition to another phase, accompanied by enhanced fluctuation and abrupt change of a macroscopic observable, called *order parameter* [71]. It gives information about the system state via a continuous measurement, e.g. the signal obtained from a photodetector monitoring the cavity output field. According to the Ehrenfest classification of phase transitions, those characterized by a discontinuity in the order parameter are called *first-order* phase transitions, while those with a discontinuity in the first derivative of the order parameter are referred to as *second-order* phase transitions [72]. The focus of my research described in this chapter was on a cavity QED system where two phases can coexist in the form of a statistical mixture with macroscopically distinct order parameters. The order parameter is continuous, however, as the system transitions between

the two phases in a finite size realization, the order parameter jumps between the corresponding two values. In the following, we describe in more detail this bistability type of phase transitions.

Phase transitions in open quantum systems, called *(driven-) dissipative quantum phase transitions (DQPTs)* [73–80], can be treated in the density operator formalism [81]. The density operator, $\rho$, describing the state of an open quantum system, obeys a master equation,

$$\dot{\rho} = \mathcal{L}\rho, \tag{3.1}$$

where $\mathcal{L}$ is a linear superoperator (in Markovian approximation, it is the so-called Liouvillian superoperator) acting on the density operator. In this formalism, the steady state, $\rho_{\rm ss}$ is defined by the homogeneous linear equation

$$\mathcal{L}\rho_{\rm ss} = 0. \tag{3.2}$$

Both $\mathcal{L}$, containing the parameters of the system, and $\rho_{\rm ss}$, its eigenoperator, depend on the control parameters, collectively denoted here by $\eta$. The order parameter is the expectation value, $\mathrm{Tr}\,(\rho\mathcal{O})$ of an observable, $\mathcal{O}$, which discriminates between the phases. The steady state, $\rho_{\rm ss}$ of the system, showing the phase transition with a bistability region, can be written in the form

$$\rho_{\rm ss}(\eta) = w(\eta)\cdot\rho_1 + (1-w(\eta))\cdot\rho_2, \tag{3.3}$$

where $\rho_1$ and $\rho_2$ yields different expectation values of $\mathcal{O}$, and the weight function $w(\eta)$ reads:

$$\begin{aligned} w = 1 \quad & \text{if} \quad \eta < \eta_{\rm crit,1} \\ 0 < w < 1 \quad & \text{if} \quad \eta_{\rm crit,1} < \eta < \eta_{\rm crit,2} \\ 0 \quad & \text{if} \quad \eta_{\rm crit,2} < \eta. \end{aligned} \tag{3.4}$$

As the weight factor varies smoothly, there is no jump in the order parameter as-

sociated with $\rho_{\rm ss}$. However, the system is under continuous measurement, therefore, only one of the two macroscopically distinct solutions, $\rho_1$ and $\rho_2$ can be present at a time. The two phases are separated temporally, leading to a series of spontaneous jumps of the order parameter in the form of a random telegraph signal. Note that neither $\rho_1$ nor $\rho_2$ is an eigenstate of $\mathcal{L}$ in general, as the steady state is the statistical mixture of the two, given by (3.3), with the weight function $w(\eta)$. However, in the *thermodynamic limit*, defined specifically for the system in question, the coupling between them decreases, and both become steady state. On approaching the thermodynamic limit, the dwelling times in the telegraph signal diverge, and ultimately it is the prepared initial state which determines the phase in the bistability domain.

My first project was an experimental investigation of a system, realizing a DQPT, which is conjectured to belong to the above described class. It was inspired by an experiment, performed previously by the group [59]. The dynamics of the collapse of an unstable phase, the so-called transmission-blockaded phase was observed with high time resolution. Transmission-blockade-breakdown (TBB) was shown to be a dynamical phase transition of a system prepared initially in a metastable phase. The phases are realized by different hyperfine ground states of cold atoms accompanied by macroscopically distinct photon populations in a single mode of a driven optical resonator [82–85]. When the atoms are in the ground state of the cavity-coupled dipole transition, the cavity transmission is inhibited due to the large resonance shift effect. The blockade can be broken down by enhancing the strength of the laser drive, which breakdown involves the atomic ground state population being transferred to another hyperfine ground state uncoupled to the resonator field. In the density operator formalism outlined above, there is a 'dark' (D) and a 'bright' (B) phase,

$$\begin{aligned} \rho_{\rm D} &= |0\rangle\langle 0| \otimes |g\rangle\langle g| \\ \rho_{\rm B} &= |\tilde{\alpha}\rangle\langle\tilde{\alpha}| \otimes |f\rangle\langle f| \end{aligned} \tag{3.5}$$

with $|g\rangle$ and $|f\rangle$ denoting the two hyperfine ground states, $|0\rangle$ and $|\tilde{\alpha}\rangle$ standing for the vacuum state and the coherent state of the cavity mode with mode amplitude

$\tilde{\alpha}$, respectively. The control parameter is the cavity drive amplitude, $\tilde{\eta}$, the order parameter is the mean cavity photon number, 0 and $|\tilde{\alpha}|^2$ in the dark and the bright phase, respectively.

This effect can be considered the extension of the photon-blockade-breakdown (PBB) phenomenon, known from single- or few-atom CQED [86, 87], to many-atom CQED systems. Whereas with PBB, a large cooperativity $\mathcal{C} = \tilde{g}^2/(\gamma\,\kappa)$ is needed at the single-atom level ($\tilde{g} \gg \kappa, \gamma$), for TBB, the large cooperativity $\mathcal{C} = N\tilde{g}^2/(|\Delta_{\rm A}|\,\kappa)$ is achieved by increasing the number of atoms, $N$, i.e. by reaching the "collective strong coupling regime" (the same notation is used here for the CQED parameters as in Ch. 1).

The goal of the research presented below was to reverse this transition by means of an additional laser field applied on the atoms, which stabilizes the otherwise only metastable transmission-blockading phase. With this, we aimed to confirm the previously proposed explanation of the mechanism underlying the observed effect, and demonstrate the coexistence of phases, which supports the classification of the TBB phenomenon as a type of first-order phase transition.

In the present study, the system involves thus two control parameters provided by tunable laser drive powers. One of the lasers is used to probe the transmission of the resonator, whose driven mode is coupled to an atomic transition. When the atoms are in the ground state of the cavity-coupled dipole transition, the resulting transmission blockade can be broken down by enhancing the strength of this laser drive. The other laser effectively repumps the atoms back into the hyperfine ground state that is coupled to the cavity.

In the theoretical limit of infinitely strong repumper, the well-known scenario of the atomic-saturation-induced optical bistability in an effectively two-level system is recovered [88–91]. Decreasing this control parameter, that is, with finite repumper, the system still exhibits bistability with the cavity drive strength control parameter, however, the role of saturation is taken over by populating another hyperfine ground state. Ultimately, the bistability develops into the statistical mixture of two *phases* in which the internal electronic state of the atoms in the cloud is a pure collective

state: all atoms are in either one or the other of the two hyperfine ground states. The extreme limit of zero repumper corresponds to the above-mentioned TBB effect. In the following, we will explore the full phase diagram spanned by the two control parameters, invoking a semiclassical mean-field theory.Experimentally, we observed hysteresis in the order parameter when either of the two control parameters is swept repeatedly across the bistability region.

We report an effect between collective states of *high quantum purity*, which is essential for future information storage. In this aspect, the bistability demonstrated here differs substantially from the familiar case of optical bistability, where the bistable region is created through atomic saturation [92]. Here, in the weak driving limit, where the population of the excited states remains close to zero, the source of nonlinearity is a cavity-assisted population transfer between *ground* states of the atoms, and the stability depends on the intensity of two driving lasers.

Although a repumper laser was already used in the sample preparation protocol (see Sec. 3.7), its optical power control was not implemented, so the setup required development. My task was to create a solution that allows for flexible and consistent power tuning. I replaced the acousto-optic modulator (AOM) previously used to switch the repumper light with one capable of adjustable amplitude modulation. By varying modulation amplitudes and measuring the optical power transmitted through the AOM in the first diffraction order, I calibrated the device. I modified the software control of the experiment, enabling in-situ modulation amplitude adjustment, to set the desired optical power of the repumper or to sweep it in a given range during the experiment.

The chapter is structured as follows. In Sec. 3.2, a model system of competing dynamical optical pumping processes is presented to establish a framework in which to describe our experiments. In Sec. 3.3, the phase diagram is mapped out by solving the mean-field equations of the model and new features of the bistability domain are pointed out. A clear distinction is made with respect to the case of absorptive optical bistability. In Sec. 3.4, the experimental scheme is described and the correspondence to the theoretical model is established. Sec. 3.5 is devoted to measurements on the

long-time behaviour of the system and to the dynamical signatures of the bistability. Both dynamical oscillations and enhanced fluctuations of the order parameter are demonstrated. In Sec. 3.6 it is shown that adiabatic ramp cycles of the control parameters lead to hysteresis, which is supporting evidence of a first-order phase transition in the system [79]. In Sec. 3.7, the interpretation of the observed bistability, namely, that it is based on the competition of two concurrent optical pumping processes, is experimentally verified. Finally, the chapter is concluded in Sec. 3.8.

## 3.2 Model of two-way optical pumping of atoms in the cavity

Let us consider $N$ atoms interacting with a single mode of a linear optical resonator, as represented schematically in Figure 3.1. The cavity mode is driven by a laser with effective amplitude, $\tilde{\eta}$, and angular frequency, $\omega$. This latter is close to the mode resonance, $\omega_{\mathrm{C}}$, such that the detuning $\Delta_{\mathrm{C}} \equiv \omega - \omega_{\mathrm{C}} \lesssim \kappa$, where $\kappa$ is the mode linewidth (HWHM), and red-detuned from the electric dipole transition $|g\rangle \leftrightarrow |e\rangle$, that is $\Delta_{\mathrm{A}} \equiv \omega - \omega_{eg} < 0$. The cavity field couples to the transition $|g\rangle \leftrightarrow |e\rangle$, with coupling constant $\tilde{g}$ (single-photon Rabi frequency). The excited atomic state, $|e\rangle$, decays mostly to $|g\rangle$ with rate $\gamma$ (HWHM), however, a weak decay channel exists to another state, $|f\rangle$, with rate $\Gamma \ll \gamma$. There is a repumper laser illuminating the atoms from the side, which performs optical pumping on the atoms back to the state $|g\rangle$ at a rate $\lambda$. The repumper excites another hyperfine excited state ($F' = 2$), and thus does not form an electromagnetically induced transparency (EIT) type of spectrum in the $\Lambda$ scheme.

The steady-state of this system manifests a non-trivial phase diagram as a function of the control parameters $\tilde{\eta}$ and $\lambda$. Bistability originates from the competition of the two optical pumping processes, where one of them involves a non-linear cavity-assisted population transfer. A single atom in state $|g\rangle$ detunes the cavity mode resonance by an amount $\delta = \tilde{g}^2 \Delta_{\mathrm{A}} / \left(\Delta_{\mathrm{A}}^2 + \gamma^2\right)$, which can be approximated by $\tilde{g}^2 / \Delta_{\mathrm{A}}$

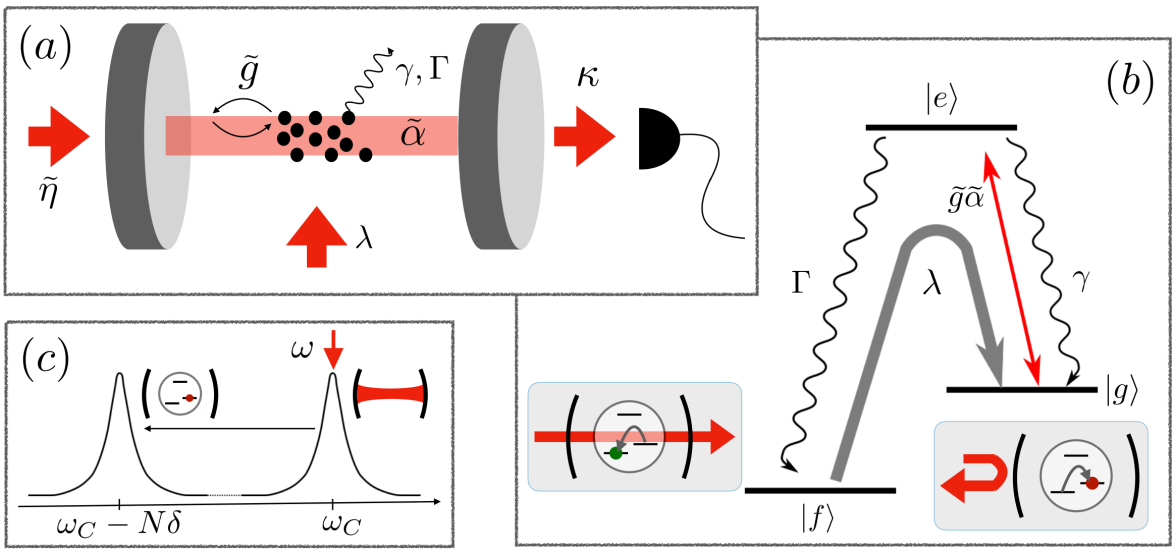


**Figure 3.1:** *(a) The configuration of our CQED scheme. Cold atoms are loaded into a linear cavity and kept in a magnetic quadrupole trap. The cavity is driven with variable effective amplitude, $\tilde{\eta}$, through an incoupling mirror and the transmitted light detected with an avalanche photodiode. The atoms are illuminated from the side by a repump laser of variable power, characterized by the pumping rate, $\lambda$. (b) The relevant part of the atomic level scheme. The transition from the ground state, $|g\rangle$, to the excited state, $|e\rangle$, couples to the cavity mode, resulting in an effective drive amplitude, $\tilde{g}\,\tilde{\alpha}$, where $\tilde{\alpha}$ is the field mode amplitude. The transversely injected repump laser drives the transition from $|f\rangle$ to $|g\rangle$ via other excited states (not indicated). Panels show the cavity transmission accompanying the optical pumping into the states $|f\rangle$ and $|g\rangle$. (c) Atoms in state $|g\rangle$ detune the cavity mode resonance with respect to the laser frequency set on resonance with the empty cavity.*

in the large atomic detuning regime ($|\Delta_\mathrm{A}| \gg \gamma$). This effect is routinely used in our lab (see e.g. Sec. 5.3 and [F1]) to determine the number of atoms in the mode, by probing the cavity with a weak laser at $\omega_\mathrm{L}$ and inverting the term for the measured transmittance, $\left((\omega_\mathrm{L} - (\omega_\mathrm{C} - N\delta)\right)^2/\kappa^2 + 1\big)^{-1}$. For large-enough atom number, the collective dispersive shift of the atom cloud, $N\delta$, can push the mode out of resonance, $|\Delta_\mathrm{C} - N\delta| \gg \kappa$, so that the drive $\tilde{\eta}$ is ineffective in exciting the cavity mode. As there is no field in the cavity, the atoms are not excited from the state $|g\rangle$. This solution, called “transmission blockade”, is a steady state. However, it becomes unstable for very large drive strength $\tilde{\eta}$. The Lorentzian cutoff does not eliminate perfectly the transmission. The blockade may break down in a runaway process: for increased cavity drive amplitude, the tiny amount of light infiltrating the cavity excites atoms

to $|e\rangle$, which, in turn, results in a reduction of the collective resonance shift and in even more light entering the cavity. This positive feedback amounts to a run-away optical pumping toward the state $|f\rangle$. The extent to which the atoms accumulate in state $|f\rangle$ depends on the repump rate, $\lambda$. For weak $\lambda$, they accumulate; for strong $\lambda$, the atoms are pumped back to $|g\rangle$ and restore the blockaded regime. In between, there is a bistability domain where the two steady states can coexist in the form of a statistical mixture.

The competition between the two optical pumping processes can be described by the semiclassical mean-field model discussed in Ch. 1 [93]. The *scaled* mean-field equations of motion (1.9) are extended with the relative population in the state $|f\rangle$, $n_f$, the decay rate from $|e\rangle$ to $|f\rangle$, $\Gamma$ and the repump rate, $\lambda$. The set of equations with the additional terms (using the scaled variables, noted without the tilde) read

$$\begin{aligned}
\dot{\alpha} &= (i\Delta_{\mathrm{C}} - \kappa)\alpha + gm + \eta\,, \\
\dot{m} &= (i\Delta_{\mathrm{A}} - \gamma - \Gamma)m + g\,(n_e - n_g)\,\alpha\,, \\
\dot{n}_e &= -g\,(\alpha^* m + m^* \alpha) - 2(\gamma + \Gamma)n_e\,, \\
\dot{n}_g &= g\,(\alpha^* m + m^* \alpha) + 2\gamma n_e + \lambda n_f\,, \\
\dot{n}_f &= 2\Gamma n_e - \lambda n_f\,.
\end{aligned} \tag{3.6}$$

In the rest of this chapter, the case of resonant driving of the empty cavity, $\Delta_{\mathrm{C}} = 0$ is considered.

Although the model is heavily simplified, it is sufficient to capture the main features of the steady-state phase diagram. In particular, the reason we consider the repumper acting only on the populations of states $|g\rangle$ and $|f\rangle$, without creating coherence between them, will be explained in Sec. 3.4.

## 3.3 Steady-state phase diagram

The driven-dissipative system defined by Eqs. (3.6) evolves towards a steady state that can be calculated by setting the temporal derivatives to zero, and solving the inhomogeneous nonlinear system of equations. Fig. 3.2 presents a colour map of the cavity transmittance in the steady state as a function of the two drive strengths, the scaled cavity drive amplitude $\eta$ and repump rate $\lambda$, for $N = 10^4$. The transmittance is the transmitted intensity normalized to that of the empty resonator with exactly the same drive $\eta, \omega$. One can clearly observe the blockaded regime for small $\eta$, where the cavity field mode is not populated (dark blue region) as well as a 'bright' phase with high transmission (yellow region). These phases are separated by a bistable domain (white stripe), where the system has two stable steady states. These solutions are plotted in Fig. 3.3 for cross-sections of fixed $\eta$ and $\lambda$ values, indicated by dotted and dashed lines in Fig. 3.2, respectively.

The transmittance exhibits an S-shaped curve as a function of the cavity drive, that is familiar from saturation-induced optical bistability (cf. Fig. 3.3(b) and (c)). There are two stable steady states and one unstable solution. In the present case of a three-level $\Lambda$ scheme, a similar multivalued domain occurs if the repumper power is varied, as shown in panel (a). This highlights the crucial role of the repumper and the third level $|f\rangle$ in the system. The distinctive feature with respect to the well-known case of optical bistability can be revealed by investigating the populations in the three atomic levels in the steady-state solutions, shown in the bottom row of panels in Figs. 3.3(d-f). In the transmission-blockaded phase, the atoms are dominantly in the state $|g\rangle$, i.e. $n_g \gg n_f, n_e$ independently of the repumper and the cavity pump strength. When the blockade is broken down and there is a finite transmittance approaching unity, the populations strongly depend on the repumping rate.

In the low $\lambda$ limit ($\lambda \ll \Gamma$), the cavity photons optically pump the atoms to the other ground state $|f\rangle$, resulting in $n_f \gg n_g, n_e$ (see the bottom-right inset scheme in the phase diagram in Fig. 3.2). This limit of bistability, represented by Fig. 3.3(e), features a bistable switching between steady states, corresponding to collective elec-

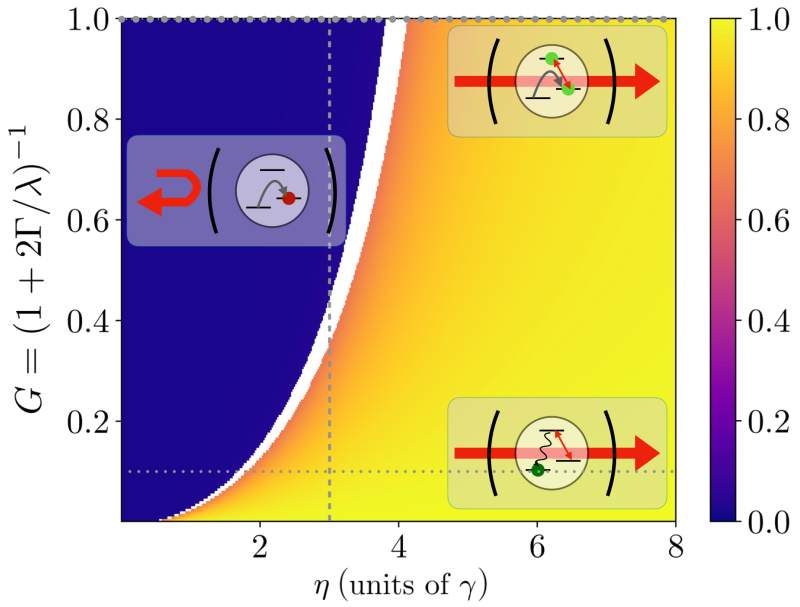


**Figure 3.2:** *Phase diagram of the transmission blockade breakdown in the steady state for $N = 10^4$ atoms. The colour map shows the cavity transmittance referenced to the resonant empty cavity transmission as a function of the scaled cavity drive amplitude, $\eta$, and repumping rate, $\lambda$. The latter quantity is rescaled with a monotonically increasing function, $G \equiv (1 + 2\Gamma/\lambda)^{-1}$, which tends to $G = 1$ for $\lambda \to \infty$. The white stripe in the middle corresponds to the domain where the system of equations admits multiple stable solutions. There are distinct phases to the left and right of this boundary, which are the blockaded and the bright states of the cavity field, respectively.*

tronic ground states, $|g\rangle$ and $|f\rangle$ with high purity, and the cavity-transmitted photocurrent enables a direct monitoring of which ground state the atoms are in.

As a reference, the case of classical bistability is displayed [94–96], which is reproduced in the limit of $\lambda \to \infty$, $G \equiv (1 + 2\Gamma/\lambda)^{-1} = 1$, when the strong repumper confines the atomic state to the two-level manifold spanned by $|e\rangle$ and $|g\rangle$ (corresponding to the top-right inset scheme in Fig. 3.2)). Fig. 3.3(f) shows that the bright cavity phase is connected to a full mixture of the atomic state $n_e \approx n_g$, while $n_f \approx 0$. This means that cavity photons saturate the atoms in the two-level manifold, while state $|f\rangle$ is effectively eliminated from the dynamics by the strong repumper. This model thus reveals that the control parameter $\lambda$ bridges the well-known saturable absorber optical bistability and the much more recent paradigm of first-order dissipative phase transitions, that has been shown to be represented by the photon-blockade-breakdown bistability.

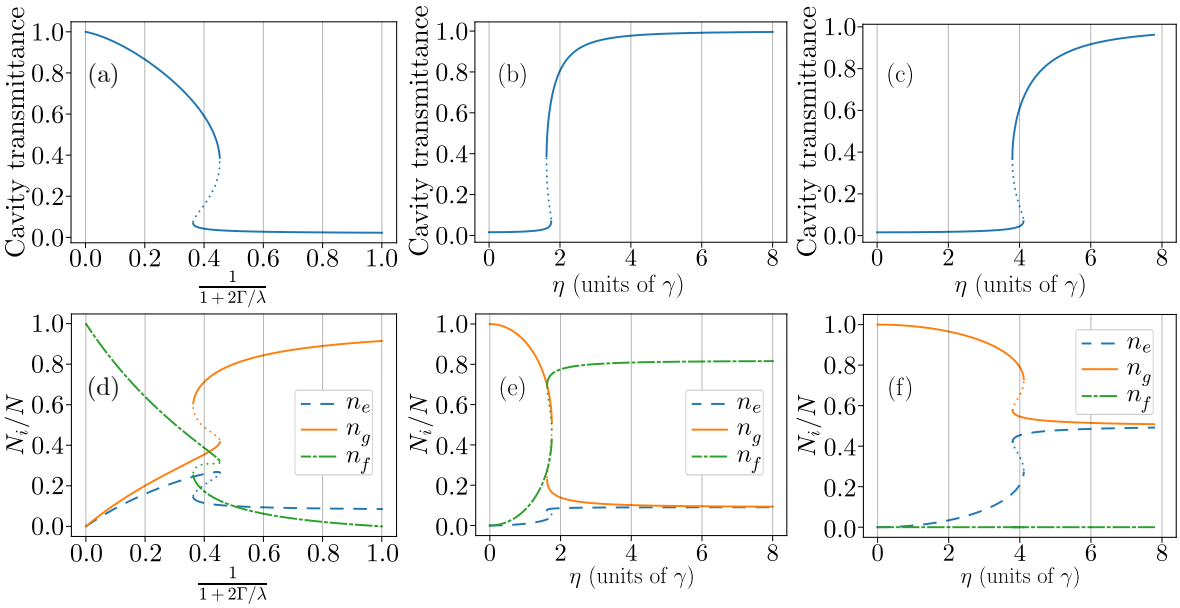


**Figure 3.3:** *Cavity transmittance and atomic populations as a function of pumping rates. Transmission is first considered with respect to varying repump rates, with the cavity drive fixed at $\eta = 3\gamma$, (a). Secondly, transmission is considered as a function of the cavity drive amplitude for fixed repumping rates $G = 0.1$, (b), and $G = 1$, (c). Similarly, the relative steady-state populations, $n_f$ (dash-dotted green), $n_e$ (dashed blue) and $n_g$ (solid orange) are plotted with respect to the same pumping rates, (d-f). All the plots show a crossing of the bistability domain, represented by the white stripe, in Fig. 3.2 along a vertical, (a and d), and horizontal (panels (b), (c), (e) and (f)) axis. Where the control parameters, $\eta$ and $\lambda$, give rise to multiple solutions, the dotted lines correspond to unstable solutions, the rest to stable steady states.*

In the following, experimental results are presented from measurements on a CQED system that is more involved than the above-discussed abstract model. However, it will be shown that the main features of the interaction are properly captured by the model, and the phase diagram presented in Fig. 3.2 underlies the actual CQED system of the experiment.

## 3.4 Experiment

Approximately $N \sim 10^5$ atoms were loaded into the mode volume of the optical cavity, and maintained in the magnetic trap, according to the protocol described in Sec. 2.4. A single mode of the resonator was resonantly driven, $\Delta_C = 0$, with the

science laser tuned below the $F = 2 \leftrightarrow 3$ atomic resonance by $\Delta_{\mathrm{A}} = -2\pi \cdot 29$ MHz. Along with a circularly polarized drive field, $\sigma^+$, the single-atom frequency shift was $\delta \approx 2\pi \cdot 3$ kHz, such that $N \approx 10^4$ relevant atoms could shift the mode by more than $10\kappa$ from resonance.

A mapping between the abstract model of Eq. (3.6) and the actual level scheme of $^{87}$Rb is presented in Fig. 3.4, together with the given configuration of laser drives. The state $|g\rangle$ corresponds to the hyperfine ground state $(F, m_F) = (2, 2)$ in $5^2\mathrm{S}_{1/2}$, whereas the excited state $|e\rangle$ is realized by $(F, m_F) = (3, 3)$ in $5^2\mathrm{P}_{3/2}$. This is a closed-cycle transition within the $\mathrm{D}_2$ line for $\sigma^+$ circular polarization. As the atoms are in a magnetic quadrupole trap, the magnetic field defining the local quantization axis varies in space. In the plane of the cavity mode, the magnetic field lies in the same plane, pointing radially outward from the trap centre which coincides with the centre of the cavity (Fig. 3.5). Therefore, the magnetic field is oriented, to a good approximation, parallel to the cavity axis within the mode. However, in the two halves of the mode volume, being on the two opposite sides of the mode centre, the magnetic field is pointing in opposite directions. Therefore, the circularly polarized cavity drive field is effectively $\sigma^+$ in one half, and $\sigma^-$ in the other half of the mode volume with respect to the local quantization axis. The atomic motion in the magnetic trap averages these two distinct effects.

The $\sigma^-$ polarized field generates transitions from $|g\rangle$ to $(F, m_F) = (2, 1)$ in $5^2\mathrm{P}_{3/2}$, which has a much smaller Clebsch-Gordan coefficient than the $\sigma^+$ transition (ratio $1/15$). Nevertheless, excitation to the $(F, m_F) = (2, 1)$ implies that the atoms can decay into $(F, m_F) = (1, 1)$, which is the state $|f\rangle$. The decay can also lead to the other hyperfine state $(F, m_F) = (1, 0)$. However, this state can be incorporated into $|f\rangle$. The coupling between the ground-state manifolds $F = 1$ and $F = 2$ includes a spontaneous emission process in both directions, therefore only the populations, not coherences between the states $|f\rangle$ and $|g\rangle$, $|e\rangle$ play a role. The repumper resonantly drives the transition from the $(F, m_F) = (1, 1)$ ground state to the $(F, m_F) = (2, 2)$ excited state with $\sigma^+$ polarized light, which amounts to an optical pumping into the state $|g\rangle$. This is considered as a population pumping with rate $\lambda$ in equation (3.6).

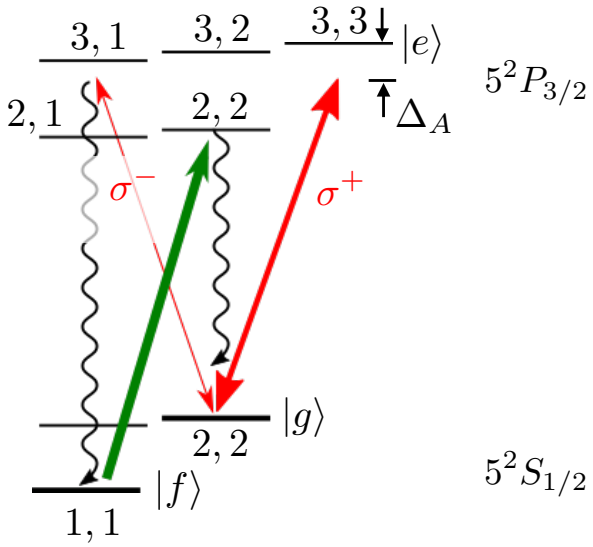


**Figure 3.4:** *The $^{87}$Rb levels behind the simplified model in Fig. 3.1. Red arrows represent cavity field excitations and the green arrow the repumper. Other states in the hyperfine manifold with smaller magnetic quantum numbers are not shown.*

The other simplification in the semiclassical model is that the state $|f\rangle$ is populated directly from the state $|e\rangle$, rather than introducing additional variables to include the state $(F, m_F) = (2, 1)$. The population in this latter is proportional to that of $|e\rangle$, since both of them are excited by the cavity field from the state $|g\rangle$. Therefore, the crucial dependence on the cavity field intensity and the population in $|g\rangle$ is captured by the model with a phenomenological rate, $\Gamma$, determined previously as $\Gamma = 0.93 \cdot 10^{-3}\gamma$, by fitting the numerical simulation to the observed transition dynamics [59].

The mean-field model, appropriately accounting for the cavity-assisted optical pumping processes, does not include the atom loss from the trap. The total atom number, $N$, in Eqs. (3.6) is not a conserved quantity. The loss can occur due to recoil heating, background gas collisions, etc. There are other processes which follow from the dynamics: when the atom is in state $|f\rangle$, the magnetic trap potential vanishes for the $(F, m_F) = (1, 0)$ and is repulsive for the $(1, 1)$ states. Because of the atom loss, the system ultimately evolves into the resonant empty-cavity transmission on a slow timescale of a few 100 ms (cf. measurement results below). Note also that atoms in the magnetic trap but outside the mode can enter the mode volume. However, these atoms adapt their internal state on a timescale of ms to the actual global phase of the

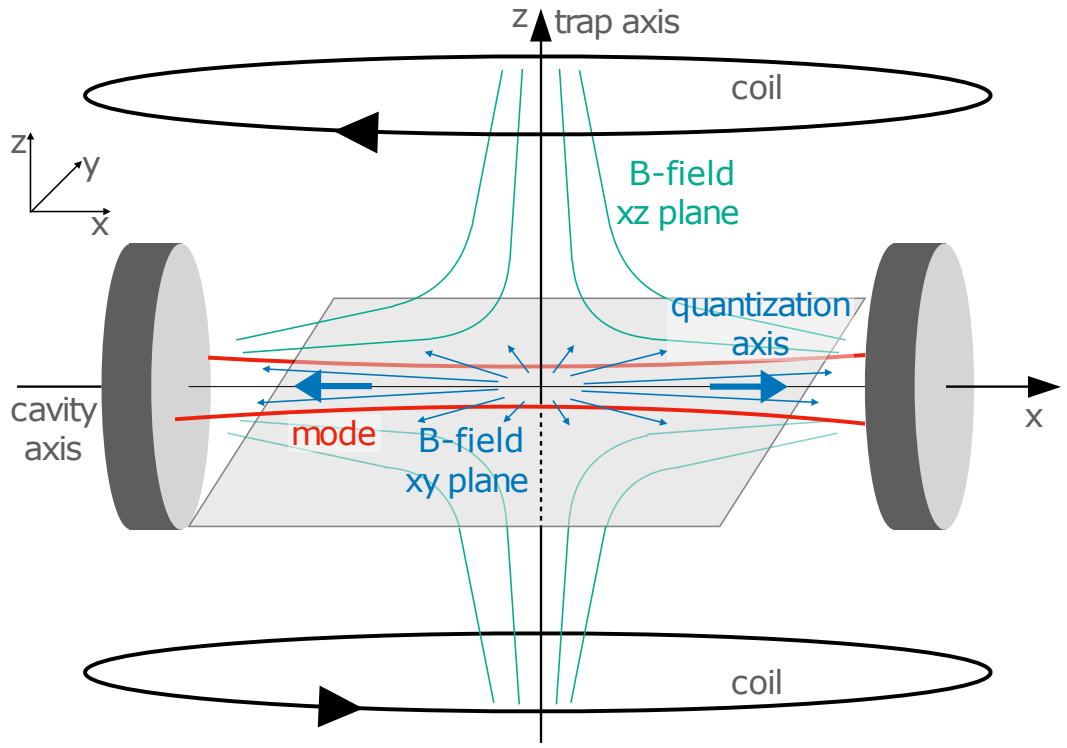


**Figure 3.5:** *Magnetic field lines and orientation with respect to the cavity axis (red lines representing the cavity mode waist in the x-y plane). In the x-z plane, the quadrupole trap creates field lines that bend away from the origin and that are cylindrically symmetric around the z axis (green lines). Perpendicular to this, within the x-y plane of the cavity axis (grey), the magnetic field lines (thin blue arrows) point radially outward. The quantization axis (thick blue arrows), within the cavity mode, is then parallel to the cavity axis but with opposite orientation in the two halves of the mode.*

system determined by the control parameters. Therefore, this reloading process can be treated together with the losses by embedding them into an effective loss.

## 3.5 Driven-dissipative phase transitions

The end of the atom transport into the cavity mode defines the time $t = 0$. The cavity drive was switched on at $t = 3$ ms at the chosen power level. The cavity transmission was recorded by an avalanche photodiode until $t = 5$ s. In all the measurements, the atoms were initially in the ground state, $|g\rangle \leftrightarrow (F, m_F) = (2, 2)$. Therefore, the transmission at the beginning of the interaction, with $N \sim 10^5$ atoms in state $|g\rangle$, was always suppressed by the dispersive shift of the mode with respect to the fixed

drive frequency by more than ten times the linewidth. Depending on the strength of the cavity drive and that of the repumper, this state could be the stable phase or an unstable one, according to the phase diagram in Fig. 3.2.

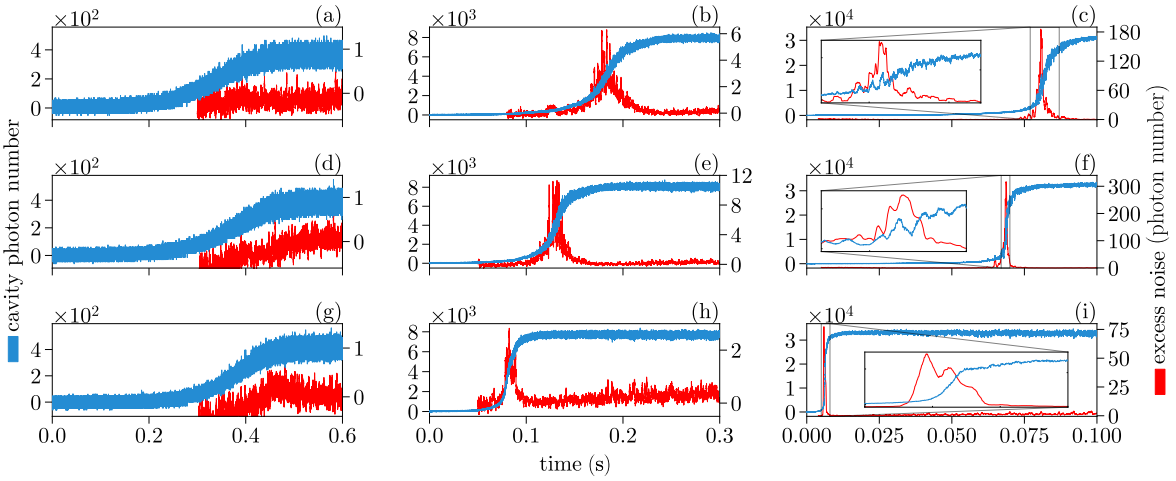


**Figure 3.6:** *The time evolution of the system with respect to varying control parameters, as monitored by the cavity transmission (blue lines, left scale) and the excess noise (red lines, right scales). The cavity drive amplitude increases from left to right ($\tilde{\eta}/\gamma = = 25, 117, 236$) and the repumping rate decreases from top to bottom ($\lambda/\gamma = 5.9 \cdot \cdot 10^{-3}, 0.85 \cdot 10^{-3}, 0.27 \cdot 10^{-3}$), such that $G = 0.76$, $0.31$ and $0.13$, respectively. The dynamics of the transition between the blockaded phase (close to zero transmission) and the transparent steady-state (transmittance reaches the maximum corresponding to a driven empty resonator) illustrate different domains of stability in the selected time windows. The transition changes from a smooth one induced by inevitable atom loss from the trap (weak cavity drive, left column of panels) to a sharp runaway dynamics for strong drive (panel (i)), and oscillatory behaviour for stronger repump (panel (f)). The excess noise (in cavity photon number) accompanying the transitions is shown by the red curves. When the control parameters are in the bistability domain, the single-mode cavity field manifests significantly enhanced fluctuations during the transition between the steady-states.*

Figure 3.6 shows the cavity transmission as a function of time for $3 \times 3$ different pairs of fixed values of the control parameters $\tilde{\eta}, \lambda$. The cavity drive strength $\tilde{\eta}$ increases from left to right, whereas the rescaled repumping rate $G$ increases from bottom to top. The left column represents a weak cavity drive compared to the effect of the repumper. According to the phase diagram in Fig. 3.2, the stable phase is the blockaded one with atoms in $|g\rangle$, which is the initially prepared state of the system. In this case, only atom loss can lead to the transparent cavity state. Indeed, the left

column shows that the transition is independent of the repumper strength and takes place on a long timescale of about 350 ms. This timescale can be attributed to the situation that even atoms in state $|g\rangle$ are gradually lost from the trap, due to the above described mechanisms not contained in our idealized theoretical model of Sec. 3.2. On increasing the cavity drive intensity (middle column of panels), an earlier and faster emptying of the trap can be observed. This indicates that the steady state is still the transmission blockade, and the cavity drive merely increases the population in the states $|e\rangle$ and $|f\rangle$, thereby speeding up the atom loss.

Qualitatively different behaviour of the transition is depicted in the right column of panels, where the cavity drive is strongest. For the bottom right panel, (i), the repumper drive intensity is so weak that the stable phase is the transparent resonator with atoms in $|f\rangle$. However, the system, initially, is prepared in the other, transmission blockaded phase with all atoms in $|g\rangle$. Before considerable atom loss can take place, the system undergoes a non-linear runaway process to transition into the stable phase. This is clearly the case in (i), and traces of this dynamics can be observed in (h). So the bottom row shows that the transition varies from an atom-loss dominated smooth transition (bottom left panel) to a phase-transition-like switch on increasing the intensity of the cavity drive. This effect has been thoroughly analysed in the paper preceding and motivating this extended study [59].

The key new observation is represented mostly by panels Fig. 3.6(f) and (c). Rather than a fast, monotonic switching to the stable phase, as in panel (i), stronger repumping leads to an oscillatory transition in (f) and, somewhat less clearly, in (c). The strong dynamical oscillations are indications of the competition of the opposing optical pumping processes. They appear only in a limited range of the control parameters for which the system is in the bistability region of the phase diagram. However, when monitoring the transmitted intensity, the oscillatory effect due to bistability is limited by the loss of atoms from the trap. One can unravel the dynamical signatures of the transition which are beyond the effects of the atom loss by analysing the intensity fluctuations. An alternative method, presented in the next section, is to vary the system parameters on a timescale shorter than that of the loss.

The phase transition is confirmed by the increased intensity of fluctuations in the detected transmitted signal. In the steady states, the atoms are either in the $|g\rangle$ or in the $|f\rangle$ ground state, with the single-mode cavity field being in either the $|0\rangle$ vacuum state or an $|\alpha \neq 0\rangle$ coherent state, respectively. In a more general context, these states of the mode can be considered as thermal states of zero temperature [97]. During the transition, however, the atoms exist in a statistical mixture of the blockading $|g\rangle$ ground state and the $|e\rangle$ excited state, leading to the broadening of the Wigner function for the cavity mode. Assuming the state remains Gaussian and positive definite, this broadened state can be described as a displaced thermal (chaotic) state represented by the $P$ function, $P_{\mathrm{th,disp}}(\beta) = \frac{1}{\pi n_{\mathrm{th}}} e^{-|\beta-\tilde{\alpha}|^2/n_{\mathrm{th}}}$, with mean field denoted by the complex amplitude $\tilde{\alpha}$, and the width of the distribution characterized by the thermal photon number $n_{\mathrm{th}}$. This parameter is zero for coherent states, and greater than 0 for thermal states of non-zero temperature, serving as a measure of the excess noise of the state with respect to the Poissonian noise. This excess noise, corresponding to fluctuations of the mean-field amplitude, $\alpha$, is beyond the scope of the mean-field model. It can be inferred from the recorded intensity noise following the procedure described in Ref. [59].

The atom-loss dominated transition to the bright phase (left column of panels) does not exhibit excess noise during the transition (note that the initial fluctuations including even negative photon numbers in panel Fig. 3.6(a), (d), and (g) indicate the finite accuracy of the method close to zero mean value of the field, i.e. uncertainty is below 0.5 photon). There is some excess noise generated during the transition with increased $\tilde{\eta}$ (middle column), while significantly enhanced intensity fluctuations accompany the transition for strong cavity drive (right column). An equivalent of 20 and 100 thermal photons characterize the width of the photon number distribution in the cavity mode during the limited time period when the system is in the transmission blockade breakdown and the bistability region, Figs. 3.6(i) and (f), respectively. This is comparable, but in addition to the Poissonian noise, which is approximately $100$ photons at the observed mean photon number ($\sim 10^4$).

The enhancement of fluctuations depends systematically on the control parame-

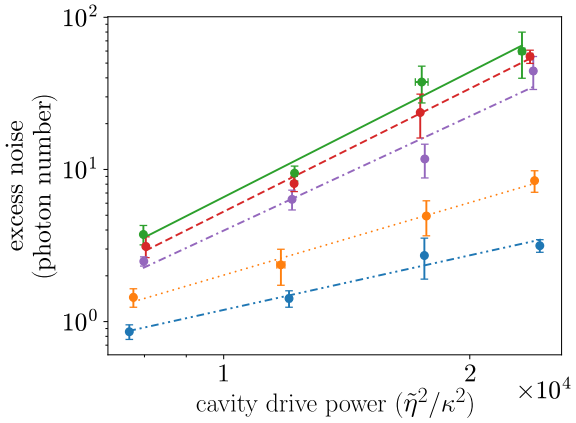


**Figure 3.7:** *The magnitude of the excess noise (in thermal cavity photon number) with respect to the cavity drive power (empty cavity photon number). Different colours and line styles correspond to different repumper strengths,* $G = 0.127$ *(dash-double-dotted blue),* $0.144$ *(dotted orange),* $0.542$ *(solid green),* $0.632$ *(dashed red) and* $0.708$ *(dash-dotted purple). Each point represents the average of ten measurements. The linear fits in the log-log scale reveal power laws with exponents* $1.19 \pm 0.15$*,* $1.58 \pm 0.11$*,* $2.73 \pm 0.27$*,* $2.68 \pm 0.11$ *and* $2.49 \pm 0.36$*, respectively.*

ters. For example, consider the rows of Fig. 3.6 in which only the cavity drive varies. Expressing this enhancement in terms of a thermal photon number, it shows a power law dependence on the cavity drive as seen on the log-log plot in Fig. 3.7 where the drive is also expressed as the photon number the drive would generate in an empty cavity. The exponent varies with the repumper strength (numerical values given in the figure caption). A deeper theoretical interpretation of this experimental observation requires the description of higher-order quantum correlations in the atom-light interaction, which is beyond the scope of the mean-field approximation of the Heisenberg–Langevin equations.

## 3.6 Hysteresis

The total atom number in the trap, $N$, evolves in time due to loss processes not included in the theoretical model. As such, these changes are not reflected in the phase diagram of Fig. 3.2. As atoms are being lost, the bistability domain of the diagram shifts towards smaller cavity drive strengths, i.e. the transmission-blockaded

phase gradually shrinks. Nevertheless, the atom loss process is slow enough that the multistability of the system can be demonstrated for quickly varying probe light, in the form of hysteresis [79].

To this end, the control parameters were swept repeatedly across the bistability domain. The intensities were varied, ramping the drive voltage of the AOM up and down linearly. For the cavity probe laser, $\tilde{\eta}$, the ramp times were 30 ms up, and 10 ms down, while for the repumper, the corresponding values were 15 and 5 ms, respectively. Fig. 3.8 presents the cavity transmission for ramping, (a), the cavity drive and, (b), the repumper intensity five times, while the other control parameter was kept fixed. An individual trajectory of the order parameter is depicted, since the bistability must be manifested at this level of single runs. With the current parameters, we experienced little variation between runs, so the presented sample was typical. The atoms were initially prepared in state $|g\rangle$, so the cavity transmission was initially suppressed. The first ramping cycle of the cavity drive did not move the system out of this phase (cf. Fig. 3.8(a)) because even if this phase becomes unstable for high cavity drive, when the bistability domain is crossed during the ramp, the transition from such a steady state takes place after a long waiting time. The lifetime of this metastable phase is random, but, on average, increases with the number of atoms in the cavity. At this first ramp, it happened to exceed the sweep period. This scenario was more likely during the first cycle than in subsequent ones, as no atoms had been lost yet. During the second ramp-up (orange curve), the transition to the bright phase, atoms in $|f\rangle$, did occur. Hence, during the ramp-down, there was a higher cavity transmission at the same drive strength. This is convincing evidence of bistability. It was only at the end of the ramp down period that the repumper transferred the atoms back to state $|g\rangle$, reinstating the blockaded phase. At the beginning of the next ramp up period (green), this was still the ongoing direction of optical pumping until the cavity drive started to dominate. Accordingly, the corresponding transmission curve (green) is slightly below than the preceding ramp-down curve (orange). This ramp cycle, with the same features, could be observed three more times before the atoms were lost from the cavity. We re-emphasize that the hysteresis window shrinks

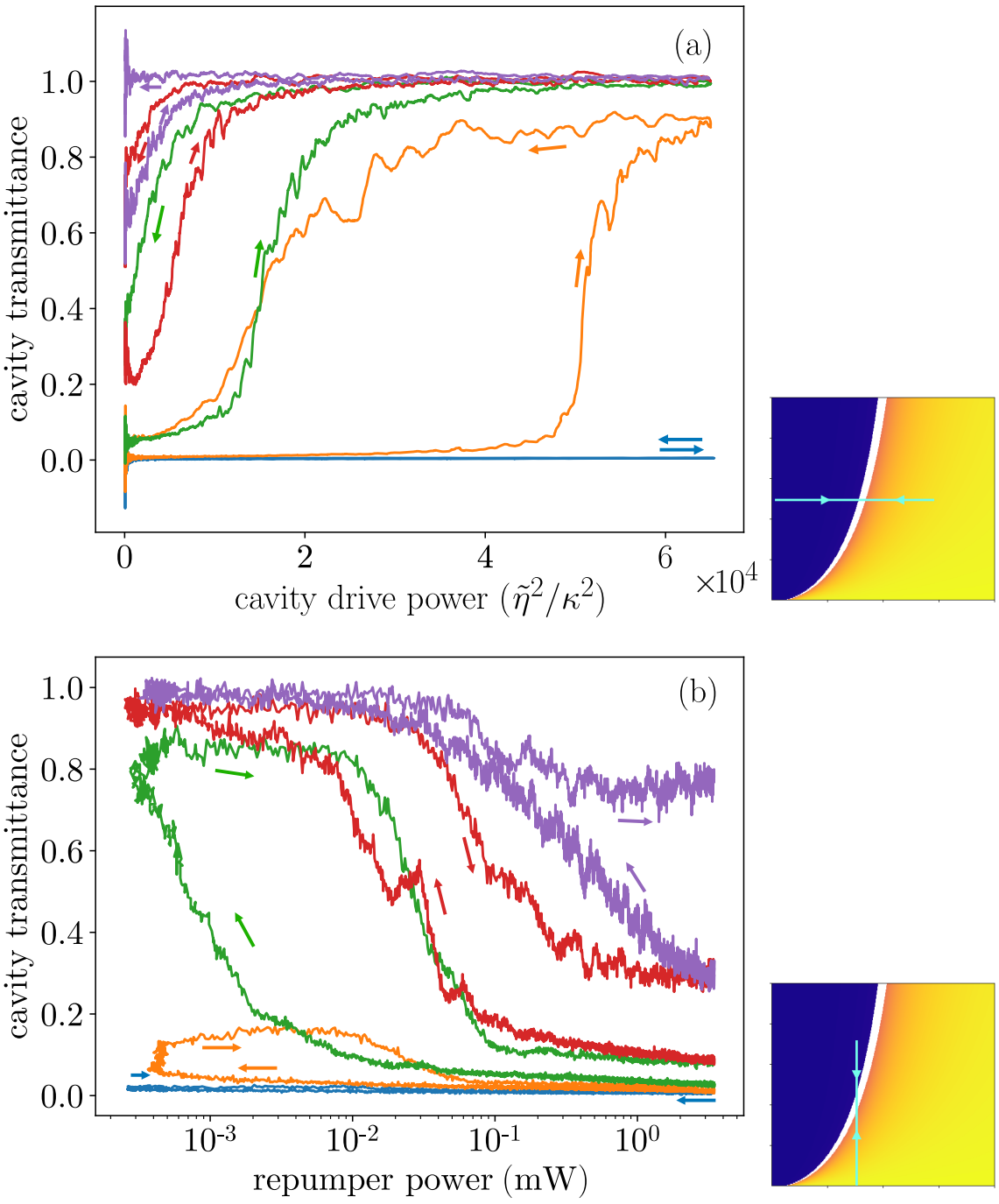


**Figure 3.8:** *Hysteresis in the cavity transmittance when the cavity drive power, (a), and the repump power, (b), sweep across the bistability domain back and forth five times. The corresponding sweep axis in the phase diagram is shown in the small panels to the right. The temporal order of the ramps is indicated by the blue, orange, green, red and purple lines, respectively, and the ramp direction by the arrows. For (b), a* $\log_{10}$ *scale is used.*

for consecutive cycles due to the decreasing number of atoms.

The hysteresis was also confirmed at fixed cavity drive by varying the repumper as a control parameter. Considering the transition across the bistability domain, the repumper powers are widely varied, therefore, a logarithmic scale is used on the horizontal axis. In Fig. 3.8(b) the curve starts at the large repumper limit, where the initial state of atoms in $|g\rangle$ corresponds to the stable phase. Within a sweep cycle, the value of the repumper power was below the bistability domain for short times only, so the transition to the states $|f\rangle$ did not happen in the first cycle (blue) but only in the second one (orange). In this cycle, a partial population transfer to the states $|f\rangle$ was accomplished within the ramp-down time and a part of the atoms remained in the blockading state $|g\rangle$. The cavity transmission increased noticeably, but to a value well below the empty cavity reference. At subsequent cycles, the atom number was smaller due to loss, and a full transfer from the state $|g\rangle$ to $|f\rangle$ has been achieved during the period where the repumper intensity was decreased below the bistability domain. At these smaller atom numbers, on the other hand, the mode frequency shift did not reach the level necessary to suppress the transmission, meaning, the red and purple curves do not go down to zero for strong repumper on the right side of the plot. Nevertheless, hysteresis was clearly observed in these cycles, implying the presence of bistability.

## 3.7 The role of the repumper

An additional measurement was performed in order to outline the role of the repumper and to detect the atomic state in the bright phase. The repumper was pulsed between zero and a large value, $G = 0.44$, with a period of 5 ms (on/off ratio 1). The time evolution of the cavity transmission is plotted in Fig. 3.9, where the blue curve represents the evolution of the system without repumping, while green gives the transmission with constant repumping, for the same value of $G$. These configurations correspond qualitatively to the (i) and (c) panels of Fig. 3.6, respectively. In the prior case, the system with atoms in $|g\rangle$ is prepared in a phase which is unstable at

finite cavity drive and without repumper. Therefore, the system switches to the stable phase in a runaway process at a random time. With the repumper on, the blockaded phase is stabilized to some extent, and the runaway transition is delayed until fewer atoms are present, due to inevitable atom loss from the trap. The observed curve for the pulsed repumper demonstrates that the atoms can be transferred back to the state $|g\rangle$ by means of the repumper. The blockade was reinstated repeatedly, following the pulse sequence exactly. This shows that when the cavity transmission blockade was broken down, the atoms were shelved in the state $|f\rangle$, from where they could be pumped back to the blockading state $|g\rangle$. This proves, on the one hand, that the cavity transmissivity is not due to an atomic saturation effect on the $|g\rangle \leftrightarrow |e\rangle$ transition. On the other hand, since the repumper reinstated the blockade at the same level as it was a period of 5 ms earlier, there is no significant light-induced loss of atoms from the trap during the timescale 40 ms of the observed transition. There is of course loss on the longer time scale, as can be seen, for example, in Fig. 3.6(g) corresponding to weak drive and repump, on a time scale of several hundreds of milliseconds.

In addition, this measurement served for the calibration of the model parameter, $\lambda$, characterising the AOM-controlled repumper intensity. When there is a sudden increase of the cavity transmittance (repumper is off), the magnitude of its change gives information on the depletion of the population in $|g\rangle$. One can safely assume that these atoms are accumulated in the state $|f\rangle$. On switching on the repumper, from the initial slope of the transmittance drop, it is possible to deduce the rate of change in the population of $|f\rangle$. It is given by $-\lambda n_f$, according to the last term in Eqs. (3.6), from which the rate $\lambda$ can be obtained.

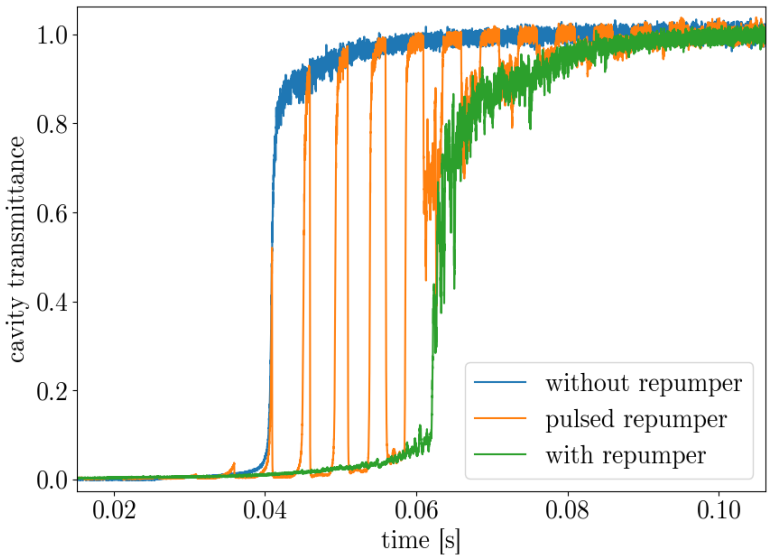


**Figure 3.9:** *The time evolution of the cavity transmission without repumping (blue), with repumping (green) and with pulsed repumping (orange). When the repumper is switched off, the system starts to evolve in a runaway process toward the bright phase at a given time near $t = 0.04$s. With the repumper on, however, the system undergoes the transmission blockade breakdown at a later time than without it. As the repumper is strong in this case, the transition to the high transmittance phase, with atoms in state $|f\rangle$, takes place only when the atom number is significantly reduced due to other loss processes. With pulsed repumping, the transition occurs every 5 ms, because the repumper brings the atoms back from state $|f\rangle$ to state $|g\rangle$ (the blockaded phase): switching between the two hyperfine ground states.*

## 3.8 Conclusion

I have experimentally demonstrated bistability in a cold atom-cavity QED system, where the steady states correspond, dominantly, to hyperfine ground states. Having explored the runaway pumping processes involved, I have described the phenomenon in terms of a driven-dissipative phase transition, with two optical driving intensities as control parameters and cavity transmission as the order parameter of the system. Crucially, by exploring different combinations of optical pump intensities, I have shown that the steady state of the system depends on the history. This observed hysteresis, in both control parameters, not only confirms the bistability but that the transition is a first-order effect. In fact, high pumping intensity in one of the control beams recovers the original, widely known, optical bistability, such that it is

included as a special case in the system presented here.

Considering future directions, it is important to note that the system size is characterised by the cooperativity, i.e. the collective coupling strength between the atomic cloud and the cavity mode. In our system, the cooperativity, $\mathcal{C}$, was about 100 which is comparable with the one reached in the circuit QED systems with single artificial atoms [87]. However, in this $\Lambda$ atom scheme, the cooperativity can be increased by the number of atoms, so one can better approach the thermodynamic limit. One possible solution is to use Bose condensed gases, for which the steady-states would be entirely quantum in all degrees of freedom. As the cavity transmittance is associated with hyperfine states, which can be coherently manipulated with microwave radiation, the system shows analogy with single-atom based quantum switches [98] and quantum birefringence systems [99]. Within many-body systems, the observed effect suggests a pathway for bringing microscopic quantum effects to a mesoscopic system size.

# Chapter 4

# Quantum bistability in the hyperfine ground state of atoms

## 4.1 Introduction

First-order phase transitions are ubiquitous in nature, however, this concept is ambiguous and often contested regarding open quantum systems. The study presented in this chapter, while offering a paradigmatic example that clarifies the essential concepts, shows that atoms in an optical cavity can exhibit a first-order dissipative phase transition, where the stable co-existing phases are collective quantum states with high quantum purity. These states correspond to atomic hyperfine ground states and coherent states of electromagnetic field modes. The scheme takes advantage of the collective enhancement of the coupling between the atoms and the cavity field. In this way, a readily implementable experimental scheme is proposed to study the dissipative phase transition phenomenology in the quantum limit, enabling, specifically, a finite-size scaling toward the thermodynamic limit.

First-order dissipative quantum phase transitions (DQPTs) [100, 101] feature the following defining properties: (i) the quantum system has multiple stable steady-states in a finite interval of a given control parameter, these states are (ii) macroscopically distinguishable by an order parameter, and (iii) are approximately pure

quantum states. When the control parameteris swept across the critical domain, the steady state depends on the history of the system, and hysteresis is manifested in the order parameter. While many classical systems show the multistability properties (i) and (ii), quantum counterparts that also fulfill condition (iii), have only recently been identified in various systems. A first-order DQPT was predicted theoretically for the clustering of Rydberg atoms [102–104], although the experimental feasibility has been contested [105–108]. Optical lattices with engineered losses [109, 110], ultracold-atom cavity QED systems [111], nonlinear photonic or polaritonic modes [56, 79], exciton-polariton condensates [112], and circuit QED systems [87, 113, 114] have also been shown to feature first-order dissipative phase transitions.

Optical bistability [80, 115–118] is a paradigmatic example of a first-order phase transition in cavity QED. In its common form [116] it satisfies conditions (i) and (ii), but not (iii). Depending on the state of atoms in a laser-driven optical resonator, its transmissivity can be switched between high and low values at a fixed drive intensity. The nonlinearity arises from the saturation effect of two-level atoms. However, the bright phase, involving saturated atoms, is a high-entropy mixed state, violating condition (iii) above.

All the three properties can be identified in the case of the recently revealed photon-blockade-breakdown (PBB) phase transition [73, 86, 119]. The experimental configuration is very similar, but only a single two-level atom is coupled to the mode with very large dipole coupling. This can be achieved in superconducting circuit QED systems in the microwave frequency regime, where the signatures of a closely related bistability effect have been observed with three-level atoms [87].

Similarly to PBB, the thermodynamic limit, where a bimodal phase-space distribution composed of two metastable states becomes true bistability between macroscopically distinct *phases*, is reached by increasing the cooperativity. However, in contrast to PBB, this can be achieved by increasing the atom number rather than the single-atom coupling constant, the latter being impossible to vary in the optical domain.

## 4.2 Mean-field model

The proposed scheme is the extension of the experiment discussed in the previous chapter, cf. also [120] for a related scenario: in this case, two cavity modes are used instead of just one. The modes interact with an ensemble of atoms modelled by a four-level scheme (see Fig. 4.1). The two cavity modes must have a spectral separation close to the atomic hyperfine splitting, which is not available actually in our experimental setup (the FSR is larger than the hyperfine splitting, see Table 2.2 and Fig. 2.2, respectively). However, the theoretical study is motivated by the striking feature of the present scheme within the above listed zoo of first-order DQPTs, namely the high quantum purity of the metastable steady states, whereas *in the thermodynamic limit, the bistable phases become perfectly pure*. The two modes are either in vacuum or in a high-intensity coherent state, meanwhile the atoms are in one of their hyperfine ground states. The essential features and the phase diagram can be captured by the mean-field theory introduced in Ch. 1 with the inclusion of the additional cavity mode and atomic states. The atoms collectively couple to the cavity modes, which mediate an infinite-range interaction. As a result, the mean field theory provides an accurate description of our system. While in the case of short-range interactions the fluctuations can wash out the mean-field bistability [121], in the case of collective coupling the mean-field equations become exact in the thermodynamic limit [122].

The system can be split into two subsystems (denoted by indices 1 and 2), according to the two cavity modes and the two pairs of (hyperfine) ground and excited states electric-dipole coupled to each of the cavity modes. Both subsystems, being just an ensemble of two-level atoms coupled to a single cavity mode, can be described in the same way as the system in Ch. 1. The only difference, importantly for the scheme, is that atoms from the excited levels may decay not only to the cavity-coupled ground state, i.e. $|e_i\rangle \leftrightarrow |g_i\rangle$, but cross decays $|e_1\rangle \rightarrow |g_2\rangle$, $|e_2\rangle \rightarrow |g_1\rangle$ are also possible with rates $\Gamma_1$ and $\Gamma_2$, respectively. This mechanism couples the subspaces 1 and 2. The drive 1 (2) is very far detuned from the transition $e_{2(1)} \rightarrow g_{2(1)}$,

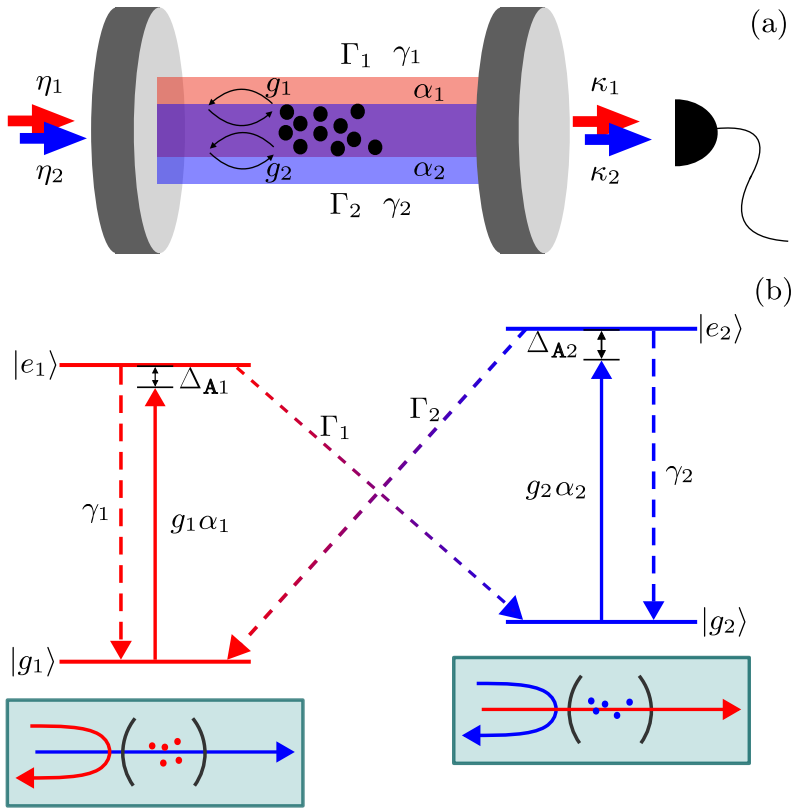


**Figure 4.1:** *(a) Parameters of the cavity QED scheme with two laser-driven modes interacting with an ensemble of atoms. The modes are spatially separated only for illustrative purposes, in practice, two fundamental modes of the cavity can be used. (b) Relevant level scheme of the atoms with two dipole-allowed transitions cross-coupled by relaxation processes. Schematic panels at the bottom represent that the atomic ground states switch the transmission or reflection of the cavity drives.*

thus no cross-coherence is created between the states 1 and 2. By extending Eq. (1.9) to include these considerations, the mean-field equations of motion become:

$$\begin{aligned}
\dot{\alpha}_1 &= (i\Delta_{\mathrm{C1}} - \kappa_1)\alpha_1 + g_1\, m_1 + \eta_1\,, \\
\dot{m}_1 &= (i\Delta_{\mathrm{A1}} - \gamma_1 - \Gamma_1)\, m_1 + g_1\,[n_{\mathrm{e1}} - n_{\mathrm{g1}}]\,\alpha_1\,, \\
\dot{n}_{\mathrm{e1}} &= -g_1\,[\alpha_1^* m_1 + m_1^* \alpha_1] - 2(\gamma_1 + \Gamma_1) n_{\mathrm{e1}}\,, \\
\dot{n}_{\mathrm{g1}} &= g_1\,[\alpha_1^* m_1 + m_1^* \alpha_1] + 2\gamma_1\, n_{\mathrm{e1}} + 2\Gamma_2\, n_{\mathrm{e2}}\,,
\end{aligned} \tag{4.1a}$$

$$
\begin{aligned}
\dot{\alpha}_2 &= (i\Delta_{\mathrm{C}2} - \kappa_2)\alpha_2 + g_2 m_2 + \eta_2 \,, \\
\dot{m}_2 &= (i\Delta_{\mathrm{A}2} - \gamma_2 - \Gamma_2)\, m_2 + g_2 \left[n_{\mathrm{e}2} - n_{\mathrm{g}2}\right] \alpha_2 \,, \\
\dot{n}_{\mathrm{e}2} &= -g_2 \left[\alpha_2^* m_2 + m_2^* \alpha_2\right] - 2(\gamma_2 + \Gamma_2) n_{\mathrm{e}2} \,, \\
\dot{n}_{\mathrm{g}2} &= g_2 \left[\alpha_2^* m_2 + m_2^* \alpha_2\right] + 2\gamma_2\, n_{\mathrm{e}2} + 2\Gamma_1\, n_{\mathrm{e}1}.
\end{aligned} \tag{4.1b}
$$

Without loss of generality, for simplicity, a symmetric case will be considered: the parameters with index $i = 1$ and $2$ are equal pairwise, $\gamma_i = \gamma$, $\Gamma_i = \Gamma$, $\kappa_i = \kappa$, and $g_i = g$ for $i = 1, 2$. Resonant driving of the cavity modes will be considered, i.e. $\Delta_{\mathrm{C}1} = \Delta_{\mathrm{C}2} = 0$. The cavity linewidth $\kappa = 1.32\gamma$ and the atom-cavity coupling are taken from the experiment presented in the previous chapter, for this latter the single atom coupling $g(N = 1) = 0.1\gamma$. Without loss of generality, $\Gamma = \gamma$ is chosen. The effect of the coherent drive $\eta_1$ on the atomic variables involving states 2 scale with $(\omega_1 - \omega_2)^{-1}$, which is the inverse of the hyperfine splitting, i.e. $1/(10^3\gamma)$ and is thus negligibly small compared to the other variables. The drive amplitudes $\eta_1$ and $\eta_2$ are left to be the control parameters of the system, which can be tuned to explore different phases and transitions between them.

Note that $N$ does not appear in the system (4.1), due to the scaling with $N$ of the dynamical variables and parameters before Eqs. (1.9). Moreover, $g$ with the above $\sqrt{N}$-scaled definition makes $g^2$ proportional to the ensemble cooperativity $\mathcal{C} \equiv \equiv g^2/\sqrt{(\Delta_{\mathrm{C}}^2 + \kappa^2)(\Delta_{\mathrm{A}}^2 + \gamma^2)}$. This latter quantity is a measure of nonlinearity, as attested by that optical bistability in a system of *two-level atoms* coupled to a cavity mode becomes possible in the $\mathcal{C} \sim 1$ regime. Note that for $\Gamma_i = 0$, the system (4.1) separates to two uncoupled two-level systems, where bistability would originate from the saturation of the atoms. Although a large atomic detuning, $\Delta_{\mathrm{A}}$ will be considered with respect to the linewidth $\gamma$ (for numerical calculations $\Delta_{\mathrm{A}} = -12\gamma$ was chosen), significant excited state population $n_{\mathrm{e}i}$ can occur for large intensities. This possibility is taken into account in these equations. Nevertheless, in the following, another solution of the mean-field equations will be studied, which is bound to the cross-coupling decay terms, and takes place in the low-excitation limit of the atoms.

## 4.3 Phase diagram

The steady state solution of Eqs. (4.1) can be obtained by setting the temporal derivatives on the left-hand side to zero. The remaining system of algebraic equations can be transformed into a single, 7th order polynomial equation with real coefficients for the variable $n_{\mathrm{e}1} - n_{\mathrm{g}1}$. Such an equation can have 1, 3, 5, or 7 real solutions out of which respectively 1, 2, 3, or 4 are stable, the rest are unstable. The number of stable solutions depends on the control parameters $\eta_1$ and $\eta_2$, as shown in the phase diagram in Figure 4.2.

The phase diagram depends on the cooperativity that in the present setup can be changed by the atom number $N$. Whereas $N = 5 \cdot 10^3$ (panel (a)) allows for 1 or 3 solutions only, the large atom numbers $N = 10^5$ and $10^6$ (panels (c) and (d)) give rise to domains with 5 (orange edge of the bright yellow domain) or even 7 solutions (bright yellow domain). An intermediate phase diagram is obtained for $N = 10^4$ (panel (b)) where a domain with 5 solutions exist, but one with 7 solutions does not. Closer look at the concrete solutions in the domains with 5 and 7 solutions (not shown here) reveal that the excited states $n_{\mathrm{e}i}$ are significantly populated, while the polarizations $m_i$ have low values. This means that the steady states correspond to statistical mixtures, i.e., the quantum purity of the state is low. In the following, we will focus on the bottom left corner of the phase diagrams, where only one or two stable solutions exist.

The different solutions in a given domain of the phase diagram are distinct in a macroscopic observable, which is the transmitted power $\kappa|\alpha_i|^2$ in our case ($i = = 1, 2$). This is a suitable order parameter of phases and is readily obtained from the mean-field model. The solution (valid for our case of $\Delta_C = 0$ and $|\Delta_{\mathrm{A}}| \gg \gamma + \Gamma$) reads

$$|\alpha_i|^2 = \frac{\eta_i^2}{\kappa^2} \frac{1}{1 + \mathcal{C}^2 (n_{\mathrm{e}i} - n_{\mathrm{g}i})^2}, \tag{4.2}$$

highlighting the role of the cooperativity as a measure of nonlinearity. The factor $\eta_i^2/\kappa^2$ is simply the number of photons in the resonantly driven empty cavity and will be used as a normalization factor. The second factor above can be identified as

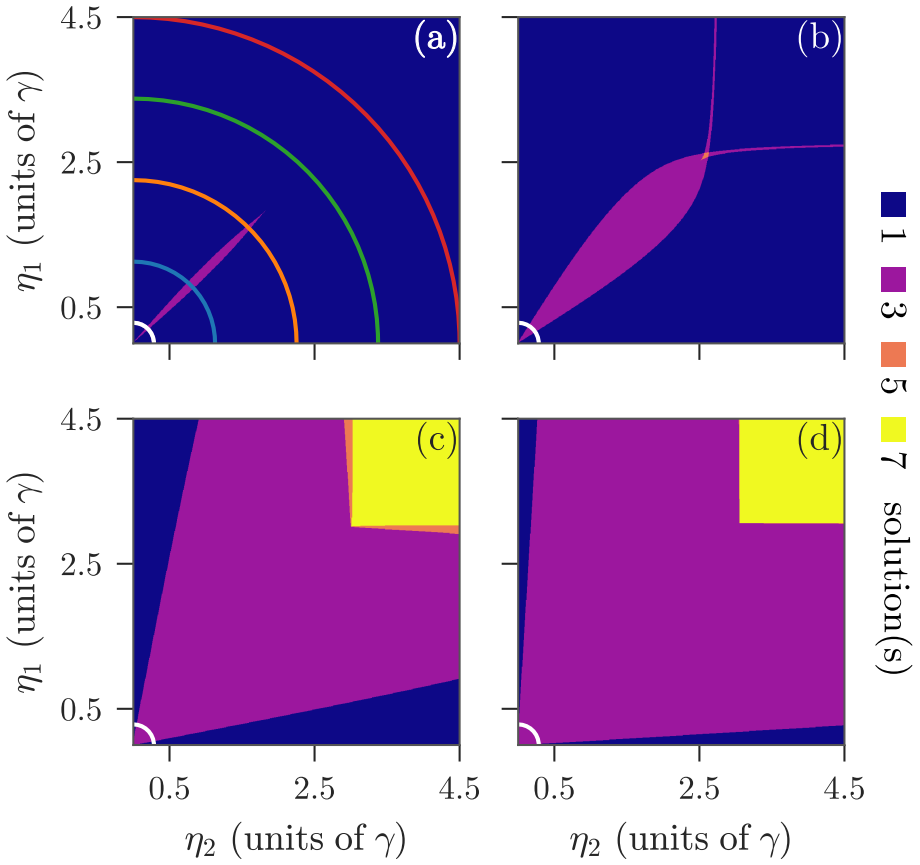


**Figure 4.2:** *Phase diagram with domains with different number of solutions of the system (4.1) on the plane of the drive amplitudes $\eta_1$, $\eta_2$. The cooperativity increases from (a) to (d), corresponding to atom numbers $N = 5 \cdot 10^3$, $10^4$, $10^5$, and $10^6$, respectively, with the single atom coupling $g(N = 1) = 0.1\gamma$. Relevant quantities along the coloured quarter circular arcs plotted on the phase diagrams will be shown later in Figs. 4.3 and 4.4. Radii of the coloured circular arcs are $\eta/\gamma = 0.29$, 1.13, 2.25, 3.38, 4.5. The white arcs in the low drive limit are of particular interest with respect to DQPT. The symmetry to the diagonal is a consequence of the artificial choice of equal parameters for the 1 and 2 transitions.*

transmittance. Equation (4.2) is not an explicit solution, as the population difference $n_{ei} - n_{gi}$ depends on the intracavity intensity $|\alpha_i|^2$. However, this form allows for getting insight to the phases.

If the population $n_{g1} \simeq 1$ and $n_{e1} \ll n_{g1}$, the transmittance through the mode 1 is suppressed for large cooperativity $\mathcal{C} \gg 1$. As there is no field in the cavity mode 1, all the atoms being in state $|g_1\rangle$ is a stable solution. On the other hand, according to the solution above with $n_{e2} \approx 0$ and $n_{g2} \approx 0$, mode 2 is closely resonantly excited, which

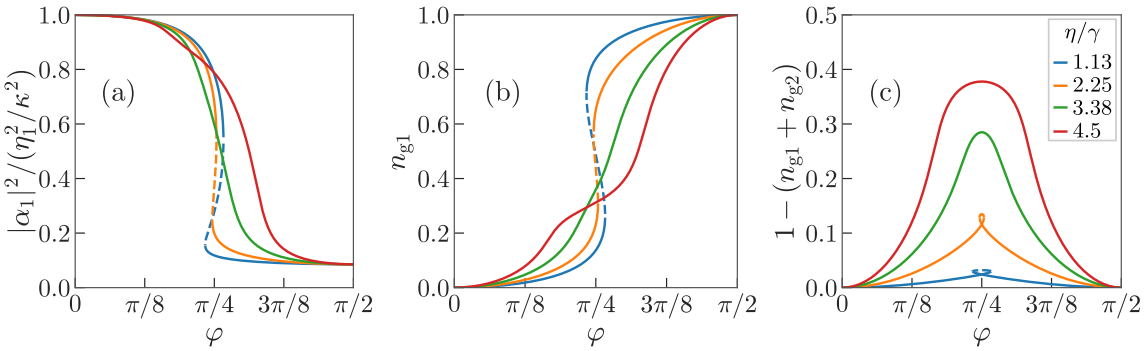


**Figure 4.3:** *Crossing domains with multiple stable solutions along the circular arcs in Fig. 4.2 (a) ($N = 5 \cdot 10^3$). The transmittance of cavity for mode 1 (a), and relative atomic population (b-c) are shown in corresponding colour as a function of the arc angle $\varphi$ measured from the vertical axis. Solid (dashed) lines correspond to stable (unstable) solutions.*

leads to transmittance 1. Reversely, there is also a stable solution in which all the atoms are in $|g_2\rangle$, i.e. $n_{g2} \simeq 1$, and the transmittance of mode 1 is close to unity. The domain with 3 solutions in Fig. 4.2 corresponds to the case when these stable steady states coexist. This will be further investigated along circular sections of the phase diagram, i.e., where $\eta_1^2 + \eta_2^2 \equiv \eta^2$ is constant. As the total input power per atom is proportional to $\eta_1^2 + \eta_2^2$, this section represents a fixed total drive intensity per atom, and increasing the angle $\varphi = \arctan \eta_2/\eta_1$ from 0 to $\pi/2$ corresponds to a continuous switching from driving mode 1 to 2.

Figure 4.3 shows cavity transmittance (a), ground state (b) and total excited state populations (c) as a function of the angle measured from axis $\eta_1$ for case $N = 5000$ along circular arcs of various radii plotted in Figure 4.2 (a) with the same colours. Because of the $1 \leftrightarrow 2$ symmetry of the scheme, the plot of the same quantities with index 2 are just the mirror images of the ones with index 1, therefore only the latter is shown. The red and the green arcs do not cross the bistable region, hence there is only one real solution along those, which is, of course, stable. The rest of the curves, both for the transmittance and the ground state population, show a characteristic S-shaped form of a bistability with overlapping stable solutions (solid line) connected by an unstable one (dashed line). The stability has been checked by means of linear perturbation analysis on Eqs. (4.1). High (low) transmittance corresponds to low

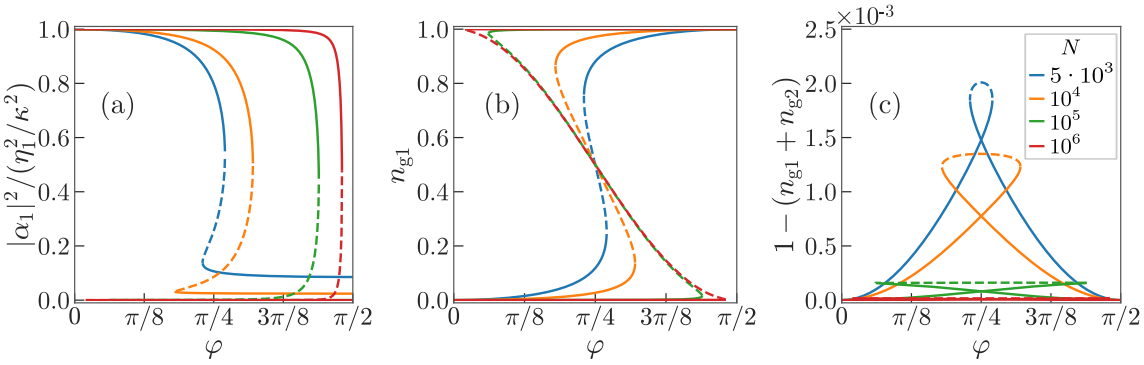


**Figure 4.4:** *Finite size scaling to the thermodynamic limit. The order parameter represented by the transmittance of cavity for mode 1 is plotted in (a), and relative atomic population are shown in (b-c) along the circular arcs on the phase space in Figure 4.2 (a) with a radius of $\eta/\gamma = 0.29$ for different atom numbers $N$. $\varphi$ is measured from the vertical axis. Solid (dashed) lines correspond to stable (unstable) solutions.*

(high) relative ground state population. For decreasing the total input power, the S-shaped curves show convergence in panels (a) and (b), whereas a gradual decrease of the population in the excited states is shown in (c). In this limit, the bistability is formed between the two hyperfine ground states, the excited states being only virtually populated underway the two-photon transition between the ground states. One can identify thus a dissipative quantum phase transition in the spirit of the three conditions given in the introduction, where in particular, the phases correspond to quantum states of high purity.

The thermodynamic limit, where the duality of metastable phases becomes a phase transition, can be defined as $\mathcal{C} \to \infty$ while $\eta$ is kept constant. In a practical case, the cooperativity can be increased by the atom number, hence the $N \to \infty$ implies that the actual drive power $N\,\eta^2$ has to go to infinity. The axes of the phase diagrams in Figure 4.2 already used this scaling. Therefore, the circular arcs of a radius $\eta/\gamma = 0.29$, plotted in each phase diagram (white), are fixed in the finite-size scaling. While the boundaries of the multivalued domain vary slightly, the phase diagram is qualitatively the same. For increasing cooperativity (via atom number), Fig. 4.4 (a) and (b) show that the S-shaped curve tends to a sharper Z-shaped one (mirrored). Interestingly, when going towards the thermodynamic limit, both so-

lutions become stable in almost the total range of the control parameter $\eta_2/\eta_1$.The initial condition determines which phase the system takes in the bistability domain. Even a very strong drive $\eta_{1(2)}$ can not kick off the atoms from the state $g_{1(2)}$ because the light cannot penetrate into the cavity. Simultaneously, as shown in Fig. 4.4 (c), the population in the excited states tends to completely vanish in this limit. Thus, in the thermodynamic limit, the proposed system has two stable solutions with the atoms being in one of the ground states $|g_{1(2)}\rangle$ and the other mode 2 (1) being populated by a coherent state, meaning that in this limit, the perfect quantum purity of the phases of the system is achieved.

## 4.4 Conclusion

I have proposed an experimentally accessible scheme, featuring metastability of steady states turning into true bistability, that is, a first-order dissipative quantum phase transition in a non-extensive thermodynamic limit, where, moreover, the phases become pure collective states. The four-level atomic scheme can be realized to a good approximation within the hyperfine structure of e.g. the $D_2$ line of rubidium-87, as discussed in the previous chapter. The atom number can be varied in a controlled way over many orders of magnitude in an experiment, allowing thus for a finite-size scaling to the thermodynamic limit. Beside the investigation of fundamental concepts of phase transitions in mesoscopic quantum systems, the bistability between long-lived ground states holds prospects for new atomic memory architectures.

# Chapter 5

# Demonstration of strong coupling of a subradiant atom array to a cavity vacuum

## 5.1 Introduction

In the experiment discussed in Ch. 3, the atoms in the optical resonator were driven from the side in order to pump them optically back to a ground state coupled by the cavity to an excited state. The main control parameter was the intensity of this repumper laser. However, the repumper laser was very far from resonance with any of the cavity modes, hence the repumper laser photons could not have been scattered into the cavity. In the following experimental research work, we studied a scheme in which the transverse drive was close to resonance with a cavity mode and photon scattering into the resonator was possible. Here, the frequency fine-tuning of the transverse drive becomes a relevant parameter beside its intensity. Furthermore, as a new element with respect to the breakdown experiments, the position of the atoms within the resonator was much better controlled as an essential element of the phenomenology. In particular, the atoms have been ordered and sustained in an intra-cavity optical lattice dipole trap rather than in a magnetic trap.

Considering atoms as linearly polarizable particles is a conventional approach when they are weakly illuminated, so that the atomic saturation is low. Even if the complicated internal electronic structure can be neglected, the interaction with low-intensity light, basically Rayleigh scattering, can still produce a large variety of interesting phenomena, depending on the specific electromagnetic configuration. Collective atomic emission, for example, is of great interest, particularly in the context of superradiance [123–127] and subradiance [128–130]. The latter has application in long-term storage of quantum information [131–133]. Accordingly, there has been an extensive study of regular three-dimensional atomic arrays [134] in which geometric constraints lead to destructive interference of the scattered light. Increased storage time, i.e., the collective suppression of spontaneous emission, has been shown to correspond to optical guided modes in the atomic array [135]. In addition to ordering atoms, the radiation can also be tailored to favour specific output channels in the scattering process, for example, when coupling to fibre-guided modes, [136, 137] where subradiant behaviour has been both predicted and experimentally demonstrated [138].

In this chapter, we revisit low-intensity light scattering from a one-dimensional atomic array in a subradiant configuration, when the scattered output is directed into strongly coupled radiation modes sustained by an optical resonator [139, 140]. Dynamics of laser-driven atoms interacting with cavity field modes is of high interest producing a great variety of effects: experiments started with efficient cooling schemes [141], atomic self-organization [51, 142, 143] and led to the exploration of superradiant [144–146] and other types of quantum phase transitions [46, 50, 54, 55, 59, T1, 147–151]. Collective radiation effects in many-atom cavity QED systems have been observed, such as the interference in Rayleigh scattering with controlled positioning of atoms in a cavity mode [139, 140, 152–154], quantum non-demolition measurements [155] have been performed, as well as lasing [156, 157] and superradiant lasing [158–160] with cold atoms as the gain media.

We will study the spectral and polarization properties of light scattered off a cold atomic ensemble into a quasi-resonant mode of a high-finesse optical cavity. The

atoms are arranged into a lattice with periodicity incommensurate with respect to the wavelength of the cavity mode resonant with the driven atomic transition. In such a configuration, destructive interference inhibits the build-up of a coherent field in the cavity, hence this configuration of atoms is referred to as a subradiant array. Experimental evidence will be presented that this interference, however, does not result in a decoupling from the cavity field. A strong collective coupling between the atomic ensemble and a cavity mode is manifested by vacuum Rabi splitting [161–163] in the spectrum of the outcoupled cavity field intensity fluctuations. Another remarkable effect is revealed, i.e., the rotation of field polarization by the subradiant array. In coherent scattering, the dipole moment of an atom is parallel with the polarization of the exciting optical field; hence, the scattered light preserves this polarization. This component is, however, suppressed by the destructive interference. The incoherent scattering is enhanced in a high-finesse cavity also into the mode with polarization orthogonal to that of the incoming field. The polarization rotation is accompanied by a two-photon Raman transition between Zeeman sublevels in the atomic hyperfine ground state manifold in accordance with the conservation of angular momentum [120, 145, 164]. We will see that this process is on the same order of the drive power and reflects the same vacuum Rabi splitting spectrum as the polarization-preserving scattering.

Prior to the experiment, my task was to build the optical path of the transverse drive, sketched in Fig. 2.7. Its beam is derived from the science laser and joined with the path of the optical pumping beam by a non-polarizing beamsplitter. Since it shares the mirrors with the vertical part of the MOT alignment, I have also built an independent adjustment setup. Regarding the frequency requirements of the transverse drive laser, I have implemented a phase-locked loop (PLL), developed in our group, which enables fine-tuning near resonance and provides sub-Hz precision relative to the reference. As the intensity of the detected signal was expected to be very low, I also had to connect the system to a superconducting nanowire single photon detector (SNSPD), and later to avalanche single photon counter (SPC) modules. Both detectors work with a time controller device, which I had to implement into the

experiment software control.

## 5.2 Experiment

The experimental scheme is sketched in Fig. 5.1. Rubidium atoms were collected in an $805\,\mathrm{nm}$ intra-cavity optical dipole lattice, described in Subsection 2.4.6. The atomic cloud was then driven in a direction perpendicular to the cavity axis, at an angular frequency $\omega$, with varying detuning from the $F = 2 \leftrightarrow F' = 3$ transition, $\omega_{\mathrm{A}}$. This laser was phase-locked to the reference laser with a variable detuning from the atomic resonance. The beam waist was $1\,\mathrm{mm}$, the power in each direction was adjusted from $0.15\,\mu\mathrm{W}$ to $256\,\mu\mathrm{W}$ by means of an acousto-optic modulator (AOM). The angular frequency $\omega_{\mathrm{C}}$ of another (undriven) longitudinal mode was set to resonance with $\omega_{\mathrm{A}}$, such that the transverse drive had equal detuning with respect to the atom, $\Delta_{\mathrm{A}} \equiv \omega - \omega_{\mathrm{A}}$, as it had to the cavity mode, $\Delta_{\mathrm{C}} \equiv \omega - \omega_{\mathrm{C}}$, i.e. $\Delta \equiv \Delta_{\mathrm{A}} = \Delta_{\mathrm{C}}$. Simultaneously, the $F = 1 \leftrightarrow F' = 2$ transition was also driven resonantly by the repumper laser (see Subsection 2.1.3), in order to keep the atoms in the $F = 2 \leftrightarrow F' = 3$ cycle.

Cavity photons could be generated only by scattering from the transverse laser drive beams. Since the atomic distribution had a periodicity incommensurate with the wavelength of the drive ($780\,\mathrm{nm}$), the scattered wave components from different positions of the mode were expected to have averaged to zero along the cavity axis [140, 165]. Such destructive interference is imposed by the geometry, regardless of the intensity, detuning and polarization of the drive. Even if coherent field build-up in the cavity mode was suppressed, presence of photon field fluctuations was expected. Such was the case, and the outcoupled cavity field was detected by single-photon counters after passing through a polarizing beamsplitter (PBS) discriminating between horizontally ('y') and vertically ('z') polarized photons.

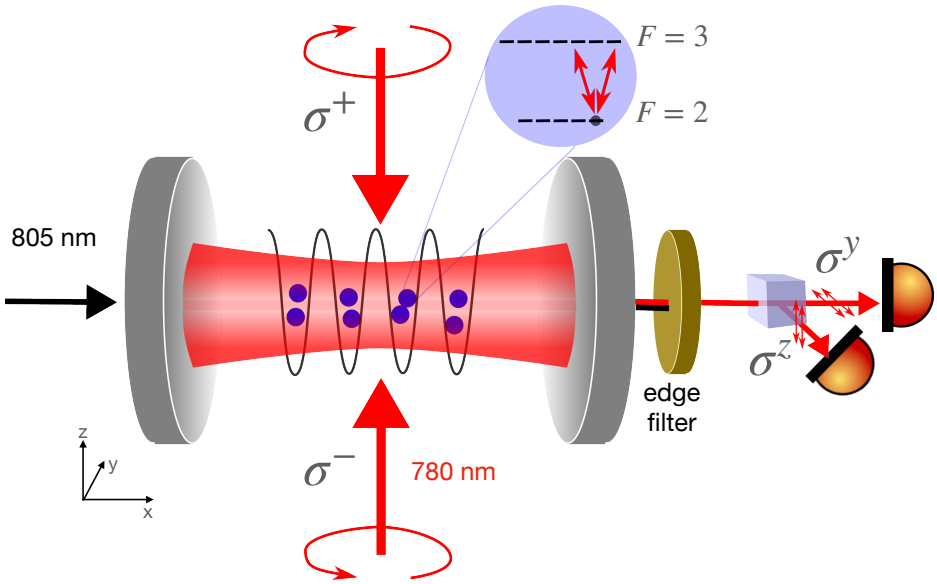


**Figure 5.1:** *Scheme of our experiment on the scattering from a subradiant atomic configuration. Cold $^{87}$Rb atoms in an intra-cavity dipole lattice at wavelength 805 nm are illuminated by two counter-propagating coherent laser beams with equal intensity and opposite circular polarizations from the two opposite directions perpendicular to the cavity axis. The laser was set near resonant with the $F = 2 \leftrightarrow F = 3$ transition of the $D_2$ line at $780\,\mathrm{nm}$ and close to resonance with one of the fundamental cavity modes. The cavity field output is split using a polarizing beamsplitter (PBS) to distinguish photon polarization. Both the horizontal and vertical polarization beams were coupled into a fibre, and they are monitored by single photon detectors (see Sec. 2.3). The cavity linewidth is $\kappa = 2\pi \cdot 3\,\mathrm{MHz}$ (HWHM), the maximum single-atom coupling constant is $g = 2\pi \cdot 0.33\,\mathrm{MHz}$.*

## 5.3 Vacuum Rabi splitting

As a first step, the number of atoms loaded into the mode volume was varied in the range of $\sim 1500$ to $\sim 10^4$ by systematically adjusting the Rb dispenser current, the duration of the MOT collection and the switch-on time of the transverse drive laser. The effective atom number was determined from independent measurements: it was calibrated by the cavity transmission of a near resonant probe detuned from the atomic transition, such that the atoms acted as a dispersive medium. The drive laser intensity was lowered as much as possible ($16\,\mu\mathrm{W}$) so that a reasonable rate of photons (in the range of $\mathrm{kHz}$, with an estimated maximum of cavity photon number $0.014$, producing a saturation around 1.5%), scattered by the atoms into the cavity

and then outcoupled from it, still could be detected by a superconducting nanowire single photon detector (SNSPD). At fixed atom number and drive intensity, the drive laser detuning $\Delta$ was varied in the range of $\pm 50\,\mathrm{MHz}$ to record a spectrum. Figure 5.2 presents that the intensity fluctuations reflected the vacuum Rabi splitting for large enough atom number. The observed large variance is intrinsic to the pho-

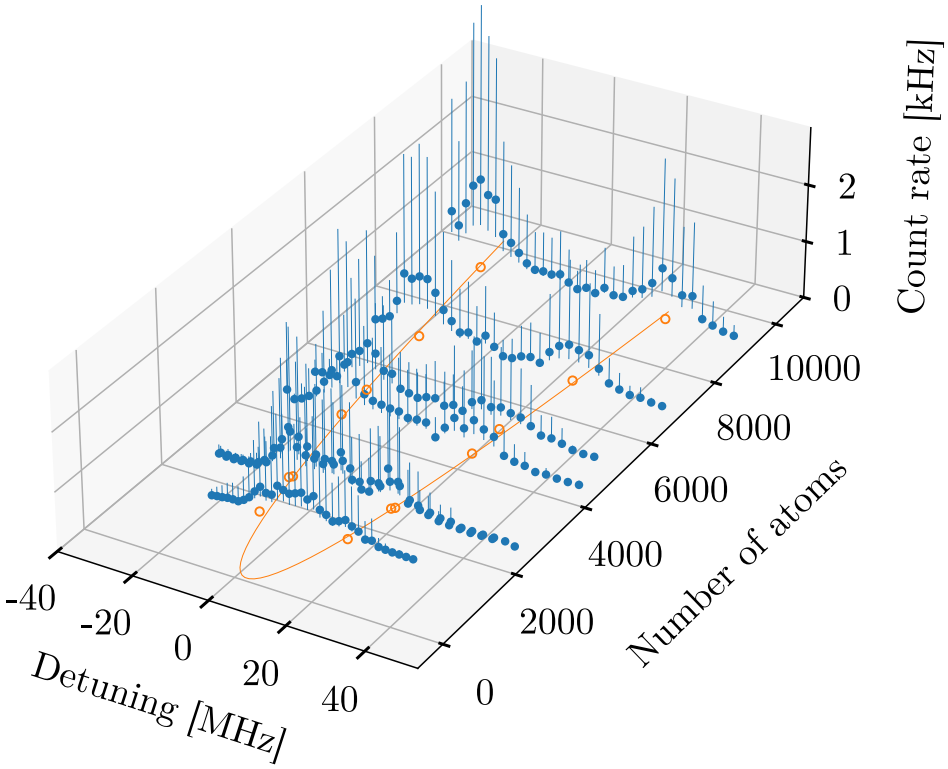


**Figure 5.2:** *Vacuum Rabi splitting with a subradiant array of atoms. The photon count rate in the first* $1\,\mathrm{ms}$ *of exposure time is plotted versus the laser drive detuning* $\Delta$ *for various atom numbers* $N$*. Horizontal and vertical polarizations are summed up. Each point and error bar is obtained from an ensemble of 70 runs assuming log-normal distribution, given that the photon count rate is a priori a non-negative quantity. The photons were counted by a superconducting nanowire single photon detector (SNSPD). The maxima of the doublets, projected on the bottom plane (orange circles), fit well on a parabola* $N = \Delta^2/g_{\mathrm{eff}}^2$ *with* $g_{\mathrm{eff}} = 2\pi \cdot 0.26\,\mathrm{MHz}$*, in accordance with the* $\sqrt{N}$ *dependence known for the collective coupling of a number of* $N$ *atoms to a single cavity mode.*

ton statistics: it indicates that the mean-field vanishes, which is in agreement with our expectation that the atoms ordered with a periodicity of the half of the $805\,\mathrm{nm}$ wavelength form a subradiant configuration. This expectation was verified in a subsequent step by a more involved analysis. The spectra have been fit by a sum of two

Lorentzians providing for the peak maxima indicated by empty orange circles in the bottom plane. The parabola fit on these peak positions is thus a $\sqrt{N}$ function, clearly evidencing that a strong collective coupling between the atomic ensemble and the mode is present. The coefficient $g_{\mathrm{eff}} \approx 2\pi \cdot 0.26\,\mathrm{MHz}$ from the fit is in good agreement with the expected value of $2\pi \cdot 0.225\,\mathrm{MHz}$ which can be obtained by averaging over the atomic population distributed evenly in the $F = 2, m_F$ magnetic sublevels with different Clebsch-Gordan coefficients. The 10% deviation is attributed to the small but not entirely negligible saturation in the atom number calibration measurement.

## 5.4 Linear scattering

In the next step, the vacuum Rabi splitting spectrum was analysed for a range of drive powers in order to verify that the scattering is in the linear regime. The recorded spectra could be compared to a simple theory based on a linear polarizability model of atoms [45] which assumes that the atomic induced dipole is proportional to the local electric field, $\vec{d} \propto \epsilon_0 \chi(\omega) \vec{E}(\vec{r})$ in the low-excitation limit [44].

In our configuration, the two counterpropagating beams have opposite circular polarizations. The resulting electric field is linearly polarized in a helical pattern along the drive axis 'z', i.e., $\vec{E}(\vec{r}) \| \vec{e}_y \cos kz + \vec{e}_x \sin kz$. Note that the optical resonator does not sustain modes with $\vec{e}_x$ polarization, being the direction of the cavity axis; hence, effectively, only the linear polarization $\vec{e}_y$ couples into the resonator field. Linear scatterers lead then to the intracavity field amplitude for the mode polarized in the direction 'y' [44, 140]

$$\alpha_y = \frac{\eta\, g \sum_a \cos kx_a \cos kz_a}{(i\Delta_{\mathrm{A}} - \gamma)(i\Delta_{\mathrm{C}} - \kappa) + g^2 \sum_a \cos^2 kx_a}\,, \tag{5.1}$$

where $\eta$ is an effective drive amplitude and the summation goes over the atoms indexed by $a = 1 \ldots N$ with positions $\vec{r}_a$. The modulus square of the denominator has two minima which, for our setting of resonance between the atoms and the mode, $\Delta_{\mathrm{A}} = \Delta_{\mathrm{C}} = \Delta$, are at $\Delta = \pm\sqrt{g^2 \sum_a \cos^2 kx_a} \equiv \pm\sqrt{N_{\mathrm{eff}}}\, g$. The effective atom number

is around $N_{\rm eff} \approx N/2$ for $\overline{\cos^2 kx} = 1/2$. This two-peaked resonance behaviour is responsible for the normal mode splitting shown in Fig. 5.2. A destructive interference leads to vanishing mean field, $\overline{\alpha}$, which is formally represented by that the numerator averages to zero over the atomic positions, $\langle \sum_a \cos kx_a \cos kz_a \rangle = 0$. This is the case for a homogeneous distribution, and also for a set of positions $\{x_a\}$ sampling the $805\,\mathrm{nm}$ wavelength optical lattice. Even if the mean vanishes, however, there are finite size fluctuations of the atomic distribution, which result in cavity field intensity fluctuations, $\overline{|\Delta\alpha_y|^2} \neq 0$. Considering the atomic positions as random variables, the statistical average gives

$$\left\langle \left| \sum_a \cos kx_a \cos kz_a \right|^2 \right\rangle \approx N^\beta/4 \,, \tag{5.2}$$

where the proportionality to the number of atoms has been taken into account with an exponent $\beta$. The actual value of the exponent can be deduced from our measured data and gives information on the atomic distribution. For destructive interference $\beta = 1$; this is expected for our case, where the distribution of atoms is incommensurate with the mode function $\cos kx$. If $\beta > 1$ was measured, it would imply the presence of a coherent component in the field amplitude, ultimately, exponent $\beta = 2$ would correspond to superradiance and perfect constructive interference. In the large vacuum Rabi splitting regime and in leading order of $(\kappa^2 + \gamma^2)/N_{\rm eff} g^2 \ll 1$, the spectrum of the intensity fluctuations around the peak maxima can be approximated by

$$S_y(\Delta) \approx \frac{\eta^2\, N^{\beta-1}}{8} \left[ (\Delta \pm \sqrt{N_{\rm eff}}\, g)^2 + \left( \frac{\kappa+\gamma}{2} \right)^2 \right]^{-1} . \tag{5.3}$$

In the experiment, the averaging over many realizations may involve a random variation of the atom number. On taking this into account, the Eq. (5.3) is modified and the peak intensity scaling on resonance gets a correction:

$$S_{\max}(\Delta_{\rm peak}) = \frac{4\eta^2 N^{\beta-1}}{(\kappa+\gamma)^2} \left( 1 - \frac{4g^2}{(\kappa+\gamma)^2} \frac{\delta N^2}{\overline{N}} \right) , \tag{5.4}$$

where $\delta N$ is the variance around the mean $\bar{N}$. The correction is, however, small for the sub-Poissonian atom number statistics in our MOT.

This form of the Rabi splitting peaks can be tested experimentally to verify the linear polarizability model of atoms. Moreover, this is a crucial result because it provides a direct measure of $\beta$ via the scaling of the peak intensity with the number of atoms $N$.

Figure 5.3 shows the detected photo-count rate, normalized to the pump power, as a function of the detuning $\Delta$, which was varied in the range of $\pm 30\,\mathrm{MHz}$. Although the linear polarizability model outlined above accounts only for horizontally polarized scattered light (a), similar spectra are recorded in vertical polarization as well (b), which will be explained in Sec. 5.6. As shown by the orange solid line, the spectrum deviates from the sum of two Lorentzian curves, in fact, the fit is composed of the sum of four Lorentzian functions. The inner two (smaller) peaks, which will be investigated in a subsequent study, are due to the multiplett structure of the hyperfine states. The outer two resonances are in very good agreement with Eq. (5.3) in three features, which confirms the validity of the linear scattering regime. First, the separation of the two outer peaks, indicated by red and blue crosses in the bottom plane for the negative and positive detunings, respectively, is constant in the range of pump powers investigated. It follows then that no noticeable atomic saturation takes place. As a by-product, this peak separation can be used to calibrate $N_{\mathrm{eff}}$. Second, the peak heights of the curves normalized to the input power, this latter being proportional to $\eta^2$, are also constant, which is shown by the empty circles on the side plane. In the case of the strongest drive plotted, some tendency of shrinking peak separation and decreasing peak height can be observed, indicating that at this power the scattering begins to leave the linear regime. Third, the linewidths of the vacuum Rabi peaks, represented by the line sections in the bottom plane, are also constant and are close to the theoretical value $(\kappa + \gamma)/2 = 2\pi \cdot 3\,\mathrm{MHz}$.

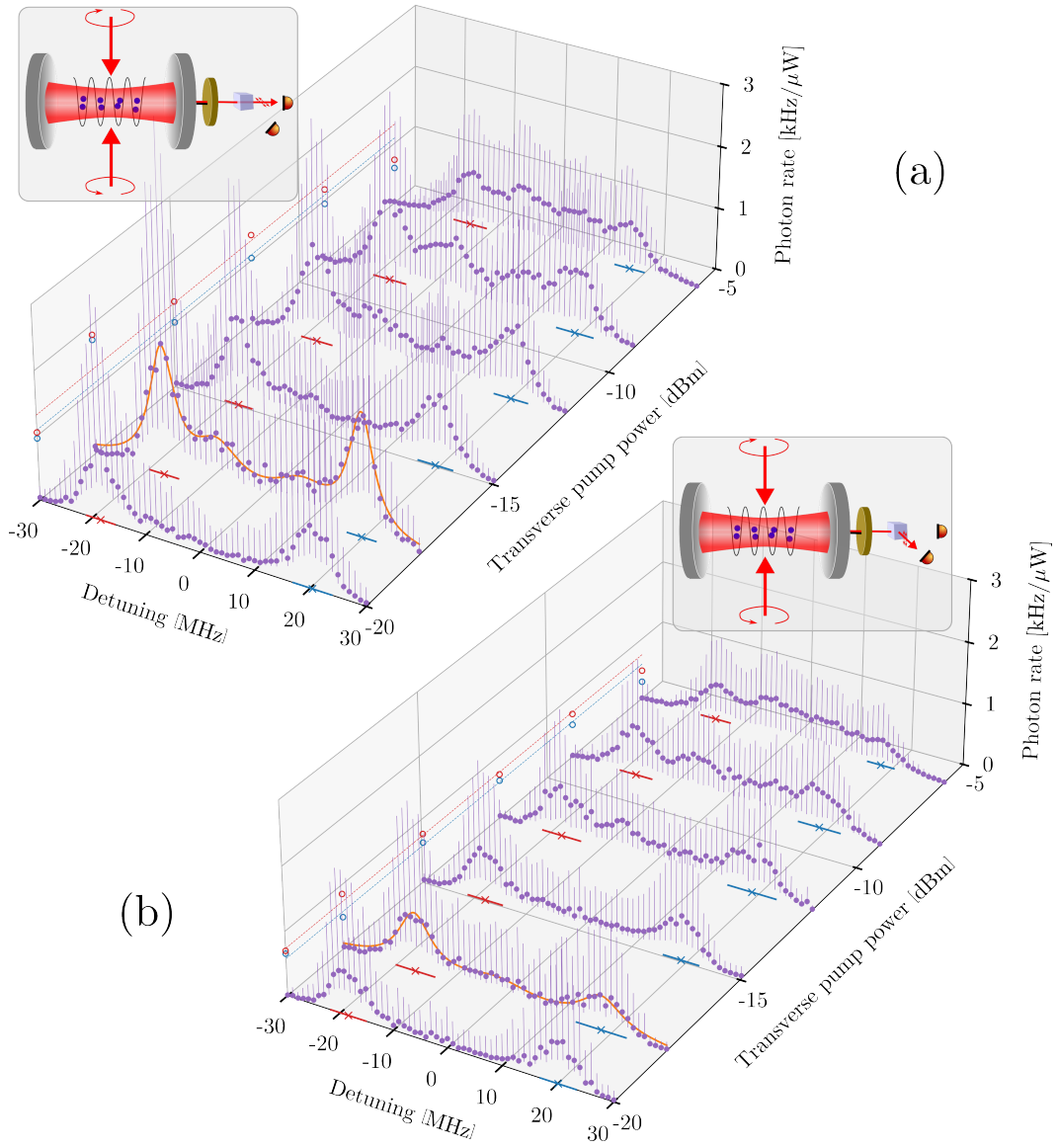


**Figure 5.3:** *Power dependence of the vacuum Rabi splitting spectrum for horizontal (a) and vertical (b) polarization. Each point is obtained from 50 runs by averaging the photon count rate in the first* $100\,\mu$s *of exposure.* $15$ ms *long signals were detected by single photon counter (SPC) modules with a time resolution of* $1\,\mu$s *and an overall detection efficiency of 50%. The detected photon rate is normalized to the laser drive power, which was set to* $10$, $16$, $32$, $64$, $128$ *and* $256\,\mu$W *for the spectra (shown in log scale, in units of* dBm*). A sum of four Lorentzian curves can be fit on each spectrum, one example is shown for the spectrum at the* $16\,\mu$W *drive power (*$-18$ dBm*, orange solid line). Heights of the fit spectra are projected onto the left plane, the corresponding detunings are projected onto the bottom plane (red and blue circles and crosses for negative and positive detunings, respectively). At* $256\,\mu$W *(*$-6$ dBm*), saturation manifests itself: the peaks are lower, and the splitting between them is also smaller. For the drive powers being safely in the linear scattering regime, the average of their heights is shown for reference by dashed lines on the left plane, red and blue, according to the sign of detuning.*

## 5.5 Subradiant atomic array

Having established the linearity of the scattering with driving power up to $64\,\mu\mathrm{W}$, the dependence of the photon fluctuations scattered into the cavity on the atom number was investigated at driving power $16\,\mu\mathrm{W}$ (the one with the fitted spectrum in Fig. 5.3). The registered photo-counts were integrated over only $100\,\mu\mathrm{s}$, in order to minimize the effects of atom loss and atomic motion. The drive frequency was tuned over the same range as in Fig. 5.3 so that the full spectrum was recorded. This allowed us (i) to calibrate the atom number from the distance of the peak maxima, and (ii) to determine the peak photo-count rate for the given atom number. The latter was compared with the maximum rate for vanishing detuning in the denominator of Eq. (5.3). The measured maximum rates, shown as a function of atom number in Fig. 5.4, scatter within 10% around a constant value. The power law fit yields an exponent slightly below 1, which is consistent with $\beta = 1$ in Eq. (5.3). This confirms the lack of coherent component in the scattered photon field and supports the observation of subradiance from an array of atoms. Beyond a simplified one-dimensional form of subradiance, the cavity does not merely enhance the scattering into a small solid angle for each individual atom, but the collective strong coupling to the cavity mode modifies the excitation spectrum of the atom array.

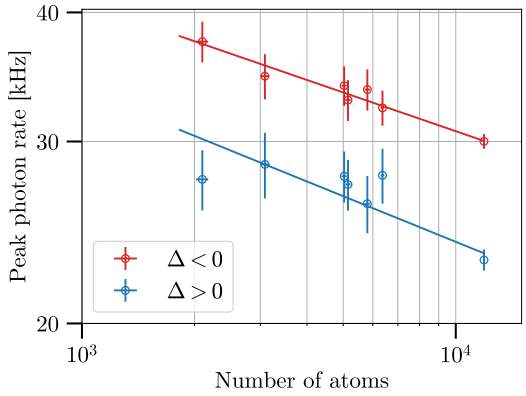


**Figure 5.4:** *Collective scattering as a function of the atom number. The maximum photon scattering rates on resonance, both at the negative (red) and positive (blue) side of the detuning, have been detected during the first* $100\,\mu$s *of transverse drive exposure. Horizontal and vertical polarizations are summed up. The exponents of the linear fit on the log-log scale are obtained* $\beta = 0.875 \pm 0.009$ *for the red and* $\beta = 0.853 \pm 0.031$ *for the blue, respectively.*

## 5.6 Polarization rotation

The strongly coupled vacuum field influences not only the spectral features of scattering but also the polarization, beyond the simple linear polarizability model presented above and leading to Eq. (5.1). The atomic polarization induced by the 'z' travelling $\sigma^{\pm}$ beams is expected to excite the 'y' polarized mode of the cavity, which corresponds to a Rayleigh scattering process. However, in linear order of the drive intensity, a photon flux was observed arising from the mode with polarization 'z' ($\sigma_0$) which is the direction of propagation of the input field. The scattering rate into the polarization 'z' as a function of the laser drive detuning for a range of drive powers is shown in Fig. 5.3(b). In full similarity with the 'y' polarization shown in panel (a), vacuum Rabi peaks with constant heights (normalized to the input power) and widths have been measured. The peak heights are close to those of the polarization-maintaining light scattering, which verifies that the coherent scattering from the subradiant array is strongly suppressed.

There are two sources of incoherent light: density fluctuations of Rayleigh scatterers and the incoherent scattering at the level of individual atoms. The prior can

yield only 'y' photons; hence, it underlies the difference between the recorded intensities in the two polarizations 'y' and 'z', respectively. The incoherent scattering from single atoms can be well incorporated into the semiclassical model of Eq. (5.1) for the cavity field amplitude $\alpha_y$: the averaging over the spatial distributions along the mode function $\cos kx_a$ can be complemented by random phase factors $e^{i\phi_a}$. Such an extension does not change the spectrum and the scaling with the atom number, which was thus correctly treated for the polarization 'y'. Concerning the polarization 'z', the underlying process is a Raman scattering in which the atoms undergo a hyperfine Zeeman-sublevel transition. The cavity-stimulated Raman scattering also scales linearly with the drive intensity. Note that this process has been exploited to realize quantum interfaces between light polarization and atomic memory states [166, 167] by means of stimulated adiabatic passage processes with pulsed excitation in single-atom strong-coupling cavity QED experiments. Cavity-enhanced Raman scattering has also been observed from a regular half-wavelength ordered array [140] when the drive is detuned from the atoms. This experiment revealed that the Raman scattering, though being an incoherent process in free space, manifests the vacuum Rabi splitting spectrum characteristic of the strong collective coupling of the atoms to the 'z' polarized cavity mode.

## 5.7 Conclusion

As evidenced above, an important conclusion is that radiation from atomic arrays is not only efficiently collected, but is substantially *modified* by the presence of a high-finesse resonator. Most importantly, the strong coupling to selected resonator modes imposes a *collective* scattering from the atoms into the resonator. This collective coupling, as I have demonstrated, is due to more than simply an interference effect, even in the extremely low intensity limit.

Such coupling can be seen in the vacuum-induced spectral features of our experiment. It suggests that new variants of the Dicke model [168], extended to disordered manifolds with cavity-mediated interactions, could be realized and simulated

in systems like presented here. In fact, considering that multiply excited subradiant states are said to be composed of the superposition of singly excited states in random ensembles [133], our system could be used to provide further insight into this superposition. In particular, such a system is well suited for time-resolved measurements and so the dynamics of the underlying subradiant states in the single-mode limit are now readily available.

Furthermore, I have shown that optical polarization rotation enters the linear scattering regime. On the one hand, the multiple ground-state level structure of atoms has to be taken into account in a linear polarizability description of atoms, beyond the usual scalar polarizability, which was noted as a subtlety in [135]. On the other hand, the multiple ground states open the scene for entanglement-based, new type of subradiant states predicted recently [169]. More generally, the cavity-enhanced polarization rotation could be the design basis for long-range many-body interactions between atoms mediated by two-mode fields. The cavity field fluctuations reflecting a non-trivial atom-cavity spectrum can be exploited as a useful light source when the mean-field is suppressed. Finally, the configuration presented here is very close to schemes for superradiant lasing [159] and for atomic clocks [146] which could be explored with the incommensurate lattice trap.

# Summary

In this thesis, driven-dissipative phase transitions and collective scattering properties of atoms have been explored within a system of cold rubidium-87 atoms coupled to a high-finesse optical cavity. My work, carried out in the Quantum Optics 'Momentum' Group of HUN–REN Wigner Research Centre for Physics, contributes both experimentally and theoretically to our understanding of light-matter interactions under collective strong coupling conditions.

A phase transition between hyperfine states of atoms has been demonstrated in an optical cavity, controlled by the intensities of external laser fields. The resulting phase diagram shows distinct dark and bright phases, with a bistable region emerging between them. By varying laser intensities, I have experimentally observed this transition, measuring hysteresis curves associated with the bistability.

As a theoretical extension of this system, I have constructed a model which leads to extreme properties in the bistability. An additional cavity mode and an additional atomic level have been taken into account. Phase diagrams for a variety of cooperativity parameters, i.e. in finite-size scaling, show that a broad range of the control parameter domain corresponds to coexistence of two semiclassical solutions that corresponds to the statistical mixture of phases represented by pure quantum states in the thermodynamic limit.

Collective scattering properties of cold rubidium atoms have been investigated in a new configuration: atoms were arranged in an intra-cavity optical lattice incommensurate with the resonant wavelength, and being excited by two counter-propagating, orthogonally circularly polarized laser beams, perpendicularly to the

cavity axis. Measuring the photon noise spectrum, collective strong atom-cavity coupling has been confirmed through the observation of vacuum Rabi splitting. Subradiance has also been demonstrated through scaling with the number of atoms.

Throughout my stay in the group, I have contributed to both experimental advancements and numerical modelling of these systems. This included development of a cavity stabilizing device, building new optical paths, and the implementation of single-photon detectors, as well as the creation of a versatile simulation package for modelling semiclassical and quantum dynamics within atom-cavity systems. This program allows for simulations involving multiple lasers and magnetic fields, greatly enhancing our capability to understand and design complex quantum-optical experiments.

In summary, this thesis gives account of experimental and theoretical results that enhance our understanding of driven-dissipative quantum systems and offer potential applications in quantum information storage, while also contributing tools and methods for future investigations in CQED and quantum technologies.

## Contributions of the thesis

The **first thesis group** summarizes the results of the publication [T1]. Detailed discussion can be found in Ch. 3.

I/1. I have shown that a first-order, driven-dissipative phase transition can be realized between hyperfine ground states of atoms loaded in a high-finesse optical cavity, by laser driving the resonator and the atoms. I have identified the intensities of the external fields as control parameters of the phase transition, and the mean intra-cavity photon number as an order parameter. Using semiclassical approximation, I have determined the phase diagram of the interacting system, in which two macroscopically discernible phases (dark and bright) are apparent, with a bistability region between the two.

I/2. I have experimentally observed the phase transition described in Thesis I/1

between hyperfine ground states $F = 1$ and $F = 2$ of laser cooled and magnetically trapped rubidium-87 atoms. Varying the intensities of the laser drive of the cavity mode and that of the atoms, I have identified the dark and bright phases, performed fast switching between them, and demonstrated bistability by measuring hysteresis curves on scanning the control parameters across the bistability region.

The **second thesis group** summarizes the results of the publication [T2]. Detailed discussion can be found in Ch. 4.

II/1. I have constructed a cavity QED model based on two driven cavity modes resonant with electronic transitions from different hyperfine ground states of atoms. Using semiclassical approximation, I have determined the phase diagram of the system under different cooperativities. Beyond the macroscopically discernible dark and bright phases and the bistable region, I have identified multistable regions as well, up to 4 coexisting phases.

II/2. I have performed a finite-size scaling of the phase transition, and showed that in the thermodynamic limit (that is in the case of infinite cooperativity), the phases correspond to pure collective quantum states: hyperfine ground states of atoms, and the bistability extends to the total range of the ratio of the two control parameters.

The **third thesis group** summarizes the results of the publication [T3]. Detailed discussion can be found in Chapter 5.

III/1. By loading cold rubidium atoms in an intra-cavity optical dipole lattice with a wavelength incommensurate with that of the atomic resonance, and illuminating them with laser perpendicularly to the cavity axis, I have observed

subradiant scattering from the array of atoms. I have found that the subradiant atomic ensemble does not decouple from the cavity mode: I have measured the spectrum of the photon noise arising from the fluctuations in the configuration of the atoms, and it shows vacuum Rabi splitting, the hallmark of strong collective coupling.

III/2. I have observed a significant polarization rotation effect by the atom array described in Thesis III/1. The incoherent scattering from the atoms is enhanced by the cavity also into the mode with polarization orthogonal to that of the incoming field. I have provided an explanation of the polarization rotation in terms of a two-photon Raman transition within the atomic hyperfine ground state manifold.

# Összefoglalás

Dolgozatomban nagy jósági tényezőjű optikai rezonátorhoz csatolt hideg rubídium-87 atomok rendszerén vizsgáltam hajtott-veszteséges fázisátalakulásokat és az atomok kollektív szórási tulajdonságait. Munkám, melyet a HUN–REN Wigner Fizikai Kutatóközpont Kvantumoptika "Lendület" Kutatócsoportjában végeztem, mind kísérleti, mind elméleti szempontból hozzájárul a kollektív erős csatolás mellett megvalósuló fény-anyag kölcsönhatások megértéséhez.

Külső lézeres gerjesztések intenzitásaival vezérelt fázisátalakulást mutattam ki atomok hiperfinom állapotai között, optikai rezonátorban. A fázisdiagram elkülönülő sötét és világos fázisokat mutat, köztük bistabil tartománnyal. Az átalakulást kísérletileg is megfigyeltem, kimérve a bistabilitáshoz tartozó hiszterézisgörbéket.

E rendszer elméleti kiterjesztéseként megalkottam egy olyan modellt, amely a bistabilitásban extrém tulajdonságokhoz vezet. A fázisdiagramok különböző kooperativitás-paraméterek mellett – vagyis végesméret-skálázásban – azt mutatják, hogy a termodinamikai határesetben tiszta kvantumállapotokkal megvalósított fázisok együtt létezhetnek a kontrollparaméterek széles tartományában.

Hideg rubídiumatomok optikai rezonátorban mutatott kollektív szórási tulajdonságait vizsgáltam, a rezonátor tengelyére merőleges irányú megvilágítás mellett. A fotonzaj spektrumát mérve igazoltam a kollektív erős csatolást az atomok és a rezonátor között a vákuum-Rabi-felhasadás megfigyelésével, valamint a szubradianciát az atomok számának változtatásával.

A csoportban eltöltött idő alatt hozzájárultam a laboratórium fejlesztéséhez és a kísérletek numerikus modellezéséhez. Részt vettem egy rezonátorstabilizáló eszköz

fejlesztésében, új optikai utakat építettem ki, egyfoton-detektorokat implementáltam a kísérleti rendszerbe. Általános célú szimulációs csomagot készítettem atom-rezonátor rendszerek szemiklasszikus és kvantumos modellezésére.

Összefoglalva, dolgozatom olyan kísérleti és elméleti eredményekről ad számot, melyek hozzájárulnak a hajtott-veszteséges kvantumrendszerek mélyebb megértéséhez, és alkalmazási lehetőséget kínálnak a kvantuminformáció-tárolás terén. Munkám egyúttal eszközökkel és módszerekkel is szolgál a rezonátoros kvantumelektrodinamika és a kvantumtechnológia további kutatásához.

# A disszertáció tézisei

Az **első téziscsoport** a [T1] publikáció eredményeit foglalja össze. A részletes bemutatás a 3. fejezetben található.

I/1. Megmutattam, hogy optikai rezonátorba helyezett atomok hiperfinom alapállapotai között elsőrendű, hajtott-veszteséges fázisátalakulást lehet megvalósítani a rezonátor és az atomok lézeres meghajtásával. Beazonosítottam a külső terek intenzitását mint a fázisátalakulás kontrollparamétereit, és a rezonátormódus fotonszámának várható értékét mint annak rendparaméterét. Szemiklasszikus közelítésben meghatároztam a kölcsönható rendszer fázisdiagramját, melyen két makroszkopikusan elkülöníthető (sötét és világos) fázis figyelhető meg, a kettő között pedig bistabil tartomány van.

I/2. Az I/1. tézispontban ismertett fázisátalakulást kísérletileg is megfigyeltem lézeresen hűtött és mágnesesen csapdázott rubídium-87 atomok $F = 1$ és $F = = 2$ hiperfinom alapállapotai között. A rezonátormódust illetve az atomokat gerjesztő lézerek intenzitását változtatva beazonosítottam a sötét és a világos fázist, gyors kapcsolást valósítottam meg közöttük, valamint a kontrollparaméterekkel pásztázva, hiszterézisgörbék mérésével kimutattam a bistabil tartományt.

A **második téziscsoport** a [T2] publikáció eredményeit foglalja össze. A részletes bemutatás a 4. fejezetben található.

II/1. Rezonátoros kvantumelektrodinamikai modellt alkottam két hajtott rezonátormódust véve alapul, melyek atomok különböző hiperfinom alapállapotaihoz tartozó dipólátmeneteivel rezonánsak. Szemiklasszikus közelítést alkalmazva meghatároztam a rendszer fázisdiagramját különböző kooperativitások mellett. A makroszkopikusan elkülönülő sötét és világos fázisok, valamint a bistabil tartomány mellett multistabil tartományokat is beazonosítottam, legfeljebb 4 koegzisztens fázissal.

II/2. Elvégeztem a fázisátalakulás végesméret-skálázását, és megmutattam, hogy a termodinamikai határesetben (vagyis végtelen kooperativitás esetében) a fázisok tiszta, kollektív kvantumállapotoknak, az atomok hiperfinom alapállapotainak felelnek meg, a bistabilitás pedig kiterjed a kontrollparaméterek arányának teljes tartományára.

A **harmadik téziscsoport** a [T3] publikáció eredményeit foglalja össze. A részletes bemutatás az 5. fejezetben található.

III/1. Hideg rubídiumatomokat nagy jósági tényezőjű optikai rezonátorban megvalósított, az atomi rezonancia hullámhosszával inkommenzurábilis optikai rácsba rendezve és a rezonátor tengelyére merőlegesen lézerrel megvilágítva az atomok szubradiáns szórását figyeltem meg. Megállapítottam, hogy a szubradiáns atomi sokaság nem csatolódik le a rezonátormódusról: megmértem az atomok konfigurációjában fellépő fluktuációkból származó fotonzaj spektrumát, amely az erős kollektív csatolásra jellemző vákuum Rabi-felhasadást mutatja.

III/2. Megfigyeltem a III/1. tézispontban leírt atomi sokaság polarizációforgató hatását. Az atomok inkoherens szórását a rezonátor erősíti, olyan módusban

is, amelynek polarizációja merőleges a beérkező mezőével. A polarizációforgatást megmagyaráztam az atomok hiperfinom alapállapoti sokaságában bekövetkező kétfotonos Raman-átmenettel.

# Publications

## Publications included in thesis


[T1] B. Gábor, D. Nagy, A. Dombi, T. W. Clark, F. I. B. Williams, K. V. Adwaith, A. Vukics, and P. Domokos. "Ground-state bistability of cold atoms in a cavity". In: *Phys. Rev. A* 107 (2 Feb. 2023), p. 023713. DOI: 10.1103/PhysRevA.107.023713. $\mathbf{IF}_{2024} = 2.9$

[T2] B. Gábor, D. Nagy, A. Vukics, and P. Domokos. "Quantum bistability in the hyperfine ground state of atoms". In: *Phys. Rev. Res.* 5 (4 Dec. 2023), p. L042038. DOI: 10.1103/PhysRevResearch.5.L042038. $\mathbf{IF}_{2024} = 4.2$

[T3] B. Gábor, A. K. Varooli, D. Varga, B. Sárközi, Á. Kurkó, A. Dombi, T. W. Clark, F. I. B. Williams, D. Nagy, A. Vukics, and P. Domokos. "Demonstration of strong coupling of a subradiant atom array to a cavity vacuum". In: *EPJ Quantum Technology* 12.1 (Aug. 2025), p. 93. DOI: 10.1140/epjqt/s40507-025-00401-x. $\mathbf{IF}_{2024} = 5.6$


## Further related publications


[F1] D. Varga, B. Gábor, B. Sárközi, K. Adwaith, D. Nagy, A. Dombi, T. Clark, F. Williams, P. Domokos, and A. Vukics. "Loading atoms from a large magnetic trap to a small intra-cavity optical lattice". In: *Physics Letters A* 505 (2024), p. 129444. DOI: 10.1016/j.physleta.2024.129444. $\mathbf{IF}_{2024} = 2.6$

# Bibliography


[1] M. Planck. “Zur Theorie des Gesetzes der Energieverteilung im Normalspektrum”. In: *Berlin* (1900), pp. 237–245.

[2] A. Einstein. “Über einen die Erzeugung und Verwandlung des Lichtes betreffenden heuristischen Gesichtspunkt”. In: *Annalen der Physik* 322.6 (Jan. 1905), pp. 132–148. DOI: 10.1002/andp.19053220607.

[3] A. Einstein. “Strahlungs-Emission und Absorption nach der Quantentheorie”. In: *Deutsche Physikalische Gesellschaft* 18 (Jan. 1916), pp. 318–323.

[4] A. Einstein. “Zur Quantentheorie der Strahlung”. In: *Physikalische Zeitschrift* 18 (Jan. 1917), pp. 121–128.

[5] N. Bohr. “I. On the constitution of atoms and molecules”. In: *The London, Edinburgh, and Dublin Philosophical Magazine and Journal of Science* 26.151 (1913), pp. 1–25. DOI: 10.1080/14786441308634955. eprint: https://doi.org/10.1080/14786441308634955.

[6] De Broglie, Louis. “Recherches sur la théorie des Quanta”. In: *Ann. Phys.* 10.3 (1925), pp. 22–128. DOI: 10.1051/anphys/192510030022.

[7] W. Heisenberg. “Über quantentheoretische Umdeutung kinematischer und mechanischer Beziehungen.” In: *Zeitschrift fur Physik* 33.1 (Dec. 1925), pp. 879–893. DOI: 10.1007/BF01328377.

[8] E. Schrödinger. “Quantisierung als Eigenwertproblem”. In: *Annalen der Physik* 384.4 (1926), pp. 361–376. DOI: 10.1002/andp.19263840404. eprint: https://onlinelibrary.wiley.com/doi/pdf/10.1002/andp.19263840404.

[9] P. A. M. Dirac. “On the theory of quantum mechanics”. In: *Proceedings of the Royal Society of London. Series A* 112 (1926), pp. 661–677. DOI: 10.1098/rspa.1926.0133.

[10] J. von Neumann. *Mathematische Grundlagen der Quantenmechanik*. Berlin: Springer, 1932.

[11] A. G. J. Macfarlane, J. P. Dowling, and G. J. Milburn. “Quantum technology: the second quantum revolution”. In: *Philosophical Transactions of the Royal Society of London. Series A: Mathematical, Physical and Engineering Sciences* 361.1809 (2003), pp. 1655–1674.

[12] E. B. Kania and J. K. Costello. *QUANTUM HEGEMONY?: China’s Ambitions and the Challenge to U.S. Innovation Leadership*. Tech. rep. Center for a New American Security, 2018, pp. 3–5.

[13] A. Manzalini. “The Second Quantum Revolution is underway”. In: *TIM notiziariotecnico, year* 29 (2020).

[14] A. L. Bloom. “OPTICAL PUMPING”. In: *Scientific American* 203.4 (1960), pp. 72–81.

[15] C. Cohen-Tannoudji and A. Kastler. “I Optical Pumping”. In: ed. by E. Wolf. Vol. 5. Progress in Optics. Elsevier, 1966, pp. 1–81. DOI: https://doi.org/10.1016/S0079-6638(08)70450-5.

[16] W. HAPPER. “Optical Pumping”. In: *Rev. Mod. Phys.* 44 (2 Apr. 1972), pp. 169–249. DOI: 10.1103/RevModPhys.44.169.

[17] A. L. Migdall, J. V. Prodan, W. D. Phillips, T. H. Bergeman, and H. J. Metcalf. “First Observation of Magnetically Trapped Neutral Atoms”. In: *Phys. Rev. Lett.* 54 (24 June 1985), pp. 2596–2599. DOI: 10.1103/PhysRevLett.54.2596.

[18] D. J. Wineland and W. M. Itano. “Laser cooling of atoms”. In: *Physical Review A* 20.4 (1979), p. 1521.

[19] E. L. Raab, M. Prentiss, A. Cable, S. Chu, and D. E. Pritchard. “Trapping of Neutral Sodium Atoms with Radiation Pressure”. In: *Phys. Rev. Lett.* 59 (23 Dec. 1987), pp. 2631–2634. DOI: 10.1103/PhysRevLett.59.2631.

[20] J. Dalibard and C. Cohen-Tannoudji. “Laser cooling below the Doppler limit by polarization gradients: simple theoretical models”. In: *J. Opt. Soc. Am. B* 6.11 (Nov. 1989), pp. 2023–2045. DOI: 10.1364/JOSAB.6.002023.

[21] J. Miller, R. Cline, and D. Heinzen. “Far-off-resonance optical trapping of atoms”. In: *Physical Review A* 47.6 (1993), R4567.

[22] C. L. Degen, F. Reinhard, and P. Cappellaro. “Quantum sensing”. In: *Reviews of modern physics* 89.3 (2017), p. 035002.

[23] V. Giovannetti, S. Lloyd, and L. Maccone. “Advances in quantum metrology”. In: *Nature photonics* 5.4 (2011), pp. 222–229.

[24] S. Pirandola, U. L. Andersen, L. Banchi, M. Berta, D. Bunandar, R. Colbeck, D. Englund, T. Gehring, C. Lupo, C. Ottaviani, et al. “Advances in quantum cryptography”. In: *Advances in optics and photonics* 12.4 (2020), pp. 1012–1236.

[25] N. Gisin and R. Thew. “Quantum communication”. In: *Nature Photonics* 1.3 (Mar. 2007), pp. 165–171. DOI: 10.1038/nphoton.2007.22.

[26] L. Henriet, L. Beguin, A. Signoles, T. Lahaye, A. Browaeys, G.-O. Reymond, and C. Jurczak. “Quantum computing with neutral atoms”. In: *Quantum* 4 (2020), p. 327.

[27] H. Ritsch, P. Domokos, F. Brennecke, and T. Esslinger. “Cold atoms in cavity-generated dynamical optical potentials”. In: *Rev. Mod. Phys.* 85 (2 Apr. 2013), pp. 553–601. DOI: 10.1103/RevModPhys.85.553.

[28] C. D. Bruzewicz, J. Chiaverini, R. McConnell, and J. M. Sage. “Trapped-ion quantum computing: Progress and challenges”. In: *Applied Physics Reviews* 6.2 (2019).

[29] J. Millen, T. S. Monteiro, R. Pettit, and A. N. Vamivakas. “Optomechanics with levitated particles”. In: *Reports on Progress in Physics* 83.2 (2020), p. 026401.

[30] J.-Q. You and F. Nori. “Atomic physics and quantum optics using superconducting circuits”. In: *Nature* 474.7353 (2011), pp. 589–597.

[31] Z. Bai, Z. Zhao, M. Tian, D. Jin, Y. Pang, S. Li, X. Yan, Y. Wang, and Z. Lu. “A comprehensive review on the development and applications of narrow-linewidth lasers”. In: *Microwave and Optical Technology Letters* 64.12 (2022), pp. 2244–2255.

[32] J. Kohler, J. A. Gerber, E. Dowd, and D. M. Stamper-Kurn. “Negative-Mass Instability of the Spin and Motion of an Atomic Gas Driven by Optical Cavity Backaction”. en. In: *Physical Review Letters* 120.1 (Jan. 2018), p. 013601. DOI: 10.1103/PhysRevLett.120.013601.

[33] Z. Chen, J. G. Bohnet, J. M. Weiner, K. C. Cox, and J. K. Thompson. “Cavity-aided nondemolition measurements for atom counting and spin squeezing”. en. In: *Physical Review A* 89.4 (Apr. 2014), p. 043837. DOI: 10.1103/PhysRevA.89.043837.

[34] H. Zhang, R. McConnell, S. Ćuk, Q. Lin, M. H. Schleier-Smith, I. D. Leroux, and V. Vuletić. “Collective State Measurement of Mesoscopic Ensembles with Single-Atom Resolution”. en. In: *Physical Review Letters* 109.13 (Sept. 2012), p. 133603. DOI: 10.1103/PhysRevLett.109.133603.

[35] R. D. Niederriter, C. Schlupf, and P. Hamilton. “Cavity probe for real-time detection of atom dynamics in an optical lattice”. en. In: *Physical Review A* 102.5 (Nov. 2020), p. 051301. DOI: 10.1103/PhysRevA.102.051301.

[36] J. Zeiher, J. Wolf, J. A. Isaacs, J. Kohler, and D. M. Stamper-Kurn. “Tracking Evaporative Cooling of a Mesoscopic Atomic Quantum Gas in Real Time”. en. In: *Physical Review X* 11.4 (Oct. 2021), p. 041017. DOI: 10.1103/PhysRevX.11.041017.

[37] E. Suarez, P. Wolf, P. Weiss, and S. Slama. “Superradiance decoherence caused by long-range Rydberg-atom pair interactions”. en. In: *Physical Review A* 105.4 (Apr. 2022), p. L041302. DOI: 10.1103/PhysRevA.105.L041302.

[38] J. A. Muniz, D. J. Young, J. R. K. Cline, and J. K. Thompson. “Cavity-QED measurements of the Sr 87 millihertz optical clock transition and determination of its natural linewidth”. en. In: *Physical Review Research* 3.2 (May 2021), p. 023152. DOI: 10.1103/PhysRevResearch.3.023152.

[39] G. Vallet, E. Bookjans, U. Eismann, S. Bilicki, R. L. Targat, and J. Lodewyck. “A noise-immune cavity-assisted non-destructive detection for an optical lattice clock in the quantum regime”. In: *New Journal of Physics* 19.8 (Aug. 2017), p. 083002. DOI: 10.1088/1367-2630/aa7c84.

[40] R. Hobson, W. Bowden, A. Vianello, I. R. Hill, and P. Gill. “Cavity-enhanced non-destructive detection of atoms for an optical lattice clock”. en. In: *Optics Express* 27.26 (Dec. 2019), p. 37099. DOI: 10.1364/OE.27.037099.

[41] S. A. Schäffer, M. Tang, M. R. Henriksen, A. A. Jørgensen, B. T. R. Christensen, and J. W. Thomsen. “Lasing on a narrow transition in a cold thermal strontium ensemble”. en. In: *Physical Review A* 101.1 (Jan. 2020), p. 013819. DOI: 10.1103/PhysRevA.101.013819.

[42] G. Yang, Z. Tan, B. Zou, and Y. Zhu. “Interference control of nonlinear excitation in a multi-atom cavity quantum electrodynamics system”. en. In: *Optics Letters* 39.23 (Dec. 2014), p. 6695. DOI: 10.1364/OL.39.006695.

[43] K. C. Cox, D. H. Meyer, Z. A. Castillo, F. K. Fatemi, and P. D. Kunz. “Spin-Wave Multiplexed Atom-Cavity Electrodynamics”. en. In: *Physical Review Letters* 123.26 (Dec. 2019), p. 263601. DOI: 10.1103/PhysRevLett.123.263601.

[44] H. Ritsch, P. Domokos, F. Brennecke, and T. Esslinger. “Cold atoms in cavity-generated dynamical optical potentials”. In: *Rev. Mod. Phys.* 85 (Apr. 2013). Publisher: American Physical Society, pp. 553–601.

[45] H. Tanji-Suzuki, I. D. Leroux, M. H. Schleier-Smith, M. Cetina, A. T. Grier, J. Simon, and V. Vuletić. "Interaction between Atomic Ensembles and Optical Resonators". en. In: *Advances In Atomic, Molecular, and Optical Physics* 60 (2011), pp. 201–237. DOI: 10.1016/B978-0-12-385508-4.00004-8.

[46] F. Mivehvar, F. Piazza, T. Donner, and H. Ritsch. "Cavity QED with quantum gases: new paradigms in many-body physics". en. In: *Advances in Physics* 70.1 (Jan. 2021), pp. 1–153. DOI: 10.1080/00018732.2021.1969727.

[47] D. Walls and G. J. Milburn. *Quantum Optics*. Springer Berlin Heidelberg, 2008, pp. 127–141. DOI: 10.1007/978-3-540-28574-8_7.

[48] H. M. Wiseman and G. J. Milburn. *Quantum Measurement and Control*. Cambridge: Cambridge University Press, 2009. DOI: 10.1017/CBO9780511813948.

[49] D. Nagy, G. Kónya, G. Szirmai, and P. Domokos. "Dicke-Model Phase Transition in the Quantum Motion of a Bose-Einstein Condensate in an Optical Cavity". In: *Phys. Rev. Lett.* 104 (Apr. 2010). Publisher: American Physical Society, p. 130401.

[50] K. Baumann, C. Guerlin, F. Brennecke, and T. Esslinger. "Dicke quantum phase transition with a superfluid gas in an optical cavity". In: *Nature* 464 (Apr. 2010). Publisher: Macmillan Publishers Limited. All rights reserved, pp. 1301–1306. DOI: 10.1038/nature09009.

[51] K. J. Arnold, M. P. Baden, and M. D. Barrett. "Self-Organization Threshold Scaling for Thermal Atoms Coupled to a Cavity". In: *Physical Review Letters* 109.15 (Oct. 2012), p. 153002. DOI: 10.1103/PhysRevLett.109.153002.

[52] D. Schmidt, H. Tomczyk, S. Slama, and C. Zimmermann. "Dynamical Instability of a Bose-Einstein Condensate in an Optical Ring Resonator". In: *Phys. Rev. Lett.* 112 (Mar. 2014). Publisher: American Physical Society, p. 115302.

[53] J. Klinder, H. Keßler, M. Wolke, L. Mathey, and A. Hemmerich. "Dynamical phase transition in the open Dicke model". In: *P. Natl. Acad. Sci. USA* (Mar. 2015). Publisher: National Academy of Sciences, p. 201417132.

[54] J. Léonard, A. Morales, P. Zupancic, T. Esslinger, and T. Donner. “Supersolid formation in a quantum gas breaking a continuous translational symmetry”. In: *Nature* 543.7643 (Mar. 2017), pp. 87–90. DOI: 10.1038/nature21067.

[55] A. J. Kollár, A. T. Papageorge, V. D. Vaidya, Y. Guo, J. Keeling, and B. L. Lev. “Supermode-density-wave-polariton condensation with a Bose–Einstein condensate in a multimode cavity”. In: *Nature Communications* 8.1 (Feb. 2017), p. 14386. DOI: 10.1038/ncomms14386.

[56] T. Fink, A. Schade, S. Höfling, C. Schneider, and A. Imamoglu. “Signatures of a dissipative phase transition in photon correlation measurements”. In: *Nature Physics* 14.4 (Apr. 2018), pp. 365–369. DOI: 10.1038/s41567-017-0020-9.

[57] *Official webpage of the Quantum Optics Group*. https://wigner.hu/en/quantum-optics-and-quantum-information/quantum-optics-group. Visited on 2024.09.19.

[58] A. Dombi, T. W. Clark, F. I. B. Williams, F. Jessen, J. Fortágh, D. Nagy, A. Vukics, and P. Domokos. “Collective self-trapping of atoms in a cavity”. In: *New Journal of Physics* 23.8 (Aug. 2021), p. 083036. DOI: 10.1088/1367-2630/ac1a3c.

[59] T. W. Clark, A. Dombi, F. I. B. Williams, Á. Kurkó, J. Fortágh, D. Nagy, A. Vukics, and P. Domokos. “Time-resolved observation of a dynamical phase transition with atoms in a cavity”. In: *Phys. Rev. A* 105 (6 June 2022), p. 063712. DOI: 10.1103/PhysRevA.105.063712.

[60] A. Vukics, T. Grießer, and P. Domokos. “Elimination of the $A$-Square Problem from Cavity QED”. In: *Phys. Rev. Lett.* 112 (7 Feb. 2014), p. 073601. DOI: 10.1103/PhysRevLett.112.073601.

[61] C. Cohen-Tannoudji. “Other Equivalent Formulations of Electrodynamics”. In: *Photons and Atoms*. John Wiley & Sons, Ltd, 1997. Chap. 4, pp. 253–359. DOI:

https://doi.org/10.1002/9783527618422.ch4. eprint: https://onlinelibrary.wiley.com/doi/pdf/10.1002/9783527618422.ch4.

[62] C. Cohen-Tannoudji, J. Dupont-Roc, and G. Grynberg. "Optical Bloch Equations". In: *Atom-Photon Interactions*. John Wiley & Sons, Ltd, 1998. Chap. 5, pp. 353–405. DOI: https://doi.org/10.1002/9783527617197.ch5. eprint: https://onlinelibrary.wiley.com/doi/pdf/10.1002/9783527617197.ch5.

[63] D. A. Steck. *Rubidium 87 D Line Data*. http://steck.us/alkalidata. (revision 2.3.2, 10 September 2023).

[64] A. Franzen. *ComponentLibrary*. https://www.gwoptics.org/ComponentLibrary/. Most symbols of optical elements in the figures of this thesis are taken from *ComponentLibrary* by Alexander Franzen, licensed under a Creative Commons Attribution-NonCommercial 3.0 Unported License.

[65] B. E. A. Saleh and M. C. Teich. *Fundamentals of Photonics*. John Wiley & Sons, Inc., Aug. 1991.

[66] D. W. Preston. "Doppler-free saturated absorption: Laser spectroscopy". In: *American Journal of Physics* 64.11 (Nov. 1996), pp. 1432–1436. DOI: 10.1119/1.18457.

[67] E. D. Black. "An introduction to Pound–Drever–Hall laser frequency stabilization". In: *American Journal of Physics* 69.1 (Jan. 2001), pp. 79–87. DOI: 10.1119/1.1286663.

[68] C. G. Townsend, N. H. Edwards, C. J. Cooper, K. P. Zetie, C. J. Foot, A. M. Steane, P. Szriftgiser, H. Perrin, and J. Dalibard. "Phase-space density in the magneto-optical trap". In: *Phys. Rev. A* 52 (2 Aug. 1995), pp. 1423–1440. DOI: 10.1103/PhysRevA.52.1423.

[69] M. Walhout, U. Sterr, and S. L. Rolston. "Magnetic inhibition of polarization-gradient laser cooling in $\sigma_+$-$\sigma_-$ optical molasses". In: *Phys. Rev. A* 54 (3 Sept. 1996), pp. 2275–2279. DOI: 10.1103/PhysRevA.54.2275.

[70] R. Grimm, M. Weidemüller, and Y. B. Ovchinnikov. “Optical dipole traps for neutral atoms”. In: *Advances in atomic, molecular, and optical physics*. Vol. 42. Elsevier, 2000, pp. 95–170.

[71] B. O. Goes, C. E. Fiore, and G. T. Landi. “Quantum features of entropy production in driven-dissipative transitions”. In: *Phys. Rev. Res.* 2 (1 Feb. 2020), p. 013136. DOI: 10.1103/PhysRevResearch.2.013136.

[72] G. Jaeger. “The Ehrenfest Classification of Phase Transitions: Introduction and Evolution”. In: *Archive for History of Exact Sciences* 53.1 (May 1998), pp. 51–81. DOI: 10.1007/s004070050021.

[73] A. Vukics, A. Dombi, J. M. Fink, and P. Domokos. “Finite-size scaling of the photon-blockade breakdown dissipative quantum phase transition”. In: *Quantum* 3 (June 2019), p. 150. DOI: 10.22331/q-2019-06-03-150.

[74] P. Brookes, G. Tancredi, A. D. Patterson, J. Rahamim, M. Esposito, T. K. Mavrogordatos, P. J. Leek, E. Ginossar, and M. H. Szymanska. “Critical slowing down in circuit quantum electrodynamics”. en. In: *Science Advances* 7.21 (May 2021), eabe9492. DOI: 10.1126/sciadv.abe9492.

[75] J. B. Curtis, I. Boettcher, J. T. Young, M. F. Maghrebi, H. Carmichael, A. V. Gorshkov, and M. Foss-Feig. “Critical theory for the breakdown of photon blockade”. en. In: *Physical Review Research* 3.2 (Apr. 2021), p. 023062. DOI: 10.1103/PhysRevResearch.3.023062.

[76] F. Reiter, T. L. Nguyen, J. P. Home, and S. F. Yelin. “Cooperative Breakdown of the Oscillator Blockade in the Dicke Model”. en. In: *Physical Review Letters* 125.23 (Nov. 2020), p. 233602. DOI: 10.1103/PhysRevLett.125.233602.

[77] B. Megyeri, G. Harvie, A. Lampis, and J. Goldwin. “Directional Bistability and Nonreciprocal Lasing with Cold Atoms in a Ring Cavity”. en. In: *Physical Review Letters* 121.16 (Oct. 2018), p. 163603. DOI: 10.1103/PhysRevLett.121.163603.

[78] J. Hannukainen and J. Larson. “Dissipation-driven quantum phase transitions and symmetry breaking”. In: *Phys. Rev. A* 98 (4 Oct. 2018), p. 042113. DOI: 10.1103/PhysRevA.98.042113.

[79] S. R. K. Rodriguez, W. Casteels, F. Storme, N. Carlon Zambon, I. Sagnes, L. Le Gratiet, E. Galopin, A. Lemaître, A. Amo, C. Ciuti, and J. Bloch. “Probing a Dissipative Phase Transition via Dynamical Optical Hysteresis”. In: *Phys. Rev. Lett.* 118 (24 June 2017), p. 247402. DOI: 10.1103/PhysRevLett.118.247402.

[80] W. Casteels, R. Fazio, and C. Ciuti. “Critical dynamical properties of a first-order dissipative phase transition”. In: *Phys. Rev. A* 95 (1 Jan. 2017), p. 012128. DOI: 10.1103/PhysRevA.95.012128.

[81] H. Carmichael. *An Open Systems Approach to Quantum Optics*. Springer-Verlag Berlin Heidelberg, 1993.

[82] A. Lambrecht, J. M. Courty, S. Reynaud, and E. Giacobino. “Cold atoms: A new medium for quantum optics”. en. In: *Applied Physics B Laser and Optics* 60.2-3 (1995), pp. 129–134. DOI: 10.1007/BF01135854.

[83] T. Elsasser, B. Nagorny, and A. Hemmerich. “Optical bistability and collective behavior of atoms trapped in a high-Q ring cavity”. In: *Physical Review A* 69.3 (Mar. 2004). Publisher: American Physical Society, pp. 033403+. DOI: 10.1103/PhysRevA.69.033403.

[84] R. Culver, A. Lampis, B. Megyeri, K. Pahwa, L. Mudarikwa, M. Holynski, P. W. Courteille, and J. Goldwin. “Collective strong coupling of cold potassium atoms in a ring cavity”. In: *New Journal of Physics* 18.11 (Nov. 2016), p. 113043. DOI: 10.1088/1367-2630/18/11/113043.

[85] A. Kawasaki, B. Braverman, E. Pedrozo-Peñafiel, C. Shu, S. Colombo, Z. Li, Ö. Özel, W. Chen, L. Salvi, A. Heinz, D. Levonian, D. Akamatsu, Y. Xiao, and V. Vuleti ć. “Geometrically asymmetric optical cavity for strong atom-photon

coupling". In: *Phys. Rev. A* 99 (1 Jan. 2019), p. 013437. DOI: 10.1103/PhysRevA.99.013437.

[86] H. J. Carmichael. "Breakdown of Photon Blockade: A Dissipative Quantum Phase Transition in Zero Dimensions". In: *Phys. Rev. X* 5.3 (Sept. 2015). Publisher: American Physical Society, p. 031028. DOI: 10.1103/PhysRevX.5.031028.

[87] J. M. Fink, A. Dombi, A. Vukics, A. Wallraff, and P. Domokos. "Observation of the Photon-Blockade Breakdown Phase Transition". en. In: *Physical Review X* 7.1 (Jan. 2017), p. 011012. DOI: 10.1103/PhysRevX.7.011012.

[88] U. Martini, C. Ginzel, and A. Schenzle. "Optical bistability and nonclassical photon counting statistics with few atoms". In: *Optics Communications* 102.3-4 (Oct. 1993), pp. 379–390. DOI: 10.1016/0030-4018(93)90409-x.

[89] A. Lambrecht, E. Giacobino, and J. Courty. "Optical nonlinear dynamics with cold atoms in a cavity". In: *Optics Communications* 115.1 (1995), pp. 199–206. DOI: https://doi.org/10.1016/0030-4018(94)00493-E.

[90] J. A. Sauer, K. M. Fortier, M. S. Chang, C. D. Hamley, and M. S. Chapman. "Cavity QED with optically transported atoms". In: *Physical Review A* 69.5 (May 2004), pp. 051804+. DOI: 10.1103/PhysRevA.69.051804.

[91] R. Sawant and S. A. Rangwala. "Optical-bistability-enabled control of resonant light transmission for an atom-cavity system". In: *Physical Review A* 93.2 (Feb. 2016). Publisher: American Physical Society, p. 023806. DOI: 10.1103/PhysRevA.93.023806.

[92] L. A. Lugiato. *II Theory of Optical Bistability*. Vol. 21. Elsevier, 1984, pp. 69–216. DOI: 10.1016/s0079-6638(08)70122-7.

[93] L. Davidovich. "Sub-Poissonian processes in quantum optics". en. In: *Reviews of Modern Physics* 68.1 (Jan. 1996), pp. 127–173. DOI: 10.1103/RevModPhys.68.127.

[94] H. M. Gibbs, S. L. McCall, and T. N. C. Venkatesan. “Differential Gain and Bistability Using a Sodium-Filled Fabry-Perot Interferometer”. In: *Physical Review Letters* 36.19 (May 1976), pp. 1135–1138. DOI: 10.1103/physrevlett.36.1135.

[95] A. T. Rosenberger, L. A. Orozco, and H. J. Kimble. “Observation of absorptive bistability with two-level atoms in a ring cavity”. en. In: *Physical Review A* 28.4 (Oct. 1983), pp. 2569–2572. DOI: 10.1103/PhysRevA.28.2569.

[96] H. J. Carmichael. “Quantum fluctuations in absorptive bistability without adiabatic elimination”. en. In: *Physical Review A* 33.5 (May 1986), pp. 3262–3269. DOI: 10.1103/PhysRevA.33.3262.

[97] H. J. Carmichael. “Quantum—Classical Correspondence for the Electromagnetic Field I: The Glauber—Sudarshan P Representation”. In: *Statistical Methods in Quantum Optics 1: Master Equations and Fokker-Planck Equations*. Berlin, Heidelberg: Springer Berlin Heidelberg, 1999, pp. 75–99. DOI: 10.1007/978-3-662-03875-8_3.

[98] L. Davidovich, A. Maali, M. Brune, J. M. Raimond, and S. Haroche. “Quantum switches and nonlocal microwave fields”. In: *Phys. Rev. Lett.* 71 (15 Oct. 1993), pp. 2360–2363. DOI: 10.1103/PhysRevLett.71.2360.

[99] Q. A. Turchette, C. J. Hood, W. Lange, H. Mabuchi, and H. J. Kimble. “Measurement of Conditional Phase Shifts for Quantum Logic”. In: *Phys. Rev. Lett.* 75 (25 Dec. 1995), pp. 4710–4713. DOI: 10.1103/PhysRevLett.75.4710.

[100] E. M. Kessler, G. Giedke, A. Imamoglu, S. F. Yelin, M. D. Lukin, and J. I. Cirac. “Dissipative phase transition in a central spin system”. In: *Phys. Rev. A* 86 (1 July 2012), p. 012116. DOI: 10.1103/PhysRevA.86.012116.

[101] K. Macieszczak, M. Guţă, I. Lesanovsky, and J. P. Garrahan. “Towards a theory of metastability in open quantum dynamics”. In: *Physical review letters* 116.24 (2016), p. 240404.

[102] T. E. Lee, H. Haeffner, and M. Cross. “Collective quantum jumps of Rydberg atoms”. In: *Physical review letters* 108.2 (2012), p. 023602.

[103] C. Ates, B. Olmos, J. P. Garrahan, and I. Lesanovsky. “Dynamical phases and intermittency of the dissipative quantum Ising model”. In: *Phys. Rev. A* 85 (4 Apr. 2012), p. 043620. DOI: 10.1103/PhysRevA.85.043620.

[104] M. Marcuzzi, E. Levi, S. Diehl, J. P. Garrahan, and I. Lesanovsky. “Universal nonequilibrium properties of dissipative Rydberg gases”. In: *Physical review letters* 113.21 (2014), p. 210401.

[105] C. Carr, R. Ritter, C. G. Wade, C. S. Adams, and K. J. Weatherill. “Nonequilibrium Phase Transition in a Dilute Rydberg Ensemble”. In: *Phys. Rev. Lett.* 111 (11 Sept. 2013), p. 113901. DOI: 10.1103/PhysRevLett.111.113901.

[106] N. Malossi, M. M. Valado, S. Scotto, P. Huillery, P. Pillet, D. Ciampini, E. Arimondo, and O. Morsch. “Full Counting Statistics and Phase Diagram of a Dissipative Rydberg Gas”. In: *Phys. Rev. Lett.* 113 (2 July 2014), p. 023006. DOI: 10.1103/PhysRevLett.113.023006.

[107] A. Urvoy, F. Ripka, I. Lesanovsky, D. Booth, J. Shaffer, T. Pfau, and R. Löw. “Strongly correlated growth of Rydberg aggregates in a vapor cell”. In: *Physical Review Letters* 114.20 (2015), p. 203002.

[108] F. Letscher, O. Thomas, T. Niederprüm, M. Fleischhauer, and H. Ott. “Bistability Versus Metastability in Driven Dissipative Rydberg Gases”. In: *Phys. Rev. X* 7 (2 May 2017), p. 021020. DOI: 10.1103/PhysRevX.7.021020.

[109] R. Labouvie, B. Santra, S. Heun, and H. Ott. “Bistability in a Driven-Dissipative Superfluid”. In: *Phys. Rev. Lett.* 116 (23 June 2016), p. 235302. DOI: 10.1103/PhysRevLett.116.235302.

[110] J. Benary, C. Baals, E. Bernhart, J. Jiang, M. Röhrle, and H. Ott. “Experimental observation of a dissipative phase transition in a multi-mode many-body quantum system”. In: *New Journal of Physics* 24.10 (Oct. 2022), p. 103034. DOI: 10.1088/1367-2630/ac97b6.

[111] F. Ferri, R. Rosa-Medina, F. Finger, N. Dogra, M. Soriente, O. Zilberberg, T. Donner, and T. Esslinger. "Emerging Dissipative Phases in a Superradiant Quantum Gas with Tunable Decay". In: *Phys. Rev. X* 11 (4 Dec. 2021), p. 041046. DOI: 10.1103/PhysRevX.11.041046.

[112] G. Dagvadorj, M. Kulczykowski, M. H. Szyma ńska, and M. Matuszewski. "First-order dissipative phase transition in an exciton-polariton condensate". In: *Phys. Rev. B* 104 (16 Oct. 2021), p. 165301. DOI: 10.1103/PhysRevB.104.165301.

[113] M. Fitzpatrick, N. M. Sundaresan, A. C. Y. Li, J. Koch, and A. A. Houck. "Observation of a Dissipative Phase Transition in a One-Dimensional Circuit QED Lattice". In: *Phys. Rev. X* 7 (1 Feb. 2017), p. 011016. DOI: 10.1103/PhysRevX.7.011016.

[114] R. Sett, F. Hassani, D. Phan, S. Barzanjeh, A. Vukics, and J. M. Fink. "Emergent Macroscopic Bistability Induced by a Single Superconducting Qubit". In: *PRX Quantum* 5 (1 Feb. 2024), p. 010327. DOI: 10.1103/PRXQuantum.5.010327.

[115] R. Bonifacio and L. A. Lugiato. "Photon statistics and spectrum of transmitted light in optical bistability". In: *Physical Review Letters* 40.15 (1978), p. 1023.

[116] R. Bonifacio and L. A. Lugiato. "Bistable absorption in a ring cavity". In: *Lettere al Nuovo Cimento (1971-1985)* 21.15 (Apr. 1978), pp. 505–509. DOI: 10.1007/BF02763161.

[117] A. Dombi, A. Vukics, and P. Domokos. "Optical bistability in strong-coupling cavity QED with a few atoms". In: *Journal of Physics B: Atomic, Molecular and Optical Physics* 46.22 (2013). Publisher: IOP Publishing, p. 224010.

[118] T. L. Heugel, M. Biondi, O. Zilberberg, and R. Chitra. "Quantum Transducer Using a Parametric Driven-Dissipative Phase Transition". In: *Phys. Rev. Lett.* 123 (17 Oct. 2019), p. 173601. DOI: 10.1103/PhysRevLett.123.173601.

[119] Dombi, András, Vukics, András, and Domokos, Peter. “Bistability effect in the extreme strong coupling regime of the Jaynes-Cummings model”. In: *Eur. Phys. J. D* 69.3 (2015), p. 60. DOI: 10.1140/epjd/e2015-50861-9.

[120] E. Suarez, F. Carollo, I. Lesanovsky, B. Olmos, P. W. Courteille, and S. Slama. “Collective atom-cavity coupling and nonlinear dynamics with atoms with multilevel ground states”. en. In: *Physical Review A* 107.2 (Feb. 2023), p. 023714. DOI: 10.1103/PhysRevA.107.023714.

[121] H. Landa, M. Schiró, and G. Misguich. “Multistability of Driven-Dissipative Quantum Spins”. In: *Phys. Rev. Lett.* 124.4 (Jan. 2020). Publisher: American Physical Society, p. 043601. DOI: 10.1103/PhysRevLett.124.043601.

[122] F. Carollo and I. Lesanovsky. “Exactness of Mean-Field Equations for Open Dicke Models with an Application to Pattern Retrieval Dynamics”. In: *Phys. Rev. Lett.* 126.23 (June 2021). Publisher: American Physical Society, p. 230601. DOI: 10.1103/PhysRevLett.126.230601.

[123] M. Gross and S. Haroche. “Superradiance: An essay on the theory of collective spontaneous emission”. en. In: *Physics Reports* 93.5 (Dec. 1982), pp. 301–396. DOI: 10.1016/0370-1573(82)90102-8.

[124] R. G. DeVoe and R. G. Brewer. “Observation of Superradiant and Subradiant Spontaneous Emission of Two Trapped Ions”. en. In: *Physical Review Letters* 76.12 (Mar. 1996), pp. 2049–2052. DOI: 10.1103/PhysRevLett.76.2049.

[125] S. Inouye, A. P. Chikkatur, D. M. Stamper-Kurn, J. Stenger, D. E. Pritchard, and W. Ketterle. “Superradiant Rayleigh Scattering from a Bose-Einstein Condensate”. In: *Science* 285 (July 1999), pp. 571–574.

[126] M. O. Araújo, I. Krešić, R. Kaiser, and W. Guerin. “Superradiance in a Large and Dilute Cloud of Cold Atoms in the Linear-Optics Regime”. en. In: *Physical Review Letters* 117.7 (Aug. 2016), p. 073002. DOI: 10.1103/PhysRevLett.117.073002.

[127] G. Ferioli, A. Glicenstein, I. Ferrier-Barbut, and A. Browaeys. “A non-equilibrium superradiant phase transition in free space”. en. In: *Nature Physics* 19.9 (Sept. 2023), pp. 1345–1349. DOI: 10.1038/s41567-023-02064-w.

[128] W. Guerin, M. O. Araújo, and R. Kaiser. “Subradiance in a Large Cloud of Cold Atoms”. en. In: *Physical Review Letters* 116.8 (Feb. 2016), p. 083601. DOI: 10.1103/PhysRevLett.116.083601.

[129] D. Das, B. Lemberger, and D. D. Yavuz. “Subradiance and superradiance-to-subradiance transition in dilute atomic clouds”. en. In: *Physical Review A* 102.4 (Oct. 2020), p. 043708. DOI: 10.1103/PhysRevA.102.043708.

[130] J. Rui, D. Wei, A. Rubio-Abadal, S. Hollerith, J. Zeiher, D. M. Stamper-Kurn, C. Gross, and I. Bloch. “A subradiant optical mirror formed by a single structured atomic layer”. en. In: *Nature* 583.7816 (July 2020), pp. 369–374. DOI: 10.1038/s41586-020-2463-x.

[131] D. Plankensteiner, L. Ostermann, H. Ritsch, and C. Genes. “Selective protected state preparation of coupled dissipative quantum emitters”. en. In: *Scientific Reports* 5.1 (Nov. 2015), p. 16231. DOI: 10.1038/srep16231.

[132] G. Facchinetti, S. D. Jenkins, and J. Ruostekoski. “Storing Light with Subradiant Correlations in Arrays of Atoms”. en. In: *Physical Review Letters* 117.24 (Dec. 2016), p. 243601. DOI: 10.1103/PhysRevLett.117.243601.

[133] G. Ferioli, A. Glicenstein, L. Henriet, I. Ferrier-Barbut, and A. Browaeys. “Storage and Release of Subradiant Excitations in a Dense Atomic Cloud”. en. In: *Physical Review X* 11.2 (May 2021), p. 021031. DOI: 10.1103/PhysRevX.11.021031.

[134] H. Zoubi and H. Ritsch. “Excitons and Cavity Polaritons for Optical Lattice Ultracold Atoms”. en. In: *Advances In Atomic, Molecular, and Optical Physics*. Vol. 62. Elsevier, 2013, pp. 171–229. DOI: 10.1016/B978-0-12-408090-4.00003-7.

[135] A. Asenjo-Garcia, M. Moreno-Cardoner, A. Albrecht, H. J. Kimble, and D. E. Chang. "Exponential Improvement in Photon Storage Fidelities Using Subradiance and "Selective Radiance" in Atomic Arrays". en. In: *Physical Review X* 7.3 (Aug. 2017), p. 031024. DOI: 10.1103/PhysRevX.7.031024.

[136] P. Solano, P. Barberis-Blostein, F. K. Fatemi, L. A. Orozco, and S. L. Rolston. "Super-radiance reveals infinite-range dipole interactions through a nanofiber". en. In: *Nature Communications* 8.1 (Nov. 2017), p. 1857. DOI: 10.1038/s41467-017-01994-3.

[137] A. Albrecht, L. Henriet, A. Asenjo-Garcia, P. B. Dieterle, O. Painter, and D. E. Chang. "Subradiant states of quantum bits coupled to a one-dimensional waveguide". In: *New Journal of Physics* 21.2 (Feb. 2019), p. 025003. DOI: 10.1088/1367-2630/ab0134.

[138] A. F. van Loo, A. Fedorov, K. Lalumière, B. C. Sanders, A. Blais, and A. Wallraff. "Photon-Mediated Interactions Between Distant Artificial Atoms". In: *Science* 342 (2013). Publisher: American Association for the Advancement of Science, pp. 1494–1496.

[139] R. Reimann, W. Alt, T. Kampschulte, T. Macha, L. Ratschbacher, N. Thau, S. Yoon, and D. Meschede. "Cavity-Modified Collective Rayleigh Scattering of Two Atoms". In: *Physical Review Letters* 114.2 (Jan. 2015). Publisher: American Physical Society, p. 023601. DOI: 10.1103/PhysRevLett.114.023601.

[140] Z. Yan, J. Ho, Y.-H. Lu, S. J. Masson, A. Asenjo-Garcia, and D. M. Stamper-Kurn. "Superradiant and Subradiant Cavity Scattering by Atom Arrays". In: *Physical Review Letters* 131.25 (Dec. 2023). Publisher: American Physical Society, p. 253603. DOI: 10.1103/PhysRevLett.131.253603.

[141] S. Nussmann, M. Hijlkema, B. Weber, F. Rohde, G. Rempe, and A. Kuhn. "Submicron Positioning of Single Atoms in a Microcavity". In: *Phys. Rev. Lett.* 95 (Oct. 2005). Publisher: American Physical Society, p. 173602.

[142] P. Domokos and H. Ritsch. “Collective Cooling and Self-Organization of Atoms in a Cavity”. In: *Phys. Rev. Lett.* 89 (Dec. 2002). Publisher: American Physical Society, p. 253003.

[143] A. T. Black, H. W. Chan, and V. Vuletić. “Observation of Collective Friction Forces due to Spatial Self-Organization of Atoms: From Rayleigh to Bragg Scattering”. In: *Phys. Rev. Lett.* 91 (Nov. 2003). Publisher: American Physical Society, p. 203001.

[144] S. Slama, G. Krenz, S. Bux, C. Zimmermann, and P. W. Courteille. “Cavity-enhanced superradiant Rayleigh scattering with ultracold and Bose-Einstein condensed atoms”. In: *Phys. Rev. A* 75 (June 2007). Publisher: American Physical Society, p. 063620.

[145] Z. Zhang, C. H. Lee, R. Kumar, K. J. Arnold, S. J. Masson, A. L. Grimsmo, A. S. Parkins, and M. D. Barrett. “Dicke-model simulation via cavity-assisted Raman transitions”. en. In: *Physical Review A* 97.4 (Apr. 2018), p. 043858. DOI: 10.1103/PhysRevA.97.043858.

[146] E. A. Bohr, S. L. Kristensen, C. Hotter, S. A. Schäffer, J. Robinson-Tait, J. W. Thomsen, T. Zelevinsky, H. Ritsch, and J. H. Müller. “Collectively enhanced Ramsey readout by cavity sub- to superradiant transition”. en. In: *Nature Communications* 15.1 (Feb. 2024). Publisher: Nature Publishing Group, p. 1084. DOI: 10.1038/s41467-024-45420-x.

[147] R. Landig, L. Hruby, N. Dogra, M. Landini, R. Mottl, T. Donner, and T. Esslinger. “Quantum phases from competing short- and long-range interactions in an optical lattice”. In: *Nature* 532 (Apr. 2016). Publisher: Nature Publishing Group, a division of Macmillan Publishers Limited. All Rights Reserved., pp. 476–479.

[148] J. Klinder, H. Keßler, M. R. Bakhtiari, M. Thorwart, and A. Hemmerich. “Observation of a Superradiant Mott Insulator in the Dicke-Hubbard Model”. In: *Phys. Rev. Lett.* 115 (2015). Publisher: American Physical Society, p. 230403.

[149] J. A. Muniz, D. Barberena, R. J. Lewis-Swan, D. J. Young, J. R. K. Cline, A. M. Rey, and J. K. Thompson. "Exploring dynamical phase transitions with cold atoms in an optical cavity". en. In: *Nature* 580.7805 (Apr. 2020), pp. 602–607. DOI: 10.1038/s41586-020-2224-x.

[150] H. Keßler, P. Kongkhambut, C. Georges, L. Mathey, J. G. Cosme, and A. Hemmerich. "Observation of a Dissipative Time Crystal". en. In: *Physical Review Letters* 127.4 (July 2021), p. 043602. DOI: 10.1103/PhysRevLett.127.043602.

[151] V. Helson, T. Zwettler, F. Mivehvar, E. Colella, K. Roux, H. Konishi, H. Ritsch, and J.-P. Brantut. "Density-wave ordering in a unitary Fermi gas with photon-mediated interactions". en. In: *Nature* 618.7966 (June 2023), pp. 716–720. DOI: 10.1038/s41586-023-06018-3.

[152] B. Casabone, K. Friebe, B. Brandstätter, K. Schüppert, R. Blatt, and T. E. Northup. "Enhanced Quantum Interface with Collective Ion-Cavity Coupling". en. In: *Physical Review Letters* 114.2 (Jan. 2015), p. 023602. DOI: 10.1103/PhysRevLett.114.023602.

[153] A. Neuzner, M. Körber, O. Morin, S. Ritter, and G. Rempe. "Interference and dynamics of light from a distance-controlled atom pair in an optical cavity". en. In: *Nature Photonics* 10.5 (May 2016), pp. 303–306. DOI: 10.1038/nphoton.2016.19.

[154] C. Hotter, L. Ostermann, and H. Ritsch. "Cavity sub- and superradiance for transversely driven atomic ensembles". In: *Physical Review Research* 5.1 (Jan. 2023). Publisher: American Physical Society, p. 013056. DOI: 10.1103/PhysRevResearch.5.013056.

[155] I. B. Mekhov and H. Ritsch. "Quantum Nondemolition Measurements and State Preparation in Quantum Gases by Light Detection". In: *Phys. Rev. Lett.* 102 (2009). Publisher: American Physical Society, p. 020403.

[156] W. Guerin, F. Michaud, and R. Kaiser. “Mechanisms for Lasing with Cold Atoms as the Gain Medium”. en. In: *Physical Review Letters* 101.9 (Aug. 2008), p. 093002. DOI: 10.1103/PhysRevLett.101.093002.

[157] R. Sawant and S. A. Rangwala. “Lasing by driven atoms-cavity system in collective strong coupling regime”. en. In: *Scientific Reports* 7.1 (Dec. 2017). Publisher: Nature Publishing Group, p. 11432. DOI: 10.1038/s41598-017-11799-5.

[158] D. Meiser and M. J. Holland. “Steady-state superradiance with alkaline-earth-metal atoms”. en. In: *Physical Review A* 81.3 (Mar. 2010), p. 033847. DOI: 10.1103/PhysRevA.81.033847.

[159] J. G. Bohnet, Z. Chen, J. M. Weiner, D. Meiser, M. J. Holland, and J. K. Thompson. “A steady-state superradiant laser with less than one intracavity photon”. en. In: *Nature* 484.7392 (Apr. 2012), pp. 78–81. DOI: 10.1038/nature10920.

[160] M. A. Norcia, M. N. Winchester, J. R. K. Cline, and J. K. Thompson. “Superradiance on the millihertz linewidth strontium clock transition”. en. In: *Science Advances* 2.10 (Oct. 2016), e1601231. DOI: 10.1126/sciadv.1601231.

[161] R. J. Thompson, G. Rempe, and H. J. Kimble. “Observation of normal-mode splitting for an atom in an optical cavity”. In: *Phys. Rev. Lett.* 68 (1992). Publisher: American Physical Society, pp. 1132–1135.

[162] A. K. Tuchman, R. Long, G. Vrijsen, J. Boudet, J. Lee, and M. A. Kasevich. “Normal-mode splitting with large collective cooperativity”. en. In: *Physical Review A* 74.5 (Nov. 2006), p. 053821. DOI: 10.1103/PhysRevA.74.053821.

[163] G. Hernandez, J. Zhang, and Y. Zhu. “Vacuum Rabi splitting and intracavity dark state in a cavity-atom system”. In: *Physical Review A* 76.5 (Nov. 2007). Publisher: American Physical Society, p. 053814. DOI: 10.1103/PhysRevA.76.053814.

[164] G. Vrijsen, O. Hosten, J. Lee, S. Bernon, and M. A. Kasevich. “Raman Lasing with a Cold Atom Gain Medium in a High-Finesse Optical Cavity”. In: *Physical Review Letters* 107.6 (Aug. 2011). Publisher: American Physical Society, p. 063904. DOI: 10.1103/PhysRevLett.107.063904.

[165] S. Zippilli, G. Morigi, and H. Ritsch. “Suppression of Bragg Scattering by Collective Interference of Spatially Ordered Atoms with a High-$Q$ Cavity Mode”. In: *Physical Review Letters* 93.12 (Sept. 2004). Publisher: American Physical Society, p. 123002. DOI: 10.1103/PhysRevLett.93.123002.

[166] T. Wilk, S. C. Webster, A. Kuhn, and G. Rempe. “Single-Atom Single-Photon Quantum Interface”. en. In: *Science* 317.5837 (July 2007), pp. 488–490. DOI: 10.1126/science.1143835.

[167] H. P. Specht, C. Nölleke, A. Reiserer, M. Uphoff, E. Figueroa, S. Ritter, and G. Rempe. “A single-atom quantum memory”. en. In: *Nature* 473.7346 (May 2011), pp. 190–193. DOI: 10.1038/nature09997.

[168] Z. Zhiqiang, C. H. Lee, R. Kumar, K. J. Arnold, S. J. Masson, A. S. Parkins, and M. D. Barrett. “Nonequilibrium phase transition in a spin-1 Dicke model”. en. In: *Optica* 4.4 (Apr. 2017), p. 424. DOI: 10.1364/OPTICA.4.000424.

[169] M. Hebenstreit, B. Kraus, L. Ostermann, and H. Ritsch. “Subradiance via Entanglement in Atoms with Several Independent Decay Channels”. en. In: *Physical Review Letters* 118.14 (Apr. 2017), p. 143602. DOI: 10.1103/PhysRevLett.118.143602.

# Acknowledgements

*Deo gratias et Mariæ!*

I would like to express my gratitude to my supervisor, **Peter Domokos**, for his generosity, patience and flexibility. He continuously monitored my work, provided invaluable professional assistance, dedicated his time to me, and ensured the proper support for my doctoral studies even amidst changes in my circumstances.

I must mention here **Péter Földi** as well, who supervised me during the first year of my doctoral studies. He respected my decision to change the topic of my research and allowed me to make this transition peacefully. He did not cease to support me up to this day, for which I remain deeply grateful.

I am also thankful to the entire Quantum Optics "Momentum" Research Group, as research – particularly experimental work – is a team effort, and the results presented here reflect their contributions as well. I cannot list all the help I received from them, but I would like to highlight some. **Dávid Nagy** introduced me to the laboratory, and continued to help me with both technical and theoretical issues. **Bálint Sárközi**'s cheerful and friendly presence made even the toughest challenges much more bearable. I did a lot of tedious work in the lab with **Adwaith Kalluvayal-Varooli**, whose optimism and persistence consistently motivated me. I could reliably turn to **Thomas Clark** with questions regarding theory and programming. I have learnt a great deal from **András Vukics**'s explanations on physics and critiques of my coding. **Andris Dombi** was ready whenever I needed help in solving technical issues in the lab. **Árpád Kurkó** assisted in the operation of the SNSPD. **Dani Varga** always knew where to look for tools and components in the lab. **Francis Williams 'Tito'**s curious ques-

tions made me think through the subject every time.

I am deeply grateful to my parents and siblings for their constant support. Last but not least, I thank my wife, **Ági**, for believing in me even when I doubted myself. I thank her, as well as my daughter, **Magdi** and my son, **Damján**, for enduring me those times and for their patience and understanding during my absences.

This work was supported by the Ministry of Culture and Innovation and the National Research, Development and Innovation Office of Hungary (NKFIH) within the Quantum Information National Laboratory of Hungary. I also acknowledge the support from the ÚNKP-23-3 New National Excellence Program and the EKÖP-24-4 University Research Scholarship Program of the Ministry for Culture and Innovation.